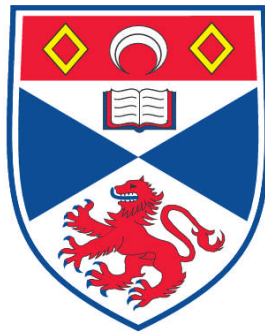


**MAGNETIC FLUX TRANSPORT SIMULATIONS:
APPLICATIONS TO SOLAR AND STELLAR MAGNETIC FIELDS**

Graeme Robert Cook

**A Thesis Submitted for the Degree of PhD
at the
University of St. Andrews**



2011

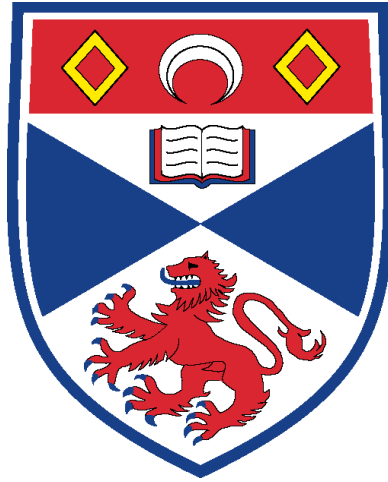
**Full metadata for this item is available in
Research@StAndrews:FullText
at:**

<http://research-repository.st-andrews.ac.uk/>

Please use this identifier to cite or link to this item:

<http://hdl.handle.net/10023/2072>

This item is protected by original copyright



UNIVERSITY OF ST ANDREWS

PHD THESIS

Magnetic Flux Transport Simulations: Applications to Solar and Stellar Magnetic Fields

Author:

Graeme Robert COOK

Supervisor:

Dr. Duncan H. MACKAY

September 18, 2011

Acknowledgements

There are many people deserve thanks for their help and support throughout the length of my PhD.

A special thanks goes to my PhD supervisor Duncan Mackay for putting up with my exploits throughout my research. His advice, help and guidance throughout my PhD research have been invaluable.

I would like to extend my warmest gratitude to both of my examiners, Claire Parnell and Mitch Berger. Their feedback and advice both during and after my viva have helped me to improve this thesis and ensure that it is worthy of final submission.

All of my friends and family who have helped my sanity and supported me throughout the good and bad times also deserve note. My parents and brothers deserve thanks for always believing in me and encouraging me to apply myself to the best of my abilities and to pursue what makes me happy. Emma Dryburgh-Cook, for putting up with me throughout my the years, through the ups and downs and always being there for me. All of my friends and colleagues who have advised me, helped me, bought the next round or been there for me also deserve credit.

I would also like to thanks STFC for their generous funding.

“It's not how hard you can hit, but how hard you can get hit and keep on going!”

“You have to risk it to get the biscuit!”

Dedicated to the memory of Mary Mackenzie and Janet Evans.

Abstract

Magnetic fields play a key role in a wide variety of phenomena found on the Sun. One such phenomena is the Coronal Mass Ejection (CME) where a large amount of material is ejected from the Sun. CME's may directly affect the earth, therefore understanding their origin is of key importance for space weather and the near-Earth environment.

In this thesis, the nature and evolution of solar magnetic fields is considered through a combination of Magnetic Flux Transport Simulations and Potential Field Source Surface Models. The Magnetic Flux Transport Simulations produce a realistic description of the evolution and distribution of the radial magnetic field at the level of the solar photosphere. This is then applied as a lower boundary condition for the Potential Field Source Surface Models which prescribe a coronal magnetic field.

Using these two techniques, the location and variation of coronal null points, a key element in the Magnetic Breakout Model of CMEs, are determined. Results show that the number of coronal null points follow a cyclic variation in phase with the solar cycle. In addition, they preferentially form at lower latitudes as a result of the complex active latitude field. Although a significant number of coronal nulls may exist at any one time (≈ 17), it is shown that only half may satisfy the necessary condition for breakout. From this it is concluded that while the Magnetic Breakout Model of CMEs is an important model in understanding the origin of the CMEs, other processes must occur in order to explain the observed number of CMEs.

Finally, the Magnetic Flux Transport Simulations are applied to stellar magnetic fields and in particular to the fast rotating star HD171488. From this speculative study it is shown that the Magnetic Flux

Transport Simulations constructed for the Sun may be applied in very different stellar circumstances and that for HD171488 a significantly higher rate of meridional flow (1200-1400 ms^{-1}) is required to match observed magnetic field distributions.

1. Candidates declarations:

I, Graeme Robert Cook, hereby certify that this thesis, which is approximately 54,000 words in length, has been written by me, that it is the record of work carried out by me and that it has not been submitted in any previous application for a higher degree.

I was admitted as a research student in September,2006 and as a candidate for the degree of PhD in Solar Physics in September 2007; the higher study for which this is a record was carried out in the University of St Andrews between 2006 and 2010.

Date

Signature of Candidate

2. Supervisors declaration:

I hereby certify that the candidate has fulfilled the conditions of the Resolution and Regulations appropriate for the degree of PhD in Solar Physics in the University of St Andrews and that the candidate is qualified to submit this thesis in application for that degree.

Date

Signature of Supervisor

3. Permission for electronic publication: (to be signed by both candidate and supervisor)

In submitting this thesis to the University of St Andrews I understand that I am giving permission for it to be made available for use in accordance with the regulations of the University Library for the time being in force, subject to any copyright vested in the work not being affected thereby. I also understand that the title and the abstract will be published, and that a copy of the work may be made and supplied to any bona fide library or research worker, that my thesis will be electronically accessible for personal or research use unless exempt by award of an embargo as requested below, and that the library has the right to migrate my thesis into new electronic forms as required to ensure continued access to the thesis. I have obtained any third-party copyright permissions that may be required in order to allow such access and migration, or have requested the appropriate embargo below.

The following is an agreed request by candidate and supervisor regarding the electronic publication of this thesis:

Access to printed copy and electronic publication of thesis through the University of St Andrews.

Date

Signature of Candidate

Signature of Supervisor

Contents

1	Introduction	25
1.1	Coronal Mass Ejections (CMEs)	27
1.1.1	Models for the Initiation of a CME	30
1.2	MHD Equations	32
1.2.1	The Induction Equation	33
1.2.2	Equation of Motion - Force Free Approximation	35
1.3	Aims	36
2	Surface Flux Transport Model for the Radial Magnetic Field	39
2.1	Surface Flux Transport Simulation: Basic Equations	40
2.1.1	Basics of Spherical Harmonics	43
2.1.2	The One Component Model	46
2.1.3	Solution With Only Diffusion	50
2.2	Test Simulation Run Results	51
2.3	Kitt Peak Synoptic Magnetogram Data	62
2.4	Conclusions	68

3	3D Coronal Field and Null Points	70
3.1	Potential Field Extrapolation Technique	71
3.2	Test Cases	74
3.2.1	Single Bipole, Overlying Global Dipole	76
3.2.2	Two Bipolar Active Regions	79
3.3	Null Point Finding Technique	82
3.4	Conclusions	87
4	Application of the Null Finding Code Over Two Solar Cycles	89
4.1	Simulation Techniques	90
4.1.1	Instant Day Simulation	91
4.1.2	Simulated Synoptic Magnetograms	97
4.2	Coronal Null Point Behaviour	102
4.2.1	Properties of Coronal Null Points	102
4.2.2	Null Numbers in Relation to Bipole Emergence Rates	108
4.2.3	Null Point Configuration Classification	109
4.3	Conclusions	113
5	Comparison of Null Point Properties with Results From Observations	115
5.1	Results from Observations	116
5.2	Comparison Between Kitt Peak Observational Results and Simulation Results	121
5.3	Conclusions	124
6	How Many Breakout Configurations May In Fact Breakout?	127
6.1	Calculating the flux above and below the null points	129

6.2	Calculating the Flux Above and Below the Null Points: Two Examples	132
6.3	Application over two solar cycles	135
6.4	Limitations of this Technique	142
6.5	Conclusions	144
7	Application of Magnetic Flux Transport Simulation to Rapidly Rotating Stellar Bodies	147
7.1	Initial Steps	149
7.2	Several Emerged Bipoles	152
7.3	Multiple Bipole Emergence Runs	156
7.3.1	Meridional Circulation Peak Value: 1200 ms^{-1}	157
7.3.2	Meridional Circulation Peak Value: 1400 ms^{-1}	159
7.4	Results	163
8	Conclusions and Future Work	165
8.1	Conclusions	165
8.2	Future Work	169

List of Figures

1.1	Image showing the structure of the Sun from the inner core, through the radiative and convection zones, past the photosphere and chromosphere, out to the solar corona. Approximate distances and widths of various layers are given, along with the direction of radiative diffusion and convection (image taken from Berthoud (1997)).	26
1.2	Image showing a 3-part CME taken from the LASCO C3 imager. Visible is the high density central core, surrounding low density cavity and leading CME front, all of which make up this CME's structure.	27
1.3	Graphs showing (a) the number of CMEs observed using the LASCO C2 and C3 imagers between 1996 and 2006 and (b) the number of observed CMEs versus latitude. The total number of CMEs in graph (b) is less than graph (a) due to the fact that halo CMEs are not included as calculating their latitude of origin is impossible. These graphs were produced using the CME catalogue from the LASCO C2 and C3 imagers.	28
1.4	Image showing the initial setup of the "Magnetic Breakout Model" postulated by Antiochos (1998). In this image red indicates positive flux, while blue indicates negative flux. This initial configuration possesses a coronal null point between the two central regions of oppositely orientated flux.	30

- 2.1 Graph showing a plot of the rate of differential rotation versus latitude. The Carrington rotation rate has been taken off in order to account for a non-moving frame of reference within our simulation. 42
- 2.2 Graph showing a plot of the meridional flow rate versus latitude. The meridional flow rate follows the behaviour of a sine curve, and can be seen to vanish above $\lambda_o = 75^\circ$ latitude. 43
- 2.3 Plots showing the Legendre polynomials. Graph (a) shows when $l=1$, (b) has $l=2$ and (c) has $l=3$. As m increases from 0 to l the various forms of the Legendre polynomials are plotted. $m = 0$ is represented by the solid line and $m = 1$ is the dotted line. Where appropriate, $m = 2$ is the dashed line and $m = 3$ is the dash-dotted line. 45
- 2.4 Images showing the spherical harmonics when $l=1$ and m is (a)0 (b)1. White represents positive values and black represents negative values. The dashed white lines on the images indicates the zeros between the positive and negative regions. 46
- 2.5 Images showing the spherical harmonics, when $l = 2$ and m is (a)0, (b)1 and (c)2. White represents positive values and black represents negative values. The dashed white lines on the images indicates the zeros between the positive and negative regions. 47
- 2.6 Images showing the spherical harmonics, when $l = 3$ and m is (a)0, (b)1, (c)2 and (d)3. White represents positive values and black represents negative values. The dashed white lines on the images indicates the zeros between the positive and negative regions. 48
- 2.7 Image showing the variation in surface flux when a single bipole is inserted and meridional flow and differential rotation are both neglected. The solid line shows what happens when $n=1$, the dotted line indicates when $n=2$ and the dashed line indicates when $n=3$. The y axis is plotted in terms of tens of days, i.e. 5=50 days. 50

2.8 Images showing the time evolution of a single emerged bipole when surface field effects are included at 0 days ((a) and (d)), 100 days ((b) and (e)) and 500 days ((c) and (f)). Images (a), (b) and (c) show these effects for a magnetic bipole with positive tilt angle, (d), (e) and (f) show the results when a negative tilt angle is used. In these images, the leading polarity is always negative, while the trailing polarity is always positive. 52

2.9 Images showing the evolution of (a) the surface magnetic flux, (b) open magnetic flux (the magnetic flux at $2.5R_{\odot}$) and (c) polar magnetic flux (i.e. flux between -90° and -70° or 70° and 90°), when a single magnetic bipole is inserted with no initial polar flux. These graphs indicate the results for when a positive tilt angle within the bipoles is used. The black line indicates a tilt angle of 0° , purple-blue indicates 5° , turquoise indicates 10° , green indicates 15° , blue indicates 20° , orange indicates 25° and red indicates 30° . In each of these simulation runs the leading polarity is negative, the trailing polarity is positive. 53

2.10 Images showing the evolution of (a) the surface magnetic flux, (b) open magnetic flux and (c) polar magnetic flux (i.e. flux between -90° and -70° or 70° and 90°), when a single magnetic bipole is inserted with no initial polar flux. These graphs indicate the results for when a negative tilt angle within the bipoles is used. The black line indicates a tilt angle of 0° , purple-blue indicates -5° , turquoise indicates -10° , green indicates -15° , blue indicates -20° , orange indicates -25° and red indicates -30° . In each of these simulation runs the leading polarity is negative, the trailing polarity is positive. 54

2.11 Images showing various time steps when a single bipole is emerged at 10° latitude ((a), (b) and (c)) and 40° latitude ((d), (e) and (f)). The bipole is then evolved forward in time. The images show the evolution of the magnetic bipole initially (Images (a) and (d)), after 100 days (Images (b) and (e)) and after 500 days (Images (c) and (f)). In all images red indicates positive magnetic field, blue indicates negative magnetic field. 56

- 2.12 Graphs showing the evolution of (a) surface flux, (b) open flux and (c) polar flux when a single magnetic bipole is inserted, with no initial polar flux and an initial peak strength of approximately 2.8×10^{22} Mx, and the latitude of emergence of the bipole is varied from 5° to 40° . Each line indicates a different latitude of emergence for the magnetic bipole. Black indicates 5° latitude of emergence, dark blue shows 10° , pale blue shows 15° , green shows 20° , orange shows 25° , red shows 30° , blue shows 35° and purple shows 40° latitude of emergence. The tilt angle of the bipole is taken to be approximately 15° , the leading polarity is negative, while the trailing polarity is positive. 58
- 2.13 Graphs showing the variation in the amount of surface flux ((a) and (d)), open flux ((b) and (e)) and total polar flux within both north and south polar regions ((c) and (f)) when the meridional flow rate is altered for a bipole emerged at 5° latitude ((a), (b) and (c)) and 30° latitude ((d), (e) and (f)). Each line represents a different peak value of meridional flow: Black shows 11m/s, dark blue shows 15m/s, light blue shows 20m/s, green shows 25m/s, yellow shows 30m/s and red indicates 35m/s. Each bipole has a positive trailing polarity and a negative leading polarity, and is emerged with an initial tilt angle of 20° 59
- 2.14 Image showing an example of one of the Kitt Peak magnetograms. Black indicates negative flux, white indicates positive flux. 63
- 2.15 Image illustrating the inaccuracy of the Kitt Peak magnetogram measurements. The solid line represents the actual radial field component, the dashed line indicates the recorded line of sight component. The difference between the two measurements at higher latitudes is obvious. 64
- 2.16 Image produced when we averaged the longitudinal magnetic field at each latitude within the Kitt Peak magnetograms for two solar cycles. The classic butterfly diagram, similar to that of bipole emergence is clearly visible. 65
- 2.17 Graphs showing the total signed value of flux against time at (a) 20° latitude, (b) -20° , (c) 40° and (d) -40° . Comparing these flux values with the averaged butterfly diagram allows comparisons as to the behaviour of the two observed solar cycles to be drawn. 66

2.18 Graphs of the total absolute value of flux against time at (a) 20°, (b) 40° and (c) 55° latitude, taken from the Kitt Peak synoptic magnetograms. The magnetogram data represents cycles 21 (June 1976 - August 1986) and 22 (September 1986 - April 1996). 67

3.1 Images showing a sample configuration from the simulation (a) before global dipole reversal and (b) after global dipole reversal. Between these images the polar field has reversed polarity, meaning that the overlying global dipole is the same orientation to the underlying bipole. In this image red indicates positive flux, blue indicates negative flux. 75

3.2 Image showing the radial field surface distribution of the first test simulation. A magnetic bipole has been inserted with a 90° tilt angle about the equator. This gives the bipole polarities the opposite orientation to the prescribed polar field in each hemisphere. 77

3.3 An orthographic image of the set up of the first test simulation. The radial surface field consists of a magnetic bipole inserted with a 90° tilt angle such that its orientation of polarities is opposite to that of the polar field within each hemisphere. The potential coronal field extrapolated from this gives a field configuration similar to that of the initial set up of the breakout model (Antiochos, 1998). The plot is made for a flux ratio of bipole to arcade flux of 0.10. Here we define arcade flux as magnetic flux between the two polar field regions, while bipole flux goes between the two polarities of the magnetic bipole. 78

3.4 Graph showing the height of the change in field orientation giving the approximate location of the null point in the first test simulation. Each line represents a different degree of half separation (namely the number of degrees between one polarity and the equator): the black line indicates 5° half separation, purple indicates 10° half separation, blue shows 15°, green indicates 20° and orange represents 25° half separation. . 79

- 3.5 Image showing the radial surface field distribution in the second test simulation. Two magnetic bipoles have been inserted along the equator with zero tilt angle. This is a setup similar to the surface configuration of the breakout model as it is also a quadrupolar field configuration. In the image red indicates positive flux and blue indicates negative flux. 80
- 3.6 Image showing an orthographic plot and field lines of the set up of the second simulation. The extrapolated coronal field shows a configuration similar to the coronal field set up within the initial configuration of the breakout model. 81
- 3.7 Plot showing the height in solar radii of the field line orientation change when (a) the inner bipole strength is held constant and the outer bipole strength is increased (solid line) and (b) the outer bipole strength is held constant and the inner bipole strength is increased (dashed line). 82
- 3.8 Plots showing (a) the calculated height of the coronal null point using the base boundary condition described in Figure 3.2 and (b) the difference between the height in field orientation previously calculated and the height of the null point. In both images the black line shows when the bipole polarities are emerged with 15° half separation, while the orange line shows 5° half separation. In image (a), the stars indicate the height of the null point calculated using the null finding technique, while the solid line indicates the height of the field line orientation change. 84
- 3.9 Plots showing (a) the calculated height of the coronal null point using the base boundary condition described in Figure 3.5 and (b) the difference between the height in field orientation previously calculated and the height of the null point. In image (a) the red diamonds represent when the inner bipole flux is held constant, the blue stars represent when the outer bipole flux is held constant. In image (b) the black line represents the difference when the inner bipole flux is held constant, while the red line indicates the difference when the outer bipolar flux is held constant. 86

4.1 Graphs showing the properties of the bipoles emerged within the simulation. (a) The distribution of bipole emergences as a function of time and latitudes, (b) the numbers of bipoles emerging per 27 days, (c) the total flux within the emerging bipoles per year, (d) the average monthly tilt angle of the bipoles, (e) tilt angle distribution throughout the simulation and (f) the average tilt angle vs. latitude. The first cycle depicted in the plots above was used as a “control” cycle to initiate the simulation. The work presented here will only analyse cycles two and three where flux values have been scaled to KP synoptic data. 92

4.2 Sample radial surface maps taken from various stages of one of the solar cycles within the instant day simulation. Each map shows a different stage of the cycle. These are (a) solar minimum, (b) rising phase, (c) solar maximum, (d) declining phase and (e) solar minimum. Within the diagrams, red indicates positive magnetic flux and blue indicates negative magnetic flux, where the field strength saturates at 10G. 93

4.3 Graphs showing the surface flux from our “instant day” simulation. Graph (a) shows the total surface flux while (b) shows the flux at 40° latitude. In each case the solid lines denote the flux values deduced from the Kitt Peak synoptic magnetograms where the dashed curve denotes the results of the simulations. The double ended arrows in each graph denote a 2-year time period around cycle maximum determined from the peaks in bipole emergence rate. 94

4.4 Image showing (a) a typical instant day map and (b) a simulated synoptic magnetogram. The 27 day period covered by the simulated synoptic magnetogram is the same 27 day rotation period the instant day example is taken from. The area within the vertical black lines corresponds to the portion of the instant day map that lies at central meridian and is extracted and inserted into the simulated synoptic magnetogram. Several key features have been marked on both the instant day map and the simulated synoptic magnetogram. 98

- 4.5 Graphs showing the surface flux from our simulated synoptic magnetogram conversion data. Graph (a) shows the total surface flux while (b) shows the flux at 40° latitude. In each case the solid lines denote the flux values deduced from the Kitt Peak synoptic magnetograms where the dashed curve denotes the results of the simulations. The double ended arrows in each graph denote a 2-year time period around cycle maximum determined from the peaks in bipole emergence rate. 100
- 4.6 Graph (a) shows the difference between the amount of magnetic flux within the Kitt Peak magnetograms and the instant day simulation (dashed line) and the difference between the amount of magnetic flux in the Kitt Peak magnetograms and the simulated synoptic magnetograms (solid line). Graph (b) is a plot of the difference between these two properties, where the range of y has been limited to positive values only. This second graph highlights the points throughout the solar cycle where the flux values within the simulated synoptic maps give a better match to the flux values within the Kitt Peak magnetograms than those within the instant day simulation. 101
- 4.7 Graphs showing the variation in total number of nulls found in (a) the instant day simulation and (c) the simulated synoptic simulation. The number of those nulls connected with the overlying global dipole can also be seen for (b) the instant day map simulation and (d) the simulated synoptic simulation. The double ended arrows in each graph denote a 2-year time period around cycle maximum determined from the peaks in bipole emergence rate 103
- 4.8 Images showing a field line plot around a null that is connected with the overlying global dipole (top) and not connected with the global dipole (bottom). 104
- 4.9 Graphs showing the variation of certain properties of coronal null points, located in the instant day simulation. Graph (a) shows the distribution of null points with latitude, (b) shows the average absolute value of latitude as a function of time, (c) shows the average radial height of coronal null points as a function of latitude, (d) shows the number of coronal null points as a function of radial height in the corona and (e) shows the average radial height as a function of time. 105

- 4.10 Butterfly diagrams showing the distribution of null points in (a) the instant day map simulation and (b) the simulated synoptic magnetogram simulation (right). 107
- 4.11 A scatter plot of the number of null points found every 27 days vs. the number of bipolar regions emerged every 27 days. The triangle in the centre indicates the mean point of both data sets. The solid line denotes a gradient of $1/3$ while the dashed line $1/2$ 108
- 4.12 Graphs showing (a) the number of nulls found in the instant day map simulation with 100% of the bipoles emerged, (b) the number of nulls found in the instant day map simulation with 75% of the bipoles emerged, (c) the number of nulls found in the instant day map simulation with 50% of the bipoles emerged and (d) the number of nulls found in the instant day map simulation with 25% of the bipoles emerged. The double ended arrows in each graph denote a 2-year time period around cycle maximum determined from the peaks in bipole emergence rate. 110
- 4.13 Images showing examples of the photospheric flux distributions used in order to classify the null point configuration. The first example (a) is a triple polarity configuration, (b) a newly emerged quadrapolar flux distribution, (c) an enclosed quadrapolar flux distribution and (d) an advected quadrapolar flux distribution. 111
- 4.14 Graphs showing the classification of the null points within the instant day simulation. The graphs show results for (a) a triple polarity configuration, (b) newly emerged quadrapolar configuration, (c) an enclosed quadrapolar configuration and (d) advected quadrapolar configuration. The double ended arrows in each graph denote a 2-year time period around cycle maximum determined from the peaks in bipole emergence rate. 112

5.1 Images showing two Kitt Peak magnetograms used as a base boundary condition for potential field extrapolation. Each image is taken from a different stage within the solar cycle. Image (a) is taken from solar minimum (Carrington rotation 1645, dated August 1976) while image (b) shows the photospheric distribution around solar maximum (Carrington rotation 1710, dated June 1981). Each image has the polarity inversion lines drawn on (black lines). 117

5.2 Graphs showing the results from a scan for coronal null points determined using the Kitt Peak synoptic maps as a base boundary condition for a potential field extrapolation. Graph (a) shows the number of nulls per map plotted against time, (b) shows a plot of the number of nulls against latitude, (c) shows the average height of the null points plotted against latitude, (d) shows the average radial height of the null points with time, (e) shows the number of null points with radial height plotted on a logarithmic axis in y, with a straight line indicating the gradient of the line of best fit plotted over and (f) shows a butterfly plot of the null point latitudes with time. 118

6.1 Illustration showing extrapolating the radial plane from the solar surface out to 2.5 solar radii. The direction of the magnetic field through the extrapolated plane is then calculated. The plane red indicates a negative direction of magnetic field, blue indicates positive magnetic field, relative to the unit normal $\hat{n} = \frac{-\nabla B_r}{|-\nabla B_r|}$. The white line is the separatrix along which there is a rapid reversal of the field components with height and the green dot shows the position of the null point relative to the plane and separatrix position. 131

6.2 Images showing (a) a plot of the field lines directly around the null point and (b) the sign of the projection of the magnetic field through the radial plane taken around a null point occurring at solar minimum. Blue indicates positive field, red indicates negative field, relative to the unit normal vector \hat{n} . The green square in image (b) indicates the position of the null point relative to the extrapolated radial plane. 133

6.3 Graphs showing (a) strength of \mathbf{B} in the direction of \hat{n} and (b) angle between \mathbf{B} and \hat{n} for a null point located at solar minimum. On graph (a) the dashed line indicates the sign change (and approximate null point location) within the radial plane, and graph (b) the dashed line indicates a 90° angle between \hat{n} and \mathbf{B} , which is the point where the null point is located. 134

6.4 Images showing (a) a plot of the field lines directly around the null point and (b) the sign of the projection of the magnetic field through the radial plane taken around a null point occurring at solar maximum. Blue indicates positive field, red indicates negative field, relative to the unit normal vector \hat{n} . The green square in image (b) indicates the position of the null point relative to the extrapolated radial plane. 135

6.5 Graphs showing (a) strength of the magnetic field in the direction of \hat{n} and (b) angle between \mathbf{B} and \hat{n} for a null point located at solar minimum. On graph (a) the dashed line indicates the sign change (and approximate null point location) within the radial plane, and graph (b) the dashed line indicates a 90° angle between \hat{n} and \mathbf{B} , which is the point where the null point is located. 136

6.6 Graphs showing results from the flux calculation when only 1 grid point is used, around the coronal null. The graphs show (a) the fraction of null points that have more flux below them than above versus time and (b) the number of null points that have more flux below them than above versus time. Graph (c) shows a scatter plot of flux below against flux above the null points, where the lines indicate $10\times$ flux above (dotted), $2\times$ flux above (dashed), flux below equals flux above (solid line), $2\times$ flux below (dash triple dot) and $10\times$ flux below (dot dash). Graph (d) shows a cumulative distribution of the null points, where the solid line indicates the fraction of the total null points that have a ratio of flux below over flux above which is less than the given value on the x axis. The dashed line indicates where flux below equals flux above. . . 137

- 6.7 Graphs showing results from the flux calculation when only 1 grid point is used, around the coronal null. Graph (a) shows the number of null points that have more flux below them than above against height, (b) shows the fraction of null points that have more flux below them than above at the given radial height and graph (c) shows the number of null points that have more flux below them than above with latitude (solid line). In image (c) the dotted line represents the total number of nulls with latitude plotted over the top. 138
- 6.8 Graphs showing results from the flux calculation when the maximum 11 grid point are used along the polarity inversion line. The graphs show (a) the fraction of null points that have more flux below them than above versus time and (b) the number of null points that have more flux below them than above versus time. Graph (c) shows a scatter plot of flux below against flux above the null points, where the lines indicate 10× flux above (dotted), 2× flux above (dashed), flux below equals flux above (solid line), 2× flux below (dash triple dot) and 10× flux below (dot dash). Graph (d) shows a cumulative distribution of the null points, where the solid line indicates the fraction of the total null points that have a ratio of flux below over flux above which is less than the given value on the x axis. The dashed line indicates where flux below equals flux above. 139
- 6.9 Graphs showing results from the flux calculation when the maximum 11 grid points are used along the polarity inversion line. Graph (a) shows the number of null points that have more flux below them than above against height, (b) shows the fraction of null points that have more flux below them than above at the given radial height and graph (c) shows the number of null points that have more flux below them than above with latitude (solid line). In image (c) the dotted line represents the total number of nulls with latitude plotted over the top. 140

- 6.10 Images showing some basic setups and coronal field configurations from examples that could occur within the flux calculation technique: (a) shows our very idealised setup, wherein the idea for our flux calculation technique was derived, (b) shows a setup similar to this, but the lower latitude bipole is stronger than the higher latitude bipole, which results in a non symmetric coronal field extrapolation and (c) shows a coronal field extrapolation when a triple polarity configuration causes a null point to arise. 143
- 7.1 Plot of solar differential rotation (dashed line) and the enhanced stellar differential rotation of HD171488 (solid line). A calculated carrington rotation rate for each line has been applied and subtracted in order that the radial surface field does not move within the given frame of reference. 148
- 7.2 Plots showing the average bipole tilt angle versus latitude when the observed map from HD171488 is evolved forward for (a) 0 days, (b) 10 days and (c) 20 days using solar meridional circulation rates. In each graph the error bars represent the distribution of tilt angles at each latitude. The images on the right show the radial surface distribution at (d) day 0, (e) day 10 and (f) day 20, all plotted for a saturation level of 10 Gauss. The Polarity inversion lines are given by the black lines. 150
- 7.3 Radial surface field images taken when 5 bipoles with an initial tilt angle of 0° are emerged at 10° latitude, and then evolved forward for 20 days. Image (a) shows the radial surface field distribution at day 0, while images (b), (c), (d) and (e) show the radial field distribution at day 20 for a different peak value of meridional circulation. Image (b) shows when a peak value of 50 m s^{-1} is used, (c) shows when a peak value of 100 m s^{-1} is used, (d) shows when a peak value of 200 m s^{-1} is used and (e) shows when a peak value of 300 m s^{-1} is used. All images are produced for a saturation level of 10 Gauss. Similar images can be produced when the bipoles are initially emerged at different latitudes and when the initial tilt angle of the bipoles is set to 30° 152

- 7.4 Plots showing the average tilt angle after 20 days of five bipoles with the same latitude of emergence, when the initial tilt angle is (a) 0° or (b) 30° . The resulting tilt angle after 20 days is plotted against the initial latitude of emergence of the bipoles. In both graphs the dot-dashed line indicates the average tilt angle versus latitude of the observed map from HD171488, the dashed line indicates the average tilt angle after the observed map has been evolved for 20 days with enhanced differential rotation and solar meridional circulation. Each solid coloured line indicates a different peak value of meridional circulation used to evolve the 5 bipoles. Black indicates a peak value of 11 m s^{-1} , blue shows 50 m s^{-1} , turquoise represents a peak value of 100 m s^{-1} , green represents 200 m s^{-1} and yellow has a peak value of 300 m s^{-1} . The bars on the two lines indicating data from the observed runs show the standard deviation within the observed data set. 153
- 7.5 Plots showing the average tilt angle after 20 days of five bipoles with the same latitude of emergence, when the initial tilt angle is (a) 0° or (b) 30° . The average tilt angle after 20 days is plotted against the initial latitude of emergence of the bipoles. In both graphs the solid black line, with bars showing variation, indicates the average tilt angle versus latitude of the observed map from HD171488, while each solid coloured line indicates a different peak value of meridional circulation. Dark blue indicates a peak value of 1100 m s^{-1} , turquoise represents a peak value of 1200 m s^{-1} , green represents 1300 m s^{-1} and red has a peak value of 1400 m s^{-1} 155
- 7.6 Plots showing the average tilt angle versus latitude at various time-steps within the simulation where bipoles are emerged in both hemispheres, where meridional circulation has a peak value of 1200 m s^{-1} . Plot (a) is taken from day 8, (b) is taken from day 31 and (c) is taken from day 60. Images (d), (e) and (f) show the corresponding radial surface field distributions plotted for a saturation level of 50 Gauss. The black lines are polarity inversion lines plotted on the surface. 158

- 7.7 Plots of the wider profile of meridional circulation implemented (black line) with the original profile plotted for comparison (red line). Plot (a) shows when the peak value is taken to be 1200 m s^{-1} , while plot (b) shows when the peak value is taken to be 1400 m s^{-1} 159
- 7.8 Plots showing the average tilt angle versus latitude at various time-steps within the simulation. Bipoles are emerged in both hemispheres and the wider profile of meridional circulation with a peak value of 1200 m s^{-1} is applied. Plot (a) is taken from day 8, (b) is taken from day 31 and (c) is taken from day 60. Images (d), (e) and (f) show the corresponding radial surface field distributions plotted for a saturation level of 50 Gauss. The black lines are polarity inversion lines plotted on the surface. . . . 160
- 7.9 Plots showing the average tilt angle versus latitude at various time-steps within the simulation where bipoles are emerged in both hemispheres using the original profile of meridional circulation with a peak value of 1400 m s^{-1} . Plot (a) is taken from day 8, (b) is taken from day 31 and (c) is taken from day 60. Images (d), (e) and (f) show the corresponding radial surface field distributions plotted for a saturation level of 50 Gauss. The black lines are polarity inversion lines plotted on the surface. 161
- 7.10 Plots showing the average tilt angle versus latitude at various time-steps within the simulation where 400 bipoles are emerged in both hemispheres using the wider profile of meridional circulation with a peak value of 1400 m s^{-1} . Plot (a) is taken from day 8, (b) is taken from day 31 and (c) is taken from day 60. Images (d), (e) and (f) show the corresponding radial surface field distributions plotted for a saturation level of 50 Gauss. The black lines are polarity inversion lines plotted on the surface. 162

1

Introduction

The Sun is the closest star to Earth, at a distance of 1 AU ($1.50 \times 10^{11} \text{ m} = 215 R_{\odot}$). It is approximately 4.5×10^9 years old, has a mass of $1.99 \times 10^{30} \text{ kg}$ and a radius $R_{\odot} = 696,000 \text{ km}$. The Sun itself is a ball of plasma that is held together by its own gravity, with a mean density of $1.4 \times 10^3 \text{ kg m}^{-3}$. The Sun does not rotate as a solid body and exhibits differential rotation. The properties of this differential rotation are an equatorial rotation rate of approximately 26 days and a polar rotation rate of approximately 30 days. There are two additional large-scale surface flow effects which transport magnetic flux on the solar surface. These are meridional circulation and super-granular diffusion (full details of these transport processes can be found in Chapter 2).

The image in Figure 1.1 shows the structure of the Sun from the radiative inner core to the corona. The inner core is the hottest region of the Sun, with temperatures of $15 \times 10^6 \text{ K}$. Energy is first transported out of the core as photons traveling through the radiative zone and then through convection in the convection zone. Through these regions the temperature drops to 400,000K in the radiative zone and then approximately 14,000K in the convection zone. Just above the convection zone lies the photosphere. This is the visible layer that we see when observing the Sun, and has a temperature of approximately 6,000K. Above the photosphere is a thin layer called the chromosphere. The temperature in this layer is approximately 10,000K. Above this lies the corona, which has a temperature of approximately $2 \times 10^6 \text{ K}$. The corona is only visible to the naked eye during times of full solar eclipse, due to the brightness of the solar photosphere.

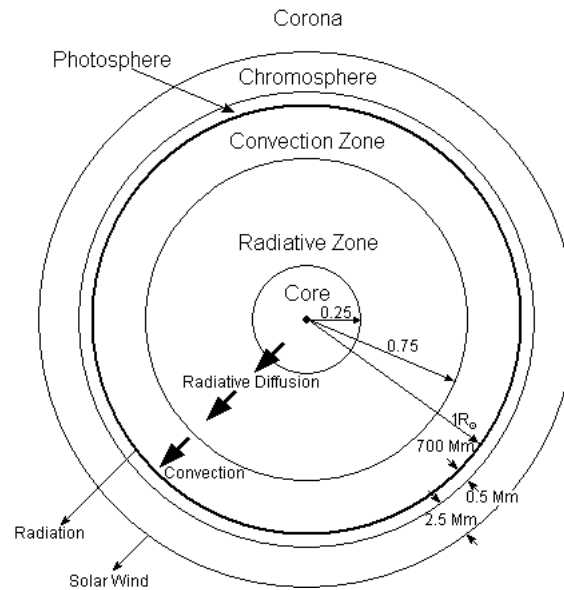


Figure 1.1: Image showing the structure of the Sun from the inner core, through the radiative and convection zones, past the photosphere and chromosphere, out to the solar corona. Approximate distances and widths of various layers are given, along with the direction of radiative diffusion and convection (image taken from Berthoud (1997)).

The magnetic field on the Sun follows the solar sunspot cycle, which is approximately 11 years in length. During this time, the magnetic field in the polar regions switches signs just after solar maximum and magnetic bipoles follow a general emergence pattern. At the start of the solar cycle, magnetic bipoles emerge at higher latitudes on the photosphere (approximately $\pm 40^\circ$). As the solar cycle progresses towards solar maximum, where emergence rates are at their highest, the average latitude of emergence of magnetic bipoles gets closer to the solar equator. During the declining phase of the cycle, named due to the declining numbers of emerging magnetic bipoles, the average latitude of emergence remains low and around the equator, whilst the number of emerging bipoles decreases. This results in a drop in the amount of large scale magnetic flux on the Sun. As the new cycle begins, magnetic bipoles start emerging at higher latitudes and then follow the same pattern described above in the new cycle. Whilst the Sun generally follows this emergence pattern, during Maunder Minimum (which occurred between 1645 and 1715), sunspot observations were very rare. No distinct pattern was seen and only about 50 sunspots were seen during this time.

Whilst the emerging sunspots follow the described emergence patterns, they also follow several distinct patterns during the 11 year cycles, namely Joy's tilt law and Hale's polarity law. Joy's law

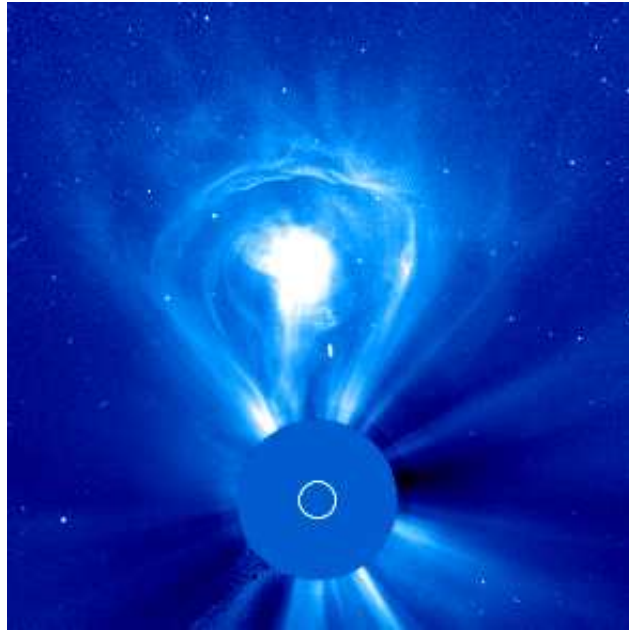


Figure 1.2: Image showing a 3-part CME taken from the LASCO C3 imager. Visible is the high density central core, surrounding low density cavity and leading CME front, all of which make up this CME's structure.

described how the emerging bipoles appear with a tilt angle which tends to have the leading polarity tilted towards the equator and the trailing polarity tilted towards the polar field. Hale's law describes how magnetic bipoles emerge such that the east-west ordering of polarities within the bipole is opposite within hemispheres and that the leading spot has the same polarity as the polar field of the hemisphere into which it is emerging. It then describes how the orientation of the polarities switches between solar cycles, but still follows this general rule.

The Sun exhibits a wide variety of phenomena ranging from filaments/prominences (Martin , 1998) and coronal loops (Zaitsev and Stepanov, 2008) to solar flares (Phillips , 2002) and coronal mass ejections (CMEs) to name but a few. Some of these, most notably CMEs, can cause a variety of space weather and have various affects upon the Earth's magnetic field and surrounding atmosphere.

1.1 Coronal Mass Ejections (CMEs)

A coronal mass ejection is a huge eruption of plasma, which can be up to approximately 10^{16} kg, originating from the solar atmosphere. The frequency of eruptions can vary between one every few

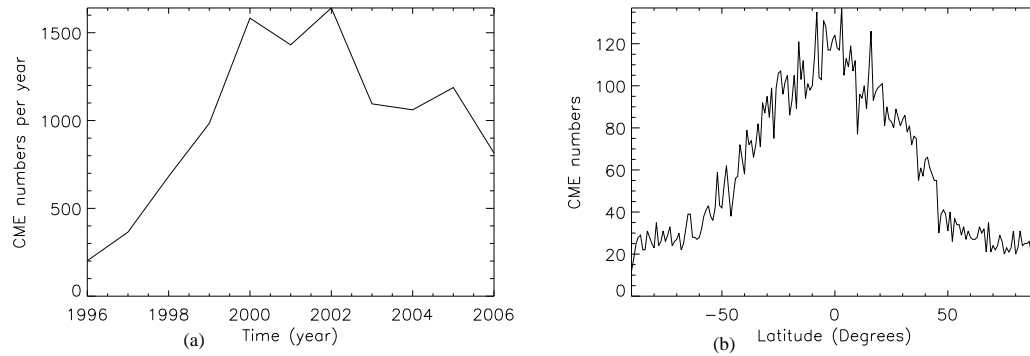


Figure 1.3: Graphs showing (a) the number of CMEs observed using the LASCO C2 and C3 imagers between 1996 and 2006 and (b) the number of observed CMEs versus latitude. The total number of CMEs in graph (b) is less than graph (a) due to the fact that halo CMEs are not included as calculating their latitude of origin is impossible. These graphs were produced using the CME catalogue from the LASCO C2 and C3 imagers.

days at solar minimum, to 5 or 6 per day at solar maximum. They propagate away from the Sun at speeds of up to 1000 km s^{-1} . The first detected CME was documented by Tousey (1973), at the National Research Laboratory using the orbiting solar observatory (OSO-7). He documented the CME using observational data obtained from Skylab. Figure 1.2 shows a LASCO C3 image of a three part CME, named such due to the 3 part structure present within it, which consists of a high density central core, low density surrounding cavity and propagation front leading the CME. Over the years, much work has been done to calculate the variation of coronal mass ejections throughout the solar cycle, from variability of size to latitude of occurrence to frequency and other characteristics (Cremades & St. Cyr, 2007). Using all of the coronagraph data collected so far (almost three solar cycles worth) Cremades & St. Cyr (2007) found that CMEs follow a cyclic variation throughout the solar cycle, with more occurring just after solar maximum, at the start of the declining phase, and fewer at solar minimum. Moreover, detailed analysis of the properties of CMEs and their source-region variation over the solar cycle, indicate that in fact, the spatio-temporal distribution of CME sources follow the sunspot butterfly diagram, with more occurring at higher latitudes during the rising phase of the cycle, and getting closer to the solar equator until just after solar maximum, where they remain throughout the declining phase until solar minimum' (Yashiro et al., 2004; Cremades et al., 2006; Howard et al., 2008). Figure 1.3(a) shows the numbers of CMEs observed by the LASCO instrument throughout solar cycle 23 (from 1996-2006). This data was obtained from Taylor the LASCO website (<http://cdaw.gsfc.nasa.gov/CMElist/>). These numbers include all sizes of CME observed by the C2

and C3 coronagraphs, including halo CMEs. The sizes of the CMEs range from tiny (less than 10^9 kg) to huge (approximately 10^{16} kg). The observed variation illustrates that as the amount of emerging magnetic flux on the solar surface increases through the cycle, the number of coronal mass ejections increase. The numbers peak around solar maximum and then decrease during the declining phase. Figure 1.3(b) shows the number of CMEs occurring with latitude using the LASCO data for all sizes of CME. This is calculated using the recorded position angle of the CME. It is worth noting that the total numbers here are less than the overall number of CMEs due to the latitude of occurrence of halo CMEs being indeterminable. Most of the CMEs occur within the active latitudes of the Sun, $\pm 50^\circ$ latitude, with fewer CMEs occurring at higher latitudes. These two graphs suggest that there is a connection between the emerging magnetic flux on the solar surface and the occurrence of a coronal mass ejection.

CMEs are generally associated with other solar events, including solar flares (Chertok, 1997) and eruptive prominences (Zhou et al., 2003). This association is not fully understood and it was once thought that flares and CMEs were directly connected, with flares driving CMEs. However, it is now thought that only approximately 60% of flares are actually associated with a CME (Andrews, 2003). Presently, CMEs (which have an associated flare) and the associated flares themselves are thought to be caused by a common event. This is due to the peak of the CME speed and the flare peak radiation often coinciding at the same time. While the common association is yet to be understood, it is thought that these events are triggered by a large scale restructuring of the magnetic field.

A CME can have various effects on the Earth and the surrounding environment. If an interplanetary coronal mass ejection is directed Earthwards and comes into contact with the magnetosphere it compresses the dayside (the side closest to the Sun) and extends the nightside (the side furthest away from the Sun). This creates trillions of watts of energy that are sent back into the upper atmosphere of the Earth. This may result in *aurora borealis* (in the northern hemisphere) and *aurora australis* (in the southern hemisphere). CMEs can also have negative effects on Earth. They can disrupt radio transmissions, cause power outages, cause damage to satellites and short electrical transmission lines and they are also dangerous to astronauts due to the high levels of charged particles present within them.

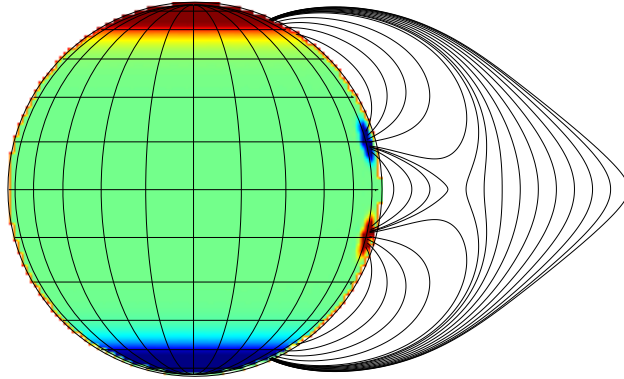


Figure 1.4: Image showing the initial setup of the “Magnetic Breakout Model” postulated by Antiochos (1998). In this image red indicates positive flux, while blue indicates negative flux. This initial configuration possesses a coronal null point between the two central regions of oppositely orientated flux.

1.1.1 Models for the Initiation of a CME

A variety of possible CME initiation mechanisms have been proposed utilizing a variety of physical phenomena. These include processes such as flux injection (Chen, 1989, 1996), dynamical instabilities (Tokman & Bellan, 2002; Török & Kliem, 2003; Kusano et al., 2004) and flux cancellation (van Ballegooijen & Martens, 1989; Priest & Forbes, 1990; Forbes & Priest, 1995).

In the flux injection model (Chen, 1989, 1996), a flux rope is held in the corona, initially in equilibrium. Magnetic flux is then injected into the base of the rope, which causes a loss of equilibrium. This forces the base of the flux rope to rise through the corona and may eventually cause a CME eruption. The initiation of a CME has been looked at in terms of dynamical instabilities. Tokman & Bellan (2002); Török & Kliem (2003); Kusano et al. (2004) look at the effects of photospheric motions on an initially twisted coronal flux tube. As the foot points of the flux tube are moved due to these photospheric motions, coronal field configurations are produced which are shown to include

the 3 part eruptive structure.

In flux cancellation (van Ballegoijen & Martens, 1989; Priest & Forbes, 1990; Forbes & Priest, 1995), a purely dipolar photospheric field is initially used. As the photospheric field is sheared, reconnection between the different regions of magnetic flux occurs. This reconnection restructures the coronal field and eventually results in a helical flux rope forming, which can support prominence plasma. As reconnection continues, eruption occurs. Recently Yeates & Mackay (2009) carried out global simulations of the coronal field based on observed magnetograms and found that flux cancellation leading to the formation and loss of equilibrium of flux ropes could account for 50% of the observed CME ejection rates over a 6 months period in 1999. Full reviews of CME initiation mechanisms are available in the papers of Klimchuk (2001) and Lin et al. (2003).

The CME model of interest within the work presented here is the “Magnetic Breakout Model”, originally described by Antiochos (1998) (see also Antiochos et al. (1999); MacNeice et al. (2004); Lynch et al. (2004); Choe et al. (2005)). In this model, a coronal null point plays a central role in the ejection of magnetic flux from within the solar corona. The model consists of a quadrupolar photospheric flux distribution, with overlying coronal field. This photospheric distribution gives rise to four distinct magnetic flux regions (see Figure 1.4). The two centrally located coronal flux regions are of opposite orientation and give rise to the formation of a coronal null point between them. Initially, this setup is held in equilibrium. A shear flow is then driven across the central region of the photospheric field. This shear flow causes the central flux region to rise, reconnecting with the overlying magnetic flux at the null point. This newly reconnected magnetic flux then transfers into the two side regions of the coronal distribution, while the central region continues to rise. As the overlying field is removed, the flux in the two side regions increases the pressure inwards on the central region of flux, causing the central region of magnetic flux to rise rapidly. This results in an ejection of plasma out into interplanetary space. If the overlying coronal field is not removed through reconnection, the underlying magnetic flux is unable to breakout through the corona in the form of a coronal mass ejection and is restricted.

The null point within the Magnetic Breakout model is a key factor, as it is where the reconnection and removal of the overlying flux occurs. It is known that in 3D, reconnection may also occur at sites other than just null points, such as current sheets (Priest & Démoulin, 1995; Démoulin et al.,

1996; Hornig & Priest, 2003; Titov et al., 2003; Galsgaard et al., 2003; Pontin et al., 2005; Haynes et al., 2007). However, for simplicity, the study presented here will focus on the variation of coronal null points as these are easily identified and are a key feature within the original model presented by Antiochos (1998). Therefore, we will use the variation of coronal null points to indicate the variation of possible breakout configurations.

1.2 MHD Equations

When modeling the magnetic field and plasma of the Sun, it is reasonable to assume that the Magneto-hydrodynamic (MHD) approximation can be used. Here, simplified Maxwell's equations, Newton's Law of Motion, an energy equation, Ohm's law, an equation of state and the equation of mass continuity describe the behaviour of the magnetic field and plasma. Using these equations, and eliminating the electric field between Maxwell's equation and Ohm's law, gives rise to the Magnetic Induction Equation, which relates the plasma velocity (\mathbf{v}) to the magnetic field (\mathbf{B}).

The MHD equations are:

$$\rho \frac{\partial \mathbf{v}}{\partial t} + \rho (\mathbf{v} \cdot \nabla) \mathbf{v} = -\nabla p + \mathbf{j} \times \mathbf{B} + \rho \mathbf{g} + F_v, \quad (1.1)$$

$$\nabla \times \mathbf{B} = \mu \mathbf{j}, \quad (1.2)$$

$$\nabla \times \mathbf{E} = -\frac{\partial \mathbf{B}}{\partial t}, \quad (1.3)$$

$$\nabla \cdot \mathbf{B} = 0, \quad (1.4)$$

$$\nabla \cdot \mathbf{E} = 0, \quad (1.5)$$

$$\mathbf{j} = \sigma (\mathbf{E} + \mathbf{v} \times \mathbf{B}) . \quad (1.6)$$

$$p = \frac{k_b \rho}{m_p} T, \quad (1.7)$$

$$\frac{\partial \rho}{\partial t} + \nabla \cdot (\rho \mathbf{v}) = 0, \quad (1.8)$$

$$\frac{\rho^\gamma}{\gamma - 1} \frac{d}{dt} \left(\frac{p}{\rho^\gamma} \right) = -L, \quad (1.9)$$

Equation 1.1 represents Newton's second law of motion, while Equations 1.2 (Ampere's Law), 1.3 (Faraday's Law), 1.4 (the Solenoidal constraint) and Equation 1.5 (Gauss Law) are 4 of Maxwell's equations. Equation 1.6 is Ohm's law and Equations 1.7, 1.8 and 1.9 represent the Ideal Gas Law, equation of mass continuity and energy equation respectively. In these equations, \mathbf{B} represents the magnetic field, \mathbf{j} is the current density, \mathbf{E} is the electric field, \mathbf{v} represents the plasma velocity, F_v denotes forces due to viscosity, L is the total energy loss function, t , p and ρ represent time, pressure and density respectively and \mathbf{g} is gravity. Parameters used in these equations include the magnetic permeability ($\mu_0 = 4\pi \times 10^{-7} \text{Hm}^{-1}$), the mass of a proton (m_p), the Boltzmann constant (k_b), the surface temperature of the Sun T and the ratio of specific heats γ (usually $\gamma = \frac{5}{3}$). If $L = 0$, then Equation 1.9 is adiabatic, which means that there is no heat transfer within the plasma.

The equations of MHD are written in this form in order to allow for the key assumptions of MHD. The first is that typical plasma velocities are much less than that of the speed of light, and the second is charge neutrality, which occurs when all of the charge within a volume adds up to zero, and is neither positive or negative.

1.2.1 The Induction Equation

Using Ohm's law (Equation 1.6), coupled with Equations 1.3 and 1.2, the quantities \mathbf{E} and \mathbf{j} can be eliminated to give:

$$\frac{\partial \mathbf{B}}{\partial t} = \nabla \times (\mathbf{v} \times \mathbf{B}) + \eta \nabla^2 \mathbf{B}, \quad (1.10)$$

where $\eta = \frac{1}{\sigma\mu}$ represents the magnetic diffusivity and is taken as a constant. This equation is called the Magnetic Induction equation. In this equation, $\nabla \times (\mathbf{v} \times \mathbf{B})$ represents the advective term, which describes how the magnetic field lines move with the plasma, and $\eta \nabla^2 \mathbf{B}$ represents the diffusive term, which describes how the magnetic field lines diffuse through the plasma. This equation allows us to calculate the magnetic field \mathbf{B} , subject to the condition that $\nabla \cdot \mathbf{B} = 0$. If the ratio of the two terms on the right hand side is taken, a new parameter can be defined. This is,

$$R_m = \frac{l_0 v_0}{\eta}. \quad (1.11)$$

This tells us the relative importance of advection to diffusion and the size of the Magnetic Reynolds number (R_m) indicates which of the two effects is the more dominant. If R_m is large (i.e. $R_m \gg 1$), this indicates that the advection term dominates within the induction equation, which can be simplified to:

$$\frac{\partial \mathbf{B}}{\partial t} = \nabla \times (\mathbf{v} \times \mathbf{B}). \quad (1.12)$$

This is called the *perfectly conducting limit* and the magnetic field follows the frozen in flux theorem, wherein the magnetic field lines move with the plasma.

If $R_m \ll 1$, this indicates that the diffusive term ($\eta \nabla^2 \mathbf{B}$) is dominant, meaning we can use the diffusive approximation. In this approximation we can approximate the induction equation by:

$$\frac{\partial \mathbf{B}}{\partial t} = \eta \nabla^2 \mathbf{B}. \quad (1.13)$$

This is called the *diffusive limit*, and the magnetic field lines do NOT move with the plasma, but rather, can diffuse through it.

In the majority of the universe, $R_m \gg 1$, whilst $R_m \ll 1$ whenever length scales are short e.g. in current sheets and during reconnection. The effects of both terms within the induction equation will be modelled in the work presented here in order to accurately model the magnetic field evolution.

1.2.2 Equation of Motion - Force Free Approximation

Using Newton's second law of motion, which states that $mass \times acceleration = force$, the force-free approximation can be derived. In Newton's second law (Equation 1.1), the terms on the right hand side represent pressure force ($-\nabla p$), gravitational force ($\rho \mathbf{g}$) and the Lorentz force ($\mathbf{j} \times \mathbf{B}$, which represents the force on a point charge due to electromagnetic fields). Using typical length scales for each term, and several key assumptions, we can reduce the equation of motion to the force free approximation, a special case of which is the potential field. Initially, compare the velocity term (left hand side of the equation) with the Lorentz force. Using typical length scales for each of the quantities, this yields,

$$\frac{\rho v_0}{t_0} \ll \frac{B_0^2}{\mu l_0}. \quad (1.14)$$

This can be rearranged to give $v_0 \ll v_A$, where $v_A = \frac{B_0}{\sqrt{\rho \mu}}$ is the Alfvén Speed. This is our first assumption, and eliminates the left hand side of the equation of motion. Next, the magnitude of the gravity and pressure forces are compared in order to determine the dominant term. Here, we can neglect gravity in favour of pressure if,

$$\frac{p_0}{l_0} \gg \rho_0 g = \frac{p_0}{H}, \quad (1.15)$$

where ρ_0 and p_0 represent typical density and pressure values and $H = \frac{k_b T}{m_p g}$ is the pressure scale height. This means gravity can be neglected in favour of pressure if,

$$l_0 \ll H. \quad (1.16)$$

Comparing the remaining terms we see that pressure can be neglected in favour of the Lorentz force, which is the force on a point charge due to electromagnetic fields, if,

$$\frac{p_0}{l_0} \ll \frac{B_0^2}{\mu l_0}. \quad (1.17)$$

Another way of expressing this is to say,

$$\beta \ll 1, \quad (1.18)$$

where $\beta = \frac{2\mu p_0}{B_0^2}$ is the plasma beta. Due to the form of this term, if $\beta \ll 1$ then we can neglect the pressure gradient, and if $\beta \gg 1$ then we can neglect the Lorentz force (it is known that in the solar corona $\beta \ll 1$).

This reduces the equation of motion to,

$$\mathbf{j} \times \mathbf{B} = 0. \quad (1.19)$$

A special case occurs when $\mathbf{j} = \nabla \times \mathbf{B} = 0$, called a potential field.

1.3 Aims

In the work presented in this thesis, two coupled techniques will be used to investigate several properties of solar and rapidly rotating stellar magnetic fields. The first component will be a magnetic flux transport model, which will be used to model the time evolution of the photospheric field (see van Ballegooijen et al. (1998), discussed in Chapter 2). The second component is a potential field source surface model (PFSS, Schatten et al. (1969), discussed in Chapter 3) which extrapolates a global coronal magnetic field from a given photospheric flux distribution out to 2.5 solar radii.

Initially, the location and variation of coronal null points (points where $\mathbf{B} = 0$) will be investigated. To start with the magnetic flux transport model will be approximately matched to observations taken

from Kitt Peak by approximately matching magnetic flux levels at various latitudes between the simulations. When this idealized simulation is accurately matched, a potential coronal field is extrapolated at each time step. Each coronal field configuration of the simulation is then scanned for coronal null points using the trilinear technique of Haynes & Parnell (2007). The properties of these null points will be used to determine the dependence of coronal null points upon the overlying global dipole strength and the emerging photospheric magnetic flux. The photospheric field is then evolved forward using Equation 2.3, and a new coronal field extrapolated using the PFSS.

The locations of the coronal null points will then be taken, and a simple test applied in order to determine how many of the null points could, in principle, be able to breakout assuming the breakout model of Antiochos (1998). Here, we define the ability to breakout as the null point having more flux below than above and being able to, in principle, remove all of the overlying flux via reconnection at the coronal null point. To do this the amount of flux above and below the null point is calculated. If the amount of flux below the null point is greater than above, then all of the flux above the null point may be removed, in principle, via reconnection between the two regions, which will allow the flux below the null point to escape from the solar corona and produce a CME. If there is more flux above the null point than below then the overlying magnetic field will not be removed via reconnection at the null point. This means that the underlying magnetic flux will be restricted from possible breakout through the overlying magnetic field. Here, no ejection will occur under the breakout principle.

Following from this, a simulation is then run using the Kitt Peak magnetograms themselves as a base boundary condition for the coronal field extrapolation. This is then scanned for the location and variation of coronal null points. This simulation is compared to the previous simulations, where the simulated photospheric surface is used, in order to determine whether, in the idealized simulations, the variation of coronal null points has been accurately modeled and determined.

Finally, the radial surface evolution code is modified such that rapidly rotating stars can be considered. This is done by changing the rate of differential rotation and meridional circulation and approximately matching the orientation of the radial magnetic field on the surface to observations of faster rotating stellar bodies, more specifically HD171488.

The work in this thesis is ordered as follows: in Chapter 2, a description of the Magnetic Flux Transport Model is given. This will include the equations to be used to model all aspects of the radial

surface field and several initial runs which will illustrate our understanding of the transport and evolution of magnetic flux on the solar surface and how the initial properties of bipoles affect this. A description of the Kitt Peak magnetograms, which are used to match flux levels of the simulation, will also be given. In Chapter 3 a description of the potential coronal field extrapolation technique will be given along with the null point finding technique that will be used. Several simple examples of using the null finding technique are then described. In Chapter 4 the null finding technique is applied to two full solar cycles and a description of the variation and properties of coronal null points will be given. In Chapter 5 the locations of the previously calculated null points will be used in order to determine how many may be able to breakout, assuming the principles of the Breakout Model of Antiochos (1998). In Chapter 6 the Kitt Peak magnetograms will be used as a base boundary condition for potential field extrapolation. Each magnetogram will have the potential field extrapolation technique applied to it, and the location of coronal null points will then be determined for each coronal configuration. A comparison between these results and the simulation results described in Chapter 4 will allow us to determine if the general variation and properties of coronal null points has been accurately modeled in the idealized simulations. This work will allow us to compare the simulated results with observed results in order to deduce if the general properties of coronal null points have been deduced. In Chapter 7 the radial surface field evolution code is modified in an attempt to model the evolution of the radial surface field of rapidly rotating stellar bodies. This will be done through modification of the differential rotation and meridional flow rates. Chapter 8 contains key conclusions from throughout the thesis along with future work.

Surface Flux Transport Model for the Radial Magnetic Field

The study of coronal null points, locations where $\mathbf{B} = \mathbf{0}$ in the solar atmosphere, is currently a key area of research in solar physics. Null points are of interest as they are sites where magnetic reconnection can take place and therefore of energy release within the solar atmosphere (Priest et al., 2003; Pontin et al., 2004; Aulanier et al., 2005; Pariat et al., 2006). The properties and existence of coronal null points depend on the complex nature of the magnetic field distribution at the solar photosphere. This distribution may be mathematically prescribed as a boundary condition in magnetic field extrapolation techniques. Many studies have considered the existence and properties of coronal null points either through considering theoretical configurations (Parnell et al., 1996, 1997; Brown & Priest, 1999, 2001; Beveridge et al., 2002, 2004; Parnell & Galsgaard, 2004; Parnell et al., 2008) or through direct extrapolation of observed magnetograms (Longcope et al., 2003; Démoulin, 2005; Maclean et al., 2005; Démoulin, 2006; Longcope & Beveridge, 2007; Régnier et al., 2008; Longcope & Parnell, 2009). To date, most of these studies of coronal null points have been carried out under the potential field approximation and in a local Cartesian frame of reference. A few studies have also considered the existence of coronal null points in spherical geometry due to a few sources (Maclean et al., 2006a,b; Maclean & Priest, 2007) or in non-potential magnetic field distributions.

In the work presented here, the location and variation of coronal null points with time will be investigated using a surface flux transport simulation of the radial magnetic field B_r as the photospheric base

boundary condition over 2 solar cycles. From this boundary condition, a potential coronal field is then extrapolated out to $2.5R_{\odot}$. At $2.5R_{\odot}$, the outer boundary condition that $B_{\theta} = B_{\phi} = 0$ is applied and the field becomes purely radial. This is to simulate the strong effects of the solar wind at this point. As the base boundary condition is evolved forward in time a new coronal field is extrapolated every 27 days. Each coronal field is scanned using the trilinear null finding technique of Haynes & Parnell (2007), adapted for spherical coordinates. The resulting properties of the coronal null points will provide the basis for several investigations within this thesis.

In this section a description of the radial surface transport simulation used to produce the lower boundary condition is given. Several simple examples are presented in order to understand the effects of the various surface flows and how the properties of the magnetic bipoles, such as their tilt angle and latitude of emergence, affect the evolution of the radial surface field.

2.1 Surface Flux Transport Simulation: Basic Equations

The time dependent evolution of the magnetic field is modelled using the magnetic induction equation. That is,

$$\frac{\partial \mathbf{B}}{\partial t} = \nabla \times (\mathbf{v} \times \mathbf{B}) + \eta \nabla^2 \mathbf{B}. \quad (2.1)$$

In this equation \mathbf{v} represents the plasma velocity, which will be imposed using the various surface flows, η the magnetic diffusivity, t is time and \mathbf{B} , the magnetic field. The magnetic diffusivity can simply be written as $\eta = D$, the photospheric diffusion constant, due to the evolution of the radial magnetic field B_r being investigated at the solar surface. This also avoids any discontinuity in the radial component of the magnetic field developing just above the solar surface. Expanding this equation gives the equations for evolving forward all three components of the magnetic field with time. However, as only the time evolution of the radial magnetic field B_r is used as the base boundary condition, it is necessary to only calculate the equation for the evolution of this component as under certain conditions the evolution of B_r decouples from that of B_{θ} and B_{ϕ} . These conditions are when there is no vertical transport of the horizontal magnetic fields ($v_r = 0$) and no radial derivatives ($\frac{\partial}{\partial r} = 0$), which

means all of the field components evolve on a spherical shell ($\frac{\partial B_\theta}{\partial r} = \frac{\partial B_\phi}{\partial r} = 0$). It is important to note that our base boundary condition will be the time evolution of the radial magnetic field, therefore it is prudent to consider only the time evolution of B_r from this point on. Using Equation 2.1, with the decoupling conditions described here, and only looking at the radial term gives us,

$$\frac{\partial B_r}{\partial t} = \frac{1}{r} \frac{\partial}{\partial \theta} (v_r B_\theta - v_\theta B_r) - \frac{1}{r \sin \theta} \frac{\partial}{\partial \phi} (v_\phi B_r - v_r B_\phi) + \eta \left(\frac{1}{r^2 \sin \theta} \frac{\partial}{\partial \theta} \left(\sin \theta \frac{\partial B_r}{\partial \theta} \right) + \frac{1}{r^2 \sin^2 \theta} \frac{\partial^2 B_r}{\partial \phi^2} \right). \quad (2.2)$$

Magnetic flux at the solar surface evolves through the large scale processes of emergence, advection and surface diffusion, combined with some other processes, for example the coalescence (merging of) same sign features and cancellation of opposite polarity features. New flux emerges at the solar surface in the form of newly emerged bipolar regions (Archontis et al., 2004; Murray et al., 2006; Murray & Hood, 2007). Once emerged, the flux is evolved via large-scale flows such as differential rotation and meridional flow. The flux transport code used in this study includes these effects along with surface diffusion as a result of super-granular convection in order to evolve forward the radial component of the magnetic field at the solar surface (Wang et al., 1989; van Ballegoijen et al., 1998; Schrijver & Title, 2001; Baumann et al., 2006). A velocity is imposed at the solar surface ($r = R_\odot = 1$) which is based upon the surface flows of meridional circulation and differential rotation. We set $v_\theta = u(\lambda)$ and $v_\phi = \sin \theta \Omega(\theta)$, where $u(\lambda = 90 - \theta)$ is the meridional flow and $\Omega(\theta)$ is the differential rotation rate. The magnetic diffusivity is set to be the value of magnetic diffusion taken from previous studies by Wang et al. (1989) and van Ballegoijen et al. (1998). The exact value of the diffusion is taken to be $D = 450 \text{ km}^2 \text{ s}^{-1}$, as used in van Ballegoijen et al. (1998), which falls within the range of $600 \pm 200 \text{ km}^2 \text{ s}^{-1}$, obtained by Wang et al. (1989) and from here we rewrite $\eta = D$. This range was found by comparing observed and simulated properties of the large scale solar magnetic field. Substituting these terms into Equation 2.2 gives,

$$\frac{\partial B_r}{\partial t} = \frac{1}{\sin \theta} \frac{\partial}{\partial \theta} (\sin \theta (-u B_r + D \frac{\partial B_r}{\partial \theta})) - \Omega(\theta) \frac{\partial B_r}{\partial \phi} + \frac{D}{\sin^2 \theta} \frac{\partial^2 B_r}{\partial \phi^2}. \quad (2.3)$$

Using this equation, the radial term of the magnetic field is evolved forward at the solar surface, where the effects of meridional flow, differential rotation and a constant surface diffusion are included. We

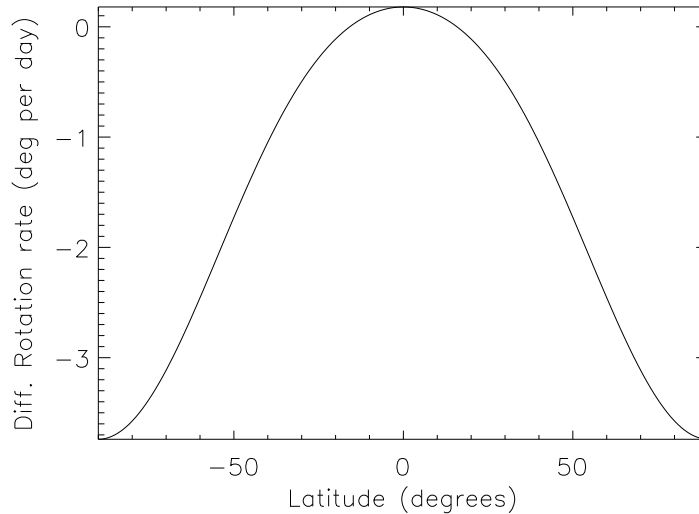


Figure 2.1: Graph showing a plot of the rate of differential rotation versus latitude. The Carrington rotation rate has been taken off in order to account for a non-moving frame of reference within our simulation.

only investigate this term, as the bas boundary condition for potential field extrapolation is taken to be the evolution of the radial magnetic field at the solar surface. Full details for the derivation of B_r , B_θ and B_ϕ at all heights within the solar corona are given in Chapter 3. The profile of differential rotation used within Equation 2.3 is taken from Snodgrass (1983),

$$\Omega(\theta) = 13.38 - 2.30 \cos^2 \theta - 1.62 \cos^4 \theta - \Omega_0(\text{deg/day}), \quad (2.4)$$

where Ω_0 is the Carrington rotation rate ($=13.20 \text{ deg day}^{-1}$). Figure 2.1 shows a plot of the rate of differential rotation. It can be seen that at higher latitudes the magnitude of differential rotation is much greater than at lower latitudes. Closer to the equator, the magnitude of differential rotation is much slower. This profile produces the observed differential rotation on the sun. The rate of differential rotation at the polar region is approximately 30 days, while at the equator it is 26 days, this gives a timescale for differential rotation of $\tau_{dr} = \frac{2\pi}{\Omega(\frac{\pi}{2}) - \Omega(0)} \approx 0.25$ years. The Carrington rotation rate accounts for a moving frame of reference within the simulation. The meridional flow profile, given as a function of latitude ($\lambda = \frac{\pi}{2} - \theta$), is given by:

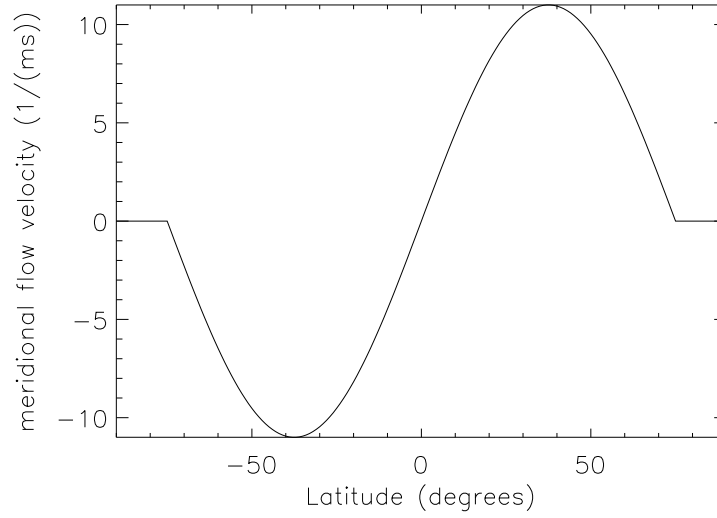


Figure 2.2: Graph showing a plot of the meridional flow rate versus latitude. The meridional flow rate follows the behaviour of a sine curve, and can be seen to vanish above $\lambda_o = 75^\circ$ latitude.

$$u(\lambda) = \begin{cases} -u_o \sin(\pi\lambda/\lambda_o) & |\lambda| < \lambda_o, \\ 0 & \text{otherwise,} \end{cases} \quad (2.5)$$

where, above λ_o the meridional flow vanishes. In these simulations we take $\lambda_o = 75^\circ$ and $u_o = 11\text{m/s}$, as used in van Ballegoijen et al. (1998). This gives a timescale of meridional flow, $T_u = \frac{R_\odot}{u_o} \approx 2$ years. Figure 2.2 shows a plot of the profile of meridional flow on the sun versus latitude. The magnitude of the flow rate increases as you move away from the equator, until approximately $\pm 37.5^\circ$. Above this latitude the magnitude of the meridional circulation decreases until λ_o is reached, at which point the meridional circulation vanishes. This follows the general behaviour of a sine curve.

In the next section we will consider how we will represent the radial magnetic field on the surface of the sun through the use of spherical harmonic functions.

2.1.1 Basics of Spherical Harmonics

Spherical harmonics, which are the solutions to the angular section of Laplace's equation, may be used to represent any function on the surface of a sphere. This set of equations forms an orthogonal

system first calculated by Pierre Simon De Laplace in 1783. Each representation of a sphere using spherical harmonics has various nodal lines indicating a sign change and hence zeros present in the system. The harmonics take the form of:

$$Y_{lm}(\theta, \phi) = \sqrt{\frac{2l+1}{4\pi} \frac{(l-m)!}{(l+m)!}} Q_l^m(\cos \theta) e^{im\phi}, \quad (2.6)$$

where l is the mode number (i.e. the total number of nodes), m indicates the azimuthal mode number and $Q_l^m(\cos \theta)$ are the associated Legendre polynomials. The Legendre polynomials are an orthogonal set of equations, taking the form:

$$Q_l^m(x) = \frac{(-1)^m}{2^l l!} (1-x^2)^{\frac{m}{2}} \frac{d^{l+m}}{dx^{l+m}} (x^2-1)^l, \quad (2.7)$$

where, after calculating the appropriate derivative which is dependent upon the values of l and m used, we substitute in $x = \cos \theta$. Each of the associated Legendre polynomials has $(l-m)$ zeros located within the range $0 < \theta < \pi$.

Figure 2.3 shows plots of the Legendre polynomials as l is increased from 1 to 3 and m is increased from 0 to l . Each of the plots shows that as m increases then the number of zeros located on each plot decreases to $l-m$, as previously noted. These polynomials, combined with the coefficients from the spherical harmonics and $e^{im\phi} = (\cos \phi + i \sin \phi)$ give the spherical harmonics portion of our magnetic field representation.

Figures 2.4, 2.5 and 2.6 show images of the spherical harmonics as a function of θ and ϕ as l is increased from 1 (Figure 2.4) to 3 (Figure 2.6) and m is increased from 0 to l . It can clearly be seen that, if $m=0$, the number of zeros in the θ direction is equal to l , while there are no zeros in the ϕ direction. As m increases, the number of zeros in the θ direction decreases to $l-m$, while the number of zeros in the ϕ direction between $0 < \phi < \pi$ increases by m . The pattern then repeats itself between $\pi < \phi < 2\pi$. As l is increased beyond 3 (in our simulations we take $l = 64$), more complex field configurations are created, which may be used to represent smaller scale magnetic features. A key point of these plots is that the harmonics represent an azimuthally symmetric system. Each plot shows symmetry about the $\phi = 180^\circ$ line. When $l = 1, m = 0$, we have a basic N-S (axisymmetric) dipole

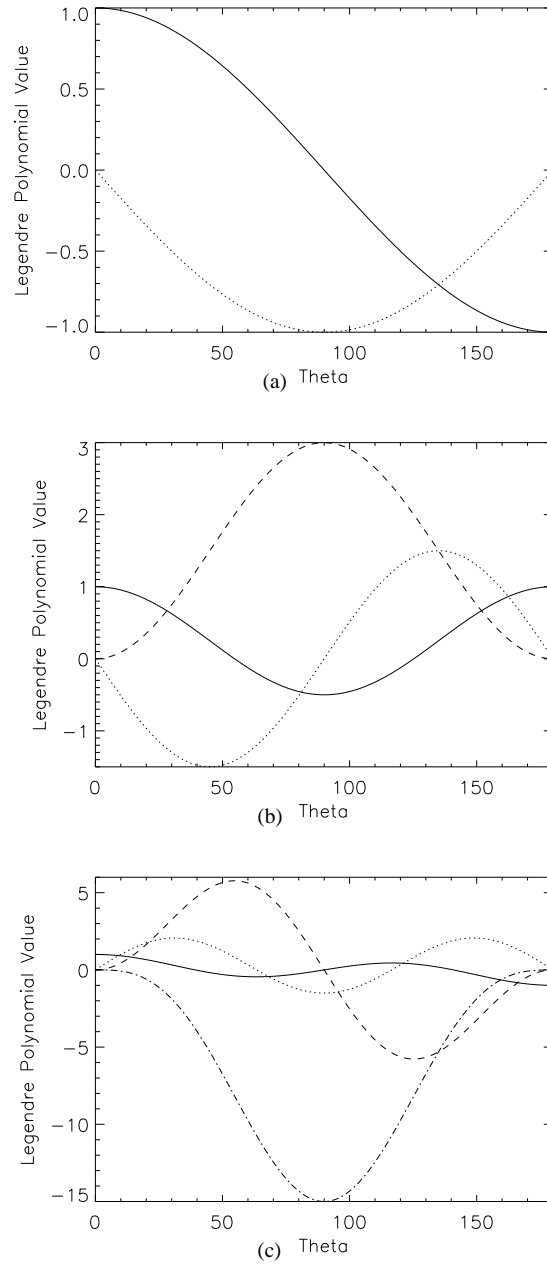


Figure 2.3: Plots showing the Legendre polynomials. Graph (a) shows when $l=1$, (b) has $l=2$ and (c) has $l=3$. As m increases from 0 to l the various forms of the Legendre polynomials are plotted. $m = 0$ is represented by the solid line and $m = 1$ is the dotted line. Where appropriate, $m = 2$ is the dashed line and $m = 3$ is the dash-dotted line.

and when $l = 1, m = 1$ we have an E-W (non-axisymmetric) dipole.

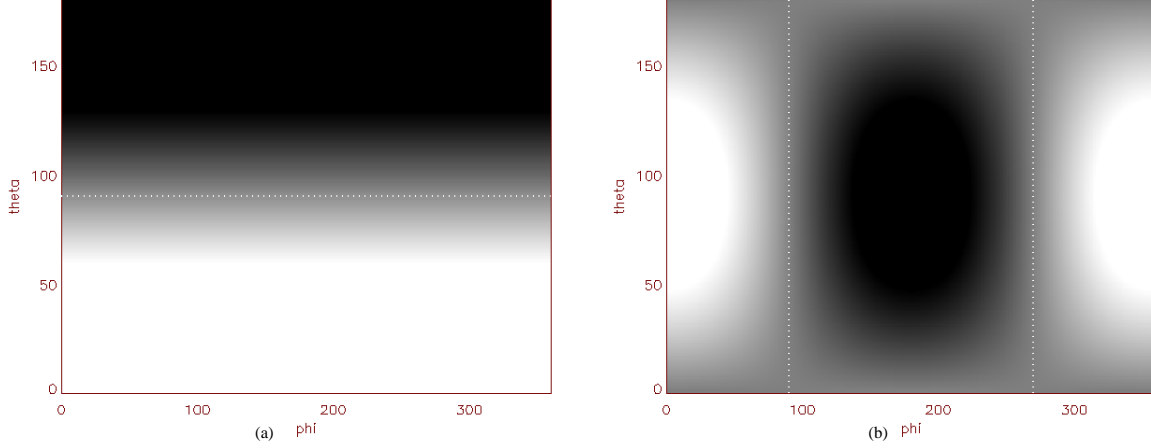


Figure 2.4: Images showing the spherical harmonics when $l=1$ and m is (a)0 (b)1. White represents positive values and black represents negative values. The dashed white lines on the images indicates the zeros between the positive and negative regions.

2.1.2 The One Component Model

The radial component of the magnetic field at the solar surface $B_r(r = R_\odot, \theta, \phi, t)$ may be represented using the previously described spherical harmonics, combined with a mode amplitude term. This gives $B_r(R_\odot = 1, \theta, \phi, t) = \sum_{m=-n}^n \sum_{l \geq |m|} B_{lm}(R_\odot = 1, t) Y_{lm}(\theta, \phi)$, where n tells us the number of horizontal zeros used within the harmonic configuration, B_{lm} represents the mode amplitudes and $Y_{lm}(\theta, \phi) = Q_l^m(\theta) e^{im\phi}$ represent the spherical harmonic components. While this is the decomposition of one field component at one radii, the full solution to obtaining all three magnetic field components at all radial heights within the simulation is presented in Section 3.1. As the base boundary condition is taken to be the time evolution of the radial magnetic field B_r , at the solar surface $R_\odot = 1$, the form for B_r given above is substituted into Equation 2.3. This gives,

$$\begin{aligned}
 \sum_{m=-n}^n \sum_{l \geq |m|} \frac{\partial B_{lm}(R_\odot, t)}{\partial t} Q_l^m(\theta) e^{im\phi} &= \sum_{m=-n}^n \sum_{l \geq |m|} \left(\frac{1}{\sin \theta} \frac{\partial}{\partial \theta} \left[\sin \theta (-u B_{lm}(R_\odot, t) Q_l^m(\theta) \right. \right. \\
 &\quad \left. \left. + D B_{lm}(R_\odot, t) \frac{\partial Q_l^m(\theta)}{\partial \theta} \right) e^{im\phi} \right) \\
 - \sum_{m=-n}^n \sum_{l \geq |m|} (\Omega(\theta) i m B_{lm}(R_\odot, t) Q_l^m(\theta) &+ \frac{D m^2}{\sin^2 \theta} B_{lm}(R_\odot, t) Q_l^m(\theta)) e^{im\phi}. \tag{2.8}
 \end{aligned}$$

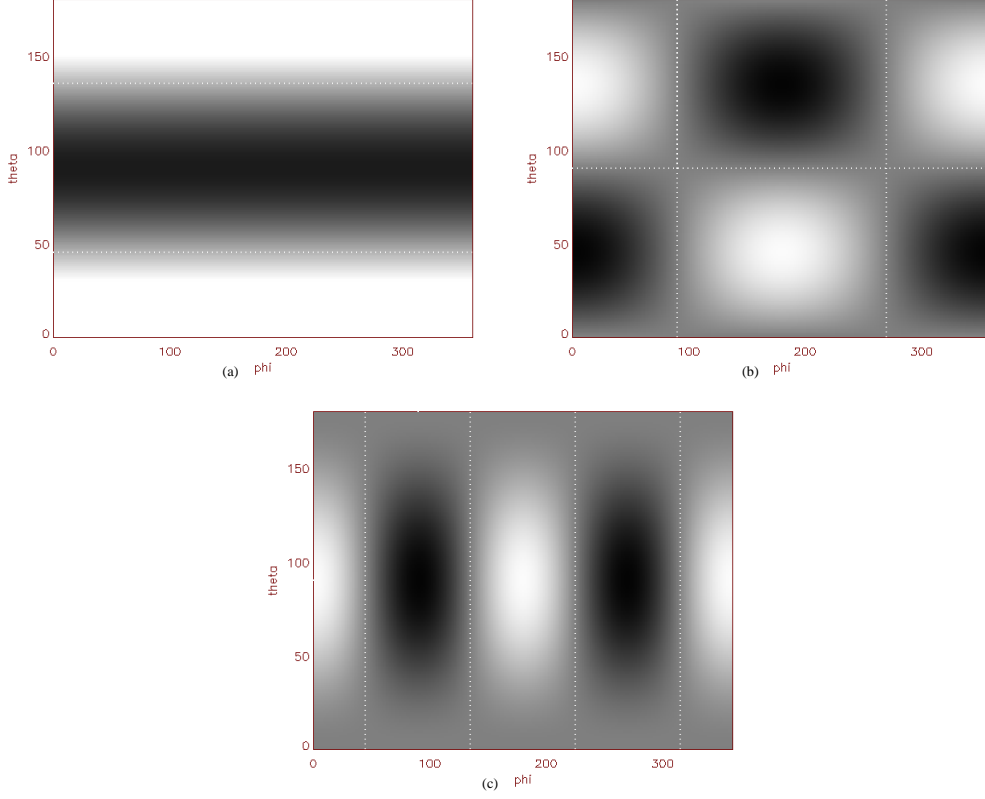


Figure 2.5: Images showing the spherical harmonics, when $l = 2$ and m is (a)0, (b)1 and (c)2. White represents positive values and black represents negative values. The dashed white lines on the images indicates the zeros between the positive and negative regions.

In this equation all of the terms containing a diffusion term (i.e. D), take the form of a Laplacian $\left(\frac{1}{\sin\theta} \frac{\partial}{\partial\theta} \left(\sin\theta \frac{\partial Q_l^m(\theta)}{\partial\theta}\right) + \left(\lambda_l - \frac{m^2}{\sin^2\theta}\right) Q_l^m(\theta) = 0\right)$, where $\lambda_l = l(l+1)$. This has the property that $\nabla^2(Q_l^m(\theta)e^{im\phi}) = \lambda_l Q_l^m(\theta)e^{im\phi}$. To take advantage of this property, group together all of the diffusion terms and all of the non diffusion terms. This gives:

$$\begin{aligned}
\sum_{m=-n}^n \sum_{l \geq |m|} \frac{\partial B_{lm}(R_\odot, t)}{\partial t} Q_l^m(\theta) e^{im\phi} &= \sum_{m=-n}^n \sum_{l \geq |m|} \left(\left(\frac{1}{\sin\theta} \frac{\partial}{\partial\theta} \left[\sin\theta (-u) B_{lm}(R_\odot, t) Q_l^m(\theta) \right] \right. \right. \\
&\quad \left. \left. - \Omega(\theta) i m B_{lm}(R_\odot, t) Q_l^m(\theta) \right) e^{im\phi} \right. \\
+ \sum_{m=-n}^n \sum_{l \geq |m|} \left(\left(\frac{1}{\sin\theta} \frac{\partial}{\partial\theta} \left[\sin\theta \frac{\partial Q_l^m(\theta)}{\partial\theta} \right] - \frac{m^2}{\sin^2\theta} Q_l^m(\theta) \right) D B_{lm}(R_\odot, t) e^{im\phi} \right). &\quad (2.9)
\end{aligned}$$

The diffusion terms can now be simplified to $\sum_{m=-n}^n \sum_{l \geq |m|} (-\lambda_l) D Q_l^m(\theta) B_{lm}(R_\odot, t) e^{im\phi}$.

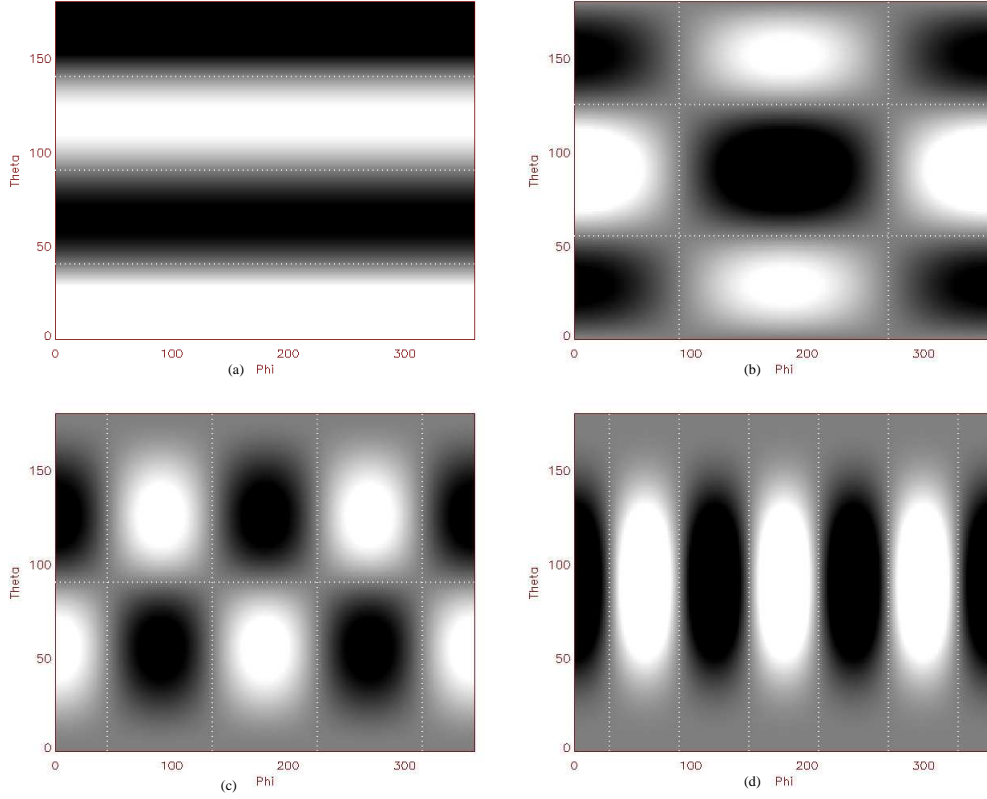


Figure 2.6: Images showing the spherical harmonics, when $l = 3$ and m is (a)0, (b)1, (c)2 and (d)3. White represents positive values and black represents negative values. The dashed white lines on the images indicates the zeros between the positive and negative regions.

The second property that we can use is the orthogonality relation of the Legendre polynomials. This states that:

$$2\pi \int_0^\pi Q_l^m(\theta) Q_n^m(\theta) \sin \theta d\theta = \begin{cases} 1 & l = n \\ 0 & \text{otherwise,} \end{cases} \quad (2.10)$$

In order to use the orthogonality relation, calculate an integral of the form $\int_0^\pi A Q_m^n(\theta) \sin \theta d\theta$, where A is Equation 2.9. Each term can then be evaluated over the integral and, where possible, simplified using the orthogonality relation. This gives, for each of the terms,

$$\sum_{m=-n}^n \sum_{l \geq |m|} \int_0^\pi \frac{\partial B_{lm}(R_\odot, t)}{\partial t} Q_l^m(\theta) Q_m^n(\theta) \sin \theta e^{im\phi} d\theta = \sum_{m=-n}^n \frac{1}{2\pi} \frac{\partial B_{nm}(r, t)}{\partial t} e^{im\phi},$$

$$\sum_{m=-n}^n \sum_{l \geq |m|} \int_0^\pi (-\lambda_l) D B_{lm}(R_\odot, t) e^{im\phi} Q_l^m(\theta) Q_m^n(\theta) \sin \theta d\theta = \sum_{m=-n}^n \frac{(-\lambda_n) D B_{nm}(r, t)}{2\pi} e^{im\phi},$$

$$\sum_{m=-n}^n \sum_{l \geq |m|} \int_0^\pi \frac{\partial}{\partial \theta} \sin \theta (-u) B_{lm}(R_\odot, t) Q_l^m(\theta) Q_m^n(\theta) e^{im\phi} d\theta = \sum_{m=-n}^n \sum_{l \geq |m|} B_{lm}(R_\odot, t) \times \int_0^\pi u Q_l^m(\theta) \frac{\partial Q_m^n(\theta)}{\partial \theta} \sin \theta d\theta e^{im\phi},$$

$$\sum_{m=-n}^n \sum_{l \geq |m|} im \int_0^\pi \Omega(\theta) B_{lm}(R_\odot, t) e^{im\phi} Q_l^m(\theta) Q_m^n(\theta) \sin \theta d\theta = \sum_{m=-n}^n \sum_{l \geq |m|} im B_{lm}(R_\odot, t) \times \int_0^\pi \Omega(\theta) Q_m^n(\theta) Q_l^m(\theta) \sin \theta d\theta e^{im\phi}.$$

The $e^{im\phi}$ term is eliminated in each term of the equation and two new variables are defined. Namely,

$$\begin{aligned} F_{l,n,m} &= 2\pi \int_0^\pi u Q_l^m(\theta) \frac{\partial Q_m^n(\theta)}{\partial \theta} \sin \theta d\theta \\ G_{l,n,m} &= 2\pi \int_0^\pi \Omega(\theta) Q_l^m(\theta) Q_m^n(\theta) \sin \theta d\theta. \end{aligned} \quad (2.11)$$

This means that the equation for evolving forward any single mode amplitude term of the expansion of the magnetic field at the solar surface is given by,

$$\frac{\partial B_{nm}(R_\odot, t)}{\partial t} = \sum_{l \geq |m|} (F_{l,n,m} - im G_{l,n,m} - \lambda_n D \delta_{l,n}) B_{lm}(R_\odot, t). \quad (2.12)$$

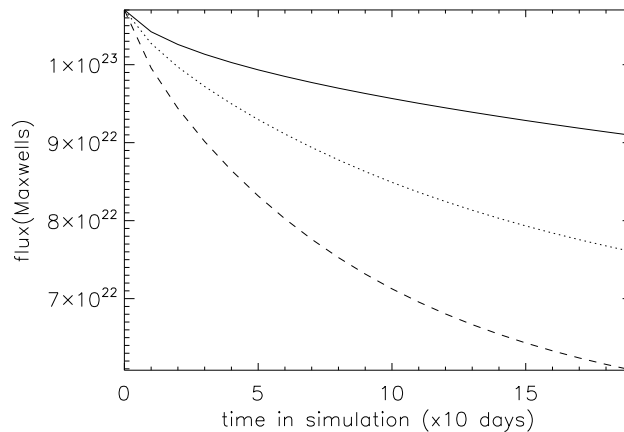


Figure 2.7: Image showing the variation in surface flux when a single bipole is inserted and meridional flow and differential rotation are both neglected. The solid line shows what happens when $n=1$, the dotted line indicates when $n=2$ and the dashed line indicates when $n=3$. The y axis is plotted in terms of tens of days, i.e. 5=50 days.

Here, F and G describe the effect of meridional flow and differential rotation respectively and $\delta_{l,n}$ is the Kronecker delta function, which is 1 if $l = n$ and 0 everywhere else. The equation shows that in order to evolve forward the radial component of the magnetic field at the solar surface, we need only evolve forward the mode amplitudes $B_{nm}(R_{\odot}, t)$ at the solar surface. The equation shows that individual modes diffuse independently of one-another but are coupled through the effects of differential rotation and meridional flow.

2.1.3 Solution With Only Diffusion

In Equation 2.12 the terms including meridional flow and differential rotation can be neglected in order to understand the effects of the spherical harmonic degree (n) on the rate of diffusion within the simulation. Setting $F_{l,n,m} = G_{l,n,m} = 0$ gives the equation,

$$\frac{\partial B_{nm}(R_{\odot}, t)}{\partial t} = -\lambda_n D B_{nm}(R_{\odot}, t). \quad (2.13)$$

Using separation of variables, this equation can be solved to give $B_{nm}(R_{\odot}, t) = A e^{-\lambda_n D t}$, where A is a constant of integration, $\lambda_n = n(n + 1)$ and n indicates the mode number used when creating the spherical harmonics. The equation indicates that the mode amplitudes decay exponentially with

time, with higher λ_n values decaying faster. Figure 2.7 shows a plot of the radial surface flux when a single spherical harmonic is inserted for n ranging from 1 to 3. As n increases, flux decays faster. This is because as n increases, so does the number of nodes. Each node represents a position where flux cancellation can take place. As the number of these increase, the rate of decrease of the mode amplitudes also increases.

2.2 Test Simulation Run Results

In order to test the simulation code and gain a better understanding as to the factors which effect the evolution of magnetic flux on the sun, three simulations are run. The first involves a single bipolar active region, with an initial flux of approximately $1.72 \times 10^{22} \text{Mx}$, inserted at approximately 7° latitude. The initial tilt angle of this bipole is varied from -30° to 30° , and the simulation run for 900 days. The second simulation involves emerging a bipole with a fixed tilt angle (approximately 15°). The latitude of emergence of this bipole was then varied from 5° latitude to 40° latitude between simulations. The third simulation involves emerging a single bipolar active region and modifying the peak rate of meridional circulation from 11ms^{-1} to 35ms^{-1} , which modifies the rate of meridional circulation over the entire sun. This will give an understanding as to how meridional circulation will affect the evolution of magnetic flux. These three simulations will provide a basic understanding of the evolution of magnetic flux on the solar surface as a consequence of tilt angle variation, latitude of emergence and the rate of poleward transport due to meridional flow and will allow us to see how slight variations in these factors can have a big effect upon the calculated variation within our code.

Figure 2.8 shows images taken at various time steps within the test simulations. Images (a), (b) and (c) are from a simulation with a positive tilt angle of 15° , while (d), (e) and (f) are from a simulation with a negative tilt angle or -15° . The images are taken from day 0 ((a) and (d)), day 100 ((b) and (e)) and day 500 ((c) and (f)) of the simulations. When the bipole has a positive tilt angle, the leading, negative polarity is closer to the equator and the trailing positive polarity is closer to the polar region (2.8(a)). As the effects of differential rotation and meridional flow evolve the bipole forward, the trailing polarity heads polewards at a faster rate than the leading polarity (2.8(b)). This results in more of a latitudinal shear in the trailing polarity than the leading polarity as when its latitude increases it moves into a region of greater gradient of differential rotation. It is also clear that, as the

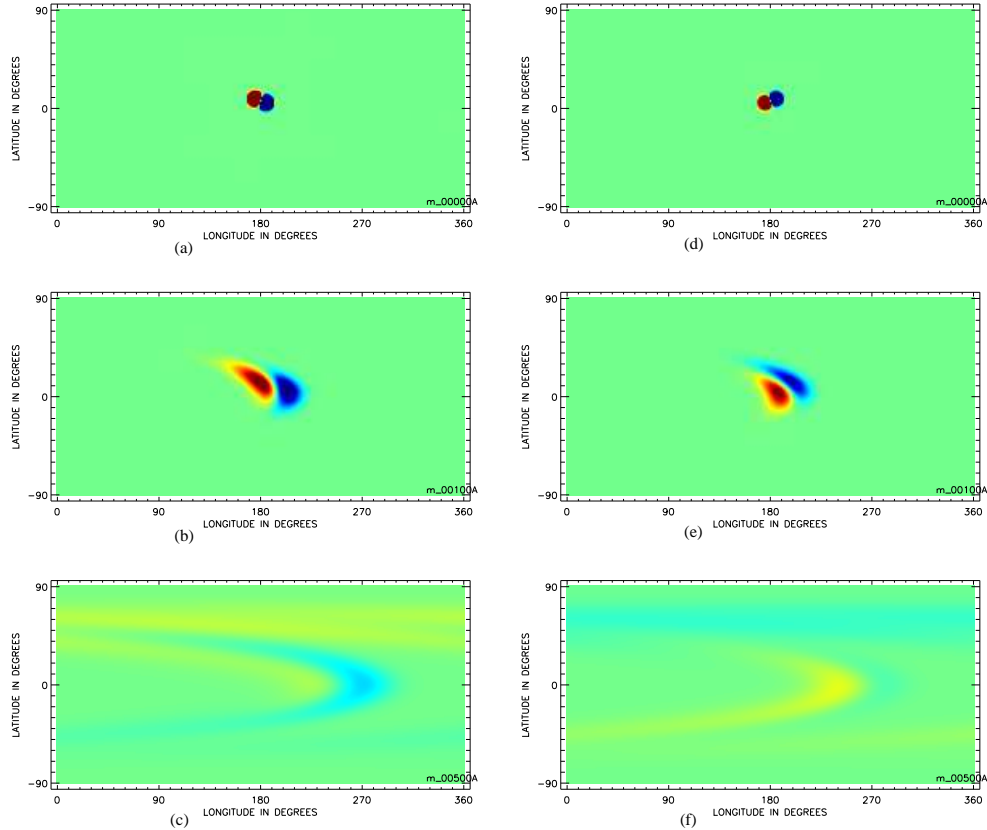


Figure 2.8: Images showing the time evolution of a single emerged bipole when surface field effects are included at 0 days ((a) and (d)), 100 days ((b) and (e)) and 500 days ((c) and (f)). Images (a), (b) and (c) show these effects for a magnetic bipole with positive tilt angle, (d), (e) and (f) show the results when a negative tilt angle is used. In these images, the leading polarity is always negative, while the trailing polarity is always positive.

bipole is emerged at a lower latitude, some of the leading negative polarity is transported over the equator. This portion of the polarity will eventually become trapped in the south pole, forming the magnetic field in this region. As meridional flow continues to transport the trailing polarity polewards faster than the leading polarity, a portion of this polarity becomes trapped in the polar region (2.8(c)). This will then form the polar magnetic field within this region. Images (d), (e) and (f) show similar results, except the higher latitude polarity is the leading polarity due to the tilt angle of the bipole. The bipole has a negative tilt angle meaning the trailing, positive polarity is closer to the equator and the leading, negative polarity is closer to the polar region (2.8(d)). As the effects of differential rotation and meridional flow evolve the bipole forward, the leading polarity heads polewards at a faster rate than the trailing polarity (2.8(e)). This results in more of a latitudinal shear in the leading polarity than

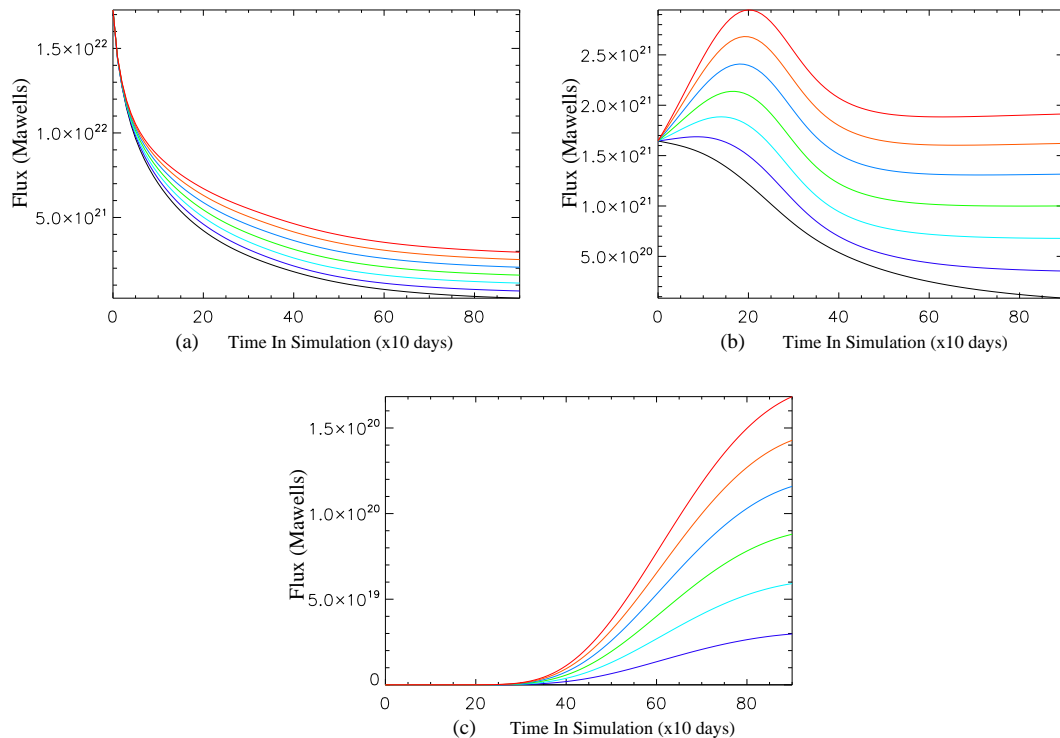


Figure 2.9: Images showing the evolution of (a) the surface magnetic flux, (b) open magnetic flux (the magnetic flux at $2.5R_{\odot}$) and (c) polar magnetic flux (i.e. flux between -90° and -70° or 70° and 90°), when a single magnetic bipole is inserted with no initial polar flux. These graphs indicate the results for when a positive tilt angle within the bipoles is used. The black line indicates a tilt angle of 0° , purple-blue indicates 5° , turquoise indicates 10° , green indicates 15° , blue indicates 20° , orange indicates 25° and red indicates 30° . In each of these simulation runs the leading polarity is negative, the trailing polarity is positive.

the trailing polarity. It is also clear that, as the bipole emerges at a lower latitude, some of the trailing negative polarity is transported over the equator. This portion of the polarity will eventually become trapped in the south pole, forming the magnetic field in this region. As meridional flow continues to transport the leading polarity polewards faster than the trailing polarity, a portion of this becomes trapped in the polar region (2.8(f)). This will then form the polar magnetic field within this region. This set of images show how the tilt angle of the bipole can effect the eventual evolution of the surface magnetic field on the sun.

Figures 2.9 and 2.10 show the results of varying the tilt angle of the bipole, where there is initially zero polar flux. Figure 2.9 shows the results when a positive tilt angle is used, Figure 2.10 shows the results when a negative tilt angle is used. In both of these sets of simulations, the parameters

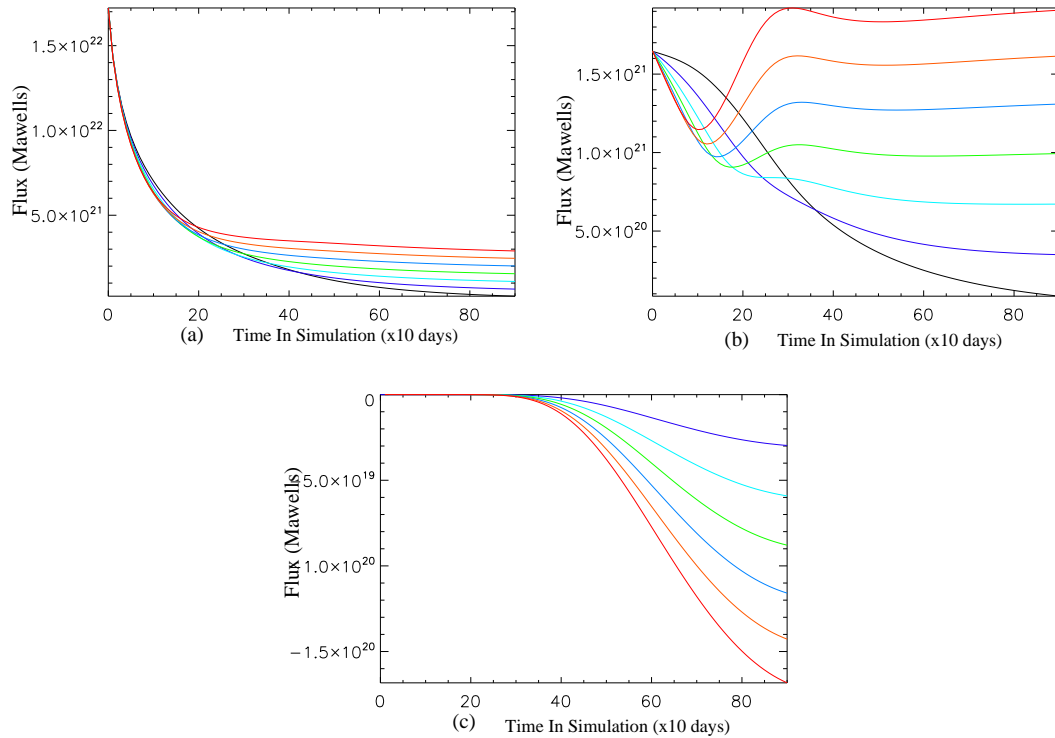


Figure 2.10: Images showing the evolution of (a) the surface magnetic flux, (b) open magnetic flux and (c) polar magnetic flux (i.e. flux between -90° and -70° or 70° and 90°), when a single magnetic bipole is inserted with no initial polar flux. These graphs indicate the results for when a negative tilt angle within the bipoles is used. The black line indicates a tilt angle of 0° , purple-blue indicates -5° , turquoise indicates -10° , green indicates -15° , blue indicates -20° , orange indicates -25° and red indicates -30° . In each of these simulation runs the leading polarity is negative, the trailing polarity is positive.

for meridional circulation, diffusion and differential rotation are the same as previously described in 2.1.2. Graph (a) in both figures shows that, as the magnitude of the tilt angle decreases, flux between the two polarities of the bipole cancel more rapidly. This results in a lower net end flux. This is due to the fact that the larger the tilt angle the less flux from the leading/trailing polarity that lie at a common latitude and can cancel with its opposite polarity. For large tilt angles the lower latitude polarity may diffuse across the equator, while the higher latitude polarity is carried polewards. These polarities then become separated due to meridional flow, and are unable to cancel out with one another.

Figure 2.9(b) shows the open flux (flux at $2.5R_\odot$) when positive tilt angles are used for the bipoles. Initially, there is a rise in the amount of open flux, peaking after approximately 200 days. This peak is higher for larger tilt angles. The level of flux then decreases slightly, eventually leveling off over

time. A higher, positive tilt angle means that the separation with latitude in the polarities of the two bipoles is larger. The lower latitude bipole rotates faster due to differential rotation and the two bipoles separate in longitude. It is this separation of the polarities that results in the increase of open flux. Figure 2.10(b) shows the corresponding result for negative tilt angles. It can be seen that there is an initial dip in open flux, before it increases slightly, where we observe more of an increase for a larger tilt angle. The amount of open flux then becomes almost constant. This initial dip is due to differential rotation forcing the two polarities together as now the following polarity lies at a lower latitude compared to the leading polarity. Once the following polarity rotates past the leading polarity the open flux may increase as their separation increases.

Graph (c) in Figures 2.9 and 2.10 shows the evolution of the polar flux in the northern hemisphere (i.e. flux between 70° and 90°) as we vary the tilt angle of the bipole. As the magnitude of the tilt angle increases, there is a larger net polar flux at the end of the simulation. This is due to less of the two polarities cancelling with each other prior to being transported into the polar regions. When there is a positive tilt angle, the trailing polarity is preferentially carried polewards, resulting in a positive flux of trailing polarity. When a negative tilt angle occurs, the leading polarity, which is now negative, forms the polar field. This is merely due to the orientation of the magnetic bipole emerged within these simulations. This explains the difference in sign of the polar flux when using either a positive or negative tilt angle.

A second set of simulations are run varying the latitude of emergence of the bipole (see discussion below and figure 2.11 for example images from these runs). Holding the tilt angle constant (at approximately 15°), the latitude of emergence was varied from 5° latitude to 40° latitude. A positive tilt angle is used as the majority of bipoles emerge with positive tilt angles. The same flux measurements as previous were then recorded and are presented in Figure 2.12.

Figure 2.11 shows images from various times in two simulations when a bipole emerges at 10° latitude (Images (a), (b) and (c)) and 40° latitude (Images (d), (e) and (f)) and evolved forward for 500 days. Images (a) and (d) show the initial set up on day 0 of both simulations. The emerged bipole can be seen to have a positive tilt angle (approximately 15°), with leading positive polarity, and trailing negative polarity. The difference between the two images can be seen as the bipole in image (d) emerges at a higher latitude than the bipole in image (a). Images (b) and (e) show the surface configuration

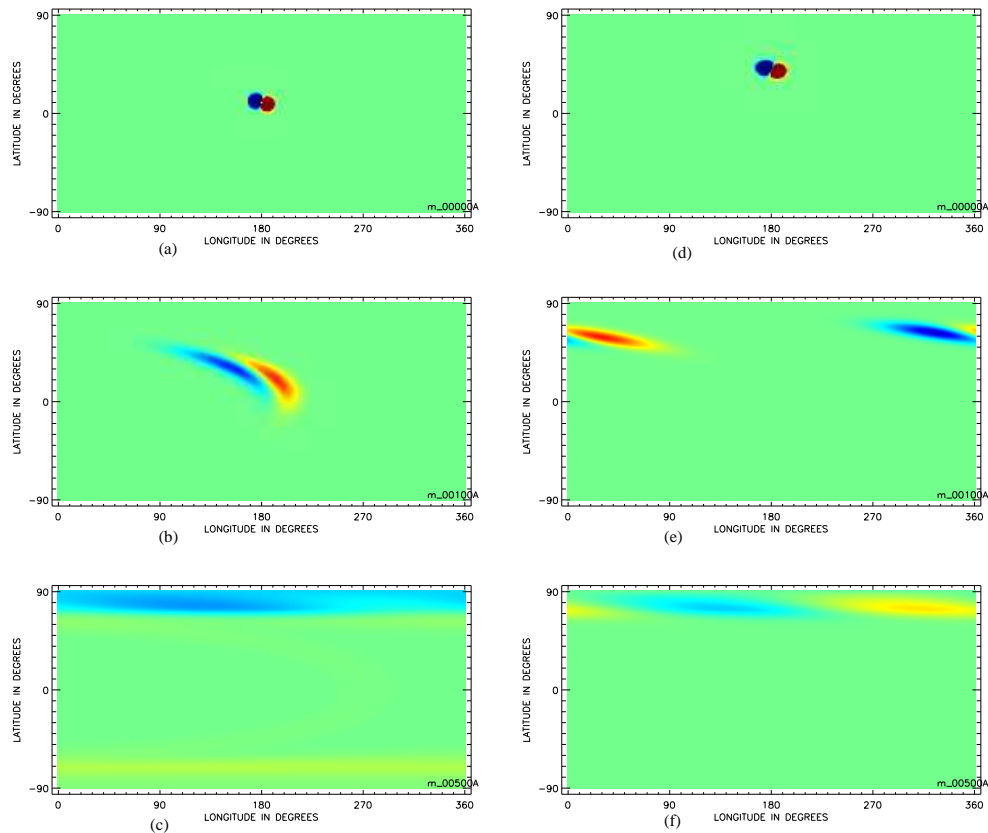


Figure 2.11: Images showing various time steps when a single bipole is emerged at 10° latitude ((a), (b) and (c)) and 40° latitude ((d), (e) and (f)). The bipole is then evolved forward in time. The images show the evolution of the magnetic bipole initially (Images (a) and (d)), after 100 days (Images (b) and (e)) and after 500 days (Images (c) and (f)). In all images red indicates positive magnetic field, blue indicates negative magnetic field.

after day 100. In Image (b), the magnetic bipole has been sheared in the East-West direction by the differential rotation. The trailing negative polarity is lying at a higher latitude than the positive polarity due to a combination of both the initial tilt angle of the bipole and the effect of meridional flow carrying this polarity polewards. The magnetic bipole emerges at a low enough latitude such as to allow some of the leading positive polarity to escape over the equatorial region. This magnetic flux will be carried towards the south pole due to meridional flow, and remain trapped in the south polar region. In image (e) slightly different effects can be seen due to the higher latitude of initial emergence of the magnetic bipole. At higher latitudes, the gradient of the differential rotation is higher, resulting in more of an effect on the surface magnetic field (see Equation 2.4 and Figure 2.1). This has caused the magnetic bipole to shear in an East-West direction and also appear to have moved,

within the frame of reference, around the sun. A key point of note within this image is that, due to a higher latitude of emergence, both polarities of the bipole are being carried towards the pole with no portion of either escaping over the equator. Images (c) and (f) show the surface field distribution after 500 days. In Image (c), the trailing negative polarity has become trapped in the north polar region, forming the field in this area. The leading positive polarity has also been transported towards this region, but lies at a lower latitude than the negative field. Meridional flow will continue to bring these two polarities together, causing cancellation between them until the stronger of the two fields (in this case the higher latitude negative field) completely cancels out the weaker of the two fields. A key point to note is that, in the south polar region there appears to be a small amount of the leading polarity. This originates from the magnetic flux from the leading polarity which escapes over the equator and is transported polewards by meridional flow, when the magnetic bipole emerges at lower latitudes. In image (f) both polarities of the magnetic bipole have been transported into the polar region. This is because both polarities emerge at sufficiently high latitudes such that none of the leading polarity is able to escape over the equator and be transported towards the southern polar region. This means that both polarities will become trapped within the northern polar region and will completely cancel with each other over time.

Figure 2.12(a) shows the evolution of the surface flux against time as the latitude of emergence is varied. There is initially a sharp decline in surface flux as the two polarities cancel with one another due to the small tilt angle. Meridional flow pushes the two polarities poleward however the leading polarity, which lies at a lower latitude may partially escape this effect and diffuse across the equator. However, the higher the latitude of emergence, the less the flux from the leading polarity can escape across the equator and the more flux from both polarities is pushed polewards. As more flux from both polarities is pushed polewards, a larger amount of cancellation may occur. This means that there is less flux at the end of the simulation.

Figure 2.12(b) shows the evolution of the open flux vs time as the latitude of emergence is varied. Initially the amount of open flux rises, peaking around day 150-200. This peak in open flux appears to be higher for a greater latitude of emergence up to approximately 25° latitude of emergence. At this point the size of the peak decreases as the latitude of emergence increases. The amount of open flux then decreases and levels off with time. The lower the latitude of emergence, the greater the open flux. This is due to more of the leading polarity being able to escape across the equatorial region the

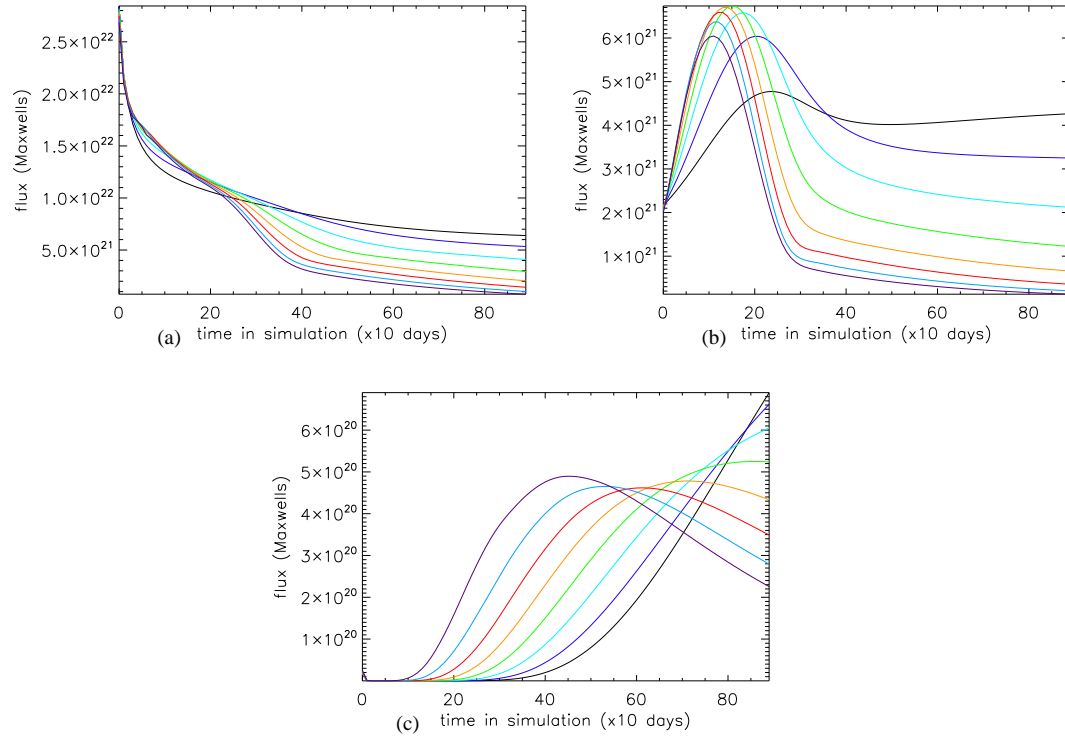


Figure 2.12: Graphs showing the evolution of (a) surface flux, (b) open flux and (c) polar flux when a single magnetic bipole is inserted, with no initial polar flux and an initial peak strength of approximately $2.8 \times 10^{22} \text{Mx}$, and the latitude of emergence of the bipole is varied from 5° to 40° . Each line indicates a different latitude of emergence for the magnetic bipole. Black indicates 5° latitude of emergence, dark blue shows 10° , pale blue shows 15° , green shows 20° , orange shows 25° , red shows 30° , blue shows 35° and purple shows 40° latitude of emergence. The tilt angle of the bipole is taken to be approximately 15° , the leading polarity is negative, while the trailing polarity is positive.

lower the latitude the bipole emerges. The peak in open flux as a function of latitude occurs for a latitude of emergence of around 25° as this is where differential rotation has its strongest gradient and the two polarities move faster apart.

Figure 2.12(c) shows the evolution of the polar flux against time as the latitude of emergence is varied. For a lower latitude of emergence, the polar flux begins to build up much later in the simulation. This is due to the polarities taking more time to reach higher latitudes and the polar region at the rate of meridional flow. As the latitude of emergence increases, more of the leading polarity will be transported into the polar region along with the following polarity. This means that more cancellation between the two polarities will occur within the polar field. The effect of this is such that, for a lower latitude of emergence, the end net polar flux will be higher.

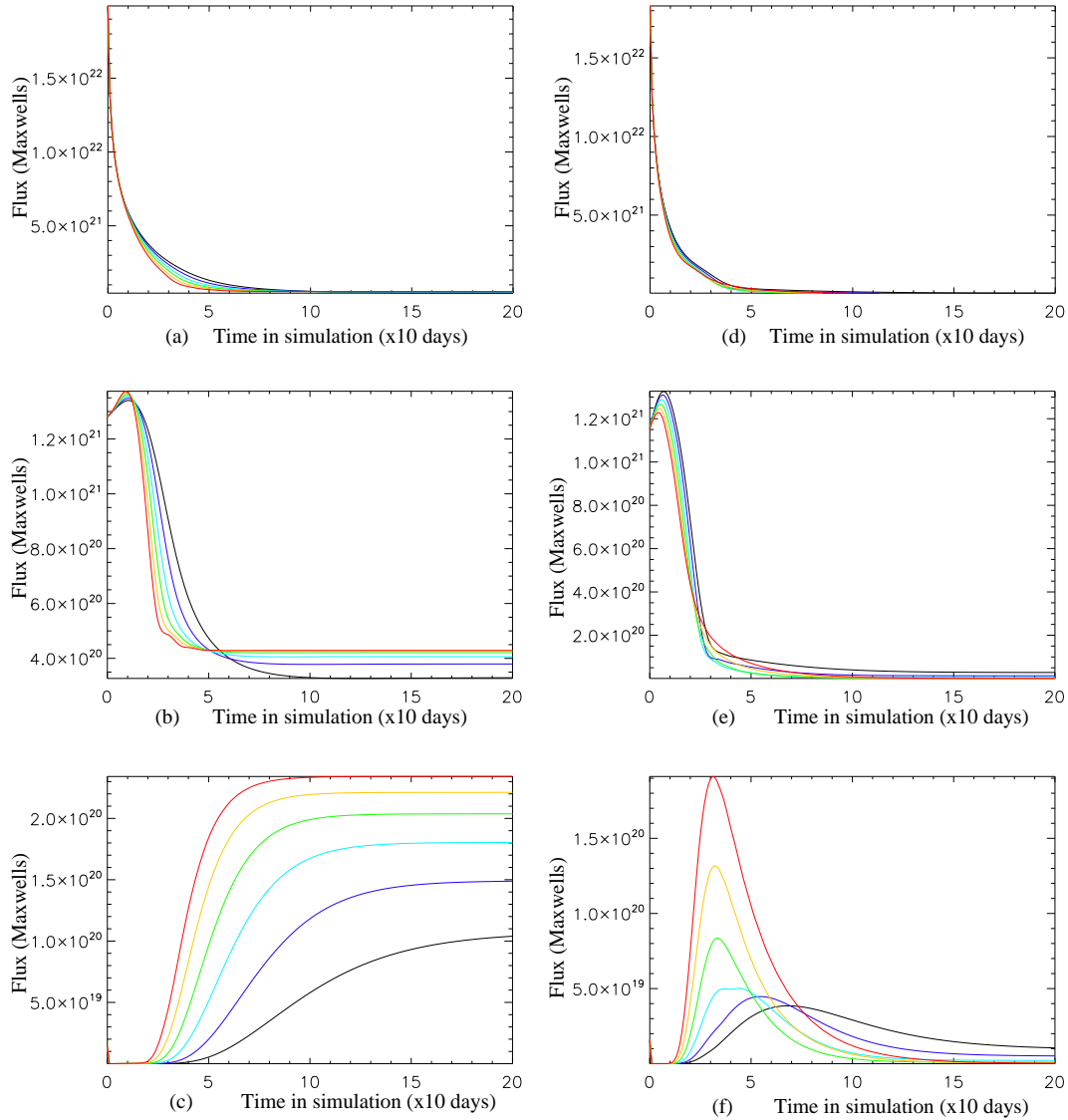


Figure 2.13: Graphs showing the variation in the amount of surface flux ((a) and (d)), open flux ((b) and (e)) and total polar flux within both north and south polar regions ((c) and (f)) when the meridional flow rate is altered for a bipole emerged at 5° latitude ((a), (b) and (c)) and 30° latitude ((d), (e) and (f)). Each line represents a different peak value of meridional flow: Black shows 11m/s, dark blue shows 15m/s, light blue shows 20m/s, green shows 25m/s, yellow shows 30m/s and red indicates 35m/s. Each bipole has a positive trailing polarity and a negative leading polarity, and is emerged with an initial tilt angle of 20° .

In order to understand the effects of meridional circulation, a third set of simulations are run. In these simulations, two sub-sets of simulations are considered. The first involves emerging a magnetic bipole at 5° latitude and varying the meridional flow rate. The second involves emerging a bipole at

30° latitude and varying the meridional flow rate. In both sets of simulations, the initial tilt angle of the bipole is 15°. In both sets of simulations the bipole is evolved forward for 200 days at each meridional flow rate, and the variation in surface, open and polar flux is recorded. These results are presented in Figure 2.13, where Graphs (a), (b) and (c) represent the results when the bipole is emerged at 5° latitude and (d), (e) and (f) represent the results when the bipole is emerged at 30° latitude.

Figure 2.13(a) shows the variation of surface flux when the meridional flow rate is altered for a bipole emerged at 5° latitude. Figure 2.13(d) shows the complementary graph when the bipole is emerged at 30° latitude. The surface flux initially decreases rapidly regardless of the peak rate of meridional flow used, or the latitude of emergence of the bipole. After about 50 days, the level of surface flux becomes fairly constant between simulations, with very little overall change between each simulation. The amount of surface flux continues to decrease, but at a much slower rate than initially. Comparing the final values of surface flux between the simulations shows that, for a lower latitude of emergence there is slightly more surface flux, in total, at the end of the simulation (approximately 5×10^{20} Mx). This is due to the fact that at a lower latitude of emergence some of the leading polarity is able to escape across the equator. This fraction of the polarity then becomes trapped in the southern pole but has no other flux with which to cancel. Hence, there will be a slightly higher value of flux for a lower latitude of emergence.

Figures 2.13(b) and 2.13(e) show the variation of open flux when the peak value of meridional circulation is changed for a bipole emerged at 5° latitude (2.13(b)) and a bipole emerged at 30° latitude (2.13(e)). When a bipole is emerged at lower latitudes, some of the leading polarity can escape across the equator. The remaining polarity in the northern hemisphere is then pushed polewards at a faster speed for a faster peak flow rate. This results in an earlier initial peak in open flux for a higher meridional flow. The level of open flux then decreases rapidly as cancellation occurs and eventually levels out over time. This is because eventually a portion of the leading polarity becomes trapped in the southern polar field, while a portion of the trailing polarity becomes trapped in the northern polar field. This results in open flux occurring from these polarities. For a bipole emerged at a higher latitude (Graph (e)), the variation of open flux occurs slightly differently. As the bipole is emerged at a higher latitude, less of the leading polarity is able to escape over the equator. As the rate of meridional circulation increases, the amount of flux from the bipole which may escape over the equator decreases. Higher meridional circulation means that less of the flux can escape over the equator into

the opposite hemisphere, resulting in less separation between the polarities and more cancellation occurring between them. This results in the smaller initial peak in open flux seen in the graph. As time continues, the amount of open flux drops rapidly and eventually becomes fairly constant over time. The drop occurs as both polarities are transported polewards and cancel with each other. For a lower peak meridional flow rate, the eventual flux level is higher due to slightly more of the leading polarity being able to escape over the equator for a slower rate of meridional flow.

Figures 2.13(c) and 2.13(f) show the variation of polar flux when the peak rate of meridional flow is changed for a bipole emerged at 5° latitude (2.13(c)) and a bipole emerged at 30° latitude (2.13(f)). When the bipole is emerged at a lower latitude (2.13(c)), more of the leading polarity can escape across the equator. This polarity then escapes to the opposite polar region and becomes trapped due to meridional flow. The remaining polarity fragments are transported to the northern polar region. In these simulations, the bipole is emerged so low that most of the leading polarity is able to escape across the equator into the southern hemisphere. As it escapes over the equator, the faster meridional flow rate pulls the polarity poleward at a faster rate. This means that more of both polarities will become trapped in the polar regions faster, hence a quicker and higher total polar flux occurring. When a bipole is emerged at a higher latitude (Figure 2.13(f)), less of the leading polarity is able to escape over the equator. This means that more of both polarities is transported polewards. However, a faster meridional flow means that this poleward transport occurs faster. Figure 2.13(f) shows that, for a faster meridional flow, the peak in polar flux happens quicker and occurs at a higher value. This is because more of both polarities are transported into the polar region, at a quicker rate. After the initial peak, the flux levels fall off rapidly. This is due to larger fractions of both polarities becoming isolated in the polar region and cancelling with one another. As the meridional flow rate drops, the peak in flux is lower due to more cancellation between the polarities occurring prior to their arrival in the polar region. The flux levels then decrease and level out over time. This decrease occurs more slowly for a slower meridional flow rate as less of the leading polarity is able to escape across the equator so more of both polarities become trapped within the polar region. Eventually, the flux levels become almost constant, but at a higher level for a lower meridional flow rate. This is due to the fact that less of the leading polarity is able to escape across the equator for a higher meridional flow rate. This means that there will be less of the leading polarity trapped in the southern polar field at the end of the simulation. Hence, a lower total polar flux.

Using the results from these simulations, the general behaviour of the emerging magnetic flux on the solar surface is understood. If a bipole has a larger positive/negative tilt angle this will mean that more of the trailing/leading polarity is able to be transported polewards by the meridional circulation. With a smaller tilt angle, differential rotation will bring more of the two polarities together causing them to cancel out. This means that less of the following/leading polarity will be transported polewards. The amount of flux from a bipole that reaches the polar region also depends upon the latitude of emergence of the bipole. If a bipole is emerged at a higher latitude then more of the leading polarity is carried polewards, along with the following polarity. This means that more cancellation will occur between these two polarities and the end net surface flux will be lower. Conversely, should a bipole emerge at a lower latitude, less of the leading polarity will be transported polewards as it may escape across the equator. This means that less cancellation will occur between the two polarities of the bipole. However, the escaping polarity may cancel out with other polarities in the opposite hemisphere. The rate of meridional flow is also one of the key factors in determining the correct evolution of magnetic flux on the solar surface. As shown in Figure 2.13, the evolution of the magnetic flux, especially the polar field, can vary greatly depending upon the peak value of meridional circulation chosen. Within the work shown here, the connection between the evolution of coronal null points and the overlying global dipole is to be investigated. This requires accurate modelling of the overlying magnetic dipole (polar) field. This means that the evolution of the polar flux within the simulation is a key point in understanding the connection between null points and the global dipole as the overlying global dipole originates from within this region. Consequentially, the evolution of the polar field must be modelled accurately. Therefore, the present understanding of the surface flows on the sun and the effects of the various properties of magnetic bipoles is essential.

2.3 Kitt Peak Synoptic Magnetogram Data

Kitt Peak synoptic magnetograms represent a monthly average of the Sun's global photospheric field and are created from NSO/KP normal component full disk magnetograms (Pierce et al., 1976). Each synoptic magnetogram represents one Carrington rotation (27 days) of measurements. An example of a Kitt Peak magnetogram is given in Figure 2.14. Synoptic magnetograms have been used for a variety of purposes, including the study of the 27 day period found on the Sun (the period with

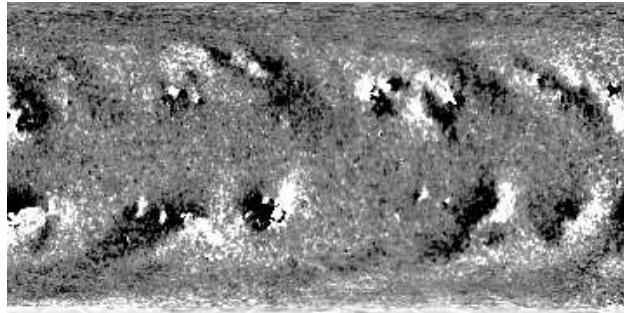


Figure 2.14: Image showing an example of one of the Kitt Peak magnetograms. Black indicates negative flux, white indicates positive flux.

which sunspots and solar features appear to rotate on the Sun) (Henney & Harvey, 2001), the study of coronal holes during solar maximum (Zhang et al., 2002), considering the origin of the hemispheric pattern of filaments (Mackay et al., 2000; Yeates et al., 2007, 2008) and in the study of the origin of CMEs (Yeates & Mackay, 2009).

When using the previously described radial surface field simulation, flux measurements of the radial surface magnetic field at various latitudes and over the whole solar surface are approximately matched with the radial field measurements calculated from Kitt Peak synoptic magnetograms. The Kitt Peak magnetograms are taken as line of sight measurements of the radial surface magnetic field on the sun via the NSO Vacuum Telescope located on Kitt Peak, Arizona. Due to seeing angle effects they will be more accurate closer to the equator. However, at higher latitudes the measurements will be inaccurate. Figure 2.15 shows an example of how the measurements from Kitt Peak are obtained. The radial field direction at the equator falls onto the line of sight of the instrument. This means these measurements will be accurate. However, at higher latitudes there is a greater angle between the measured line of sight component and the actual radial field component. This inaccuracy increases as the measurements are obtained for higher latitudes. This inaccuracy means that the Kitt Peak measurements of the polar fields, and hence overlying global dipole, may be inaccurate. Due to this, Kitt Peak magnetograms are not directly used as a photospheric boundary condition. Given the nature of this investigation, the accurate modelling of the polar field is essential.

However, despite the inaccuracies at higher latitudes, the Kitt Peak magnetograms still prove an essential component of the investigation. Given their accuracy at lower latitudes it is prudent to create our radial surface field simulation such that the magnitude and evolution of magnetic flux at lower

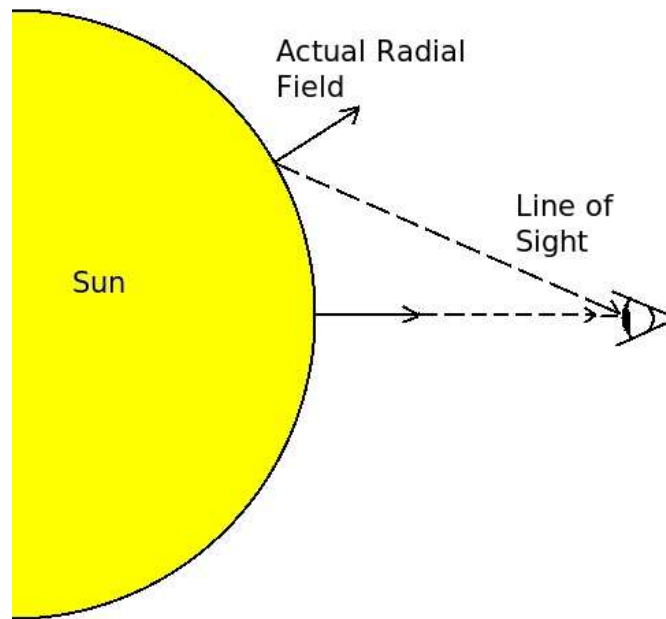


Figure 2.15: Image illustrating the inaccuracy of the Kitt Peak magnetogram measurements. The solid line represents the actual radial field component, the dashed line indicates the recorded line of sight component. The difference between the two measurements at higher latitudes is obvious.

latitudes (say around -40° to 40°) approximately matches the measurements obtained from Kitt Peak. Doing so will give confidence that our higher latitude and polar field evolution, which is systematically derived due to surface flows pushing the low latitude fields to higher latitudes, is correct. Thus our polar fields should be more accurate than those seen in Kitt Peak magnetograms. Hence, the overlying global dipole will be modelled accurately when a potential field is extrapolated using the radial surface map.

Below, an understanding of the Kitt Peak measurements and flux evolution within them is given.

Figure 2.16 was created by averaging the flux at each latitude from the Kitt Peak magnetograms over two solar cycles. We created this image in order to show the general orientation of magnetic flux throughout the two observed solar cycles and to give us a reference to the general behaviour of magnetic flux with time. The two cycles used were cycles 21 (June 1976-August 1986) and 22 (September 1986-April 1996). Doing so produced the well known butterfly diagram, similar to that for sunspot emergence. There are several key features within this diagram. It is clearly visible that the polar flux within each hemisphere is of opposite polarity. Initially, positive field is in the north pole, negative field is in the south pole. At just after solar maximum, the fields are observed to switch

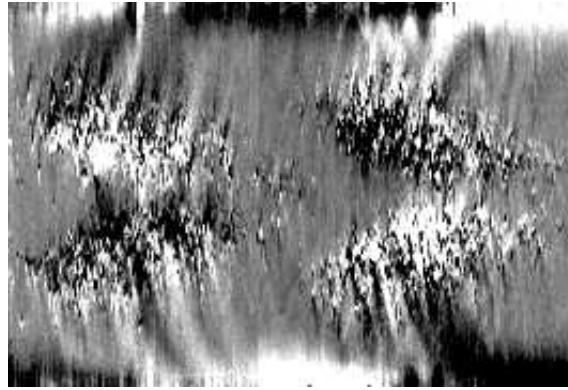


Figure 2.16: Image produced when we averaged the longitudinal magnetic field at each latitude within the Kitt Peak magnetograms for two solar cycles. The classic butterfly diagram, similar to that of bipole emergence is clearly visible.

sign. The polar field then remains this polarity until just after the maximum of the next solar cycle. At this point field reversal occurs again and the polar fields change sign. Another key feature is that the polarities in each hemisphere that are directed polewards and diffused equatorwards are of opposite sign. In the northern hemisphere, during the first cycle a fraction of the positive polarity of the lower latitude bipoles is being diffused equatorwards. In the southern hemisphere, the negative polarity of the lower latitude bipoles is being diffused towards the equator. During the second cycle, the polarities have reversed. This tells us about the orientation of the bipoles that are emerging on the sun. During the first cycle in the northern hemisphere, the leading polarity is positive while the trailing polarity is negative. During the next cycle this has reversed. The leading polarity is now negative while the trailing polarity is positive. In the southern hemisphere the bipole orientation was the opposite way around. This helps explain another noticeable feature of the butterfly diagram. In both hemispheres visible “streaks” of flux can be seen heading polewards. These streaks appear to be mainly of opposite polarity to the fluxes that are being directed towards the equator. This is because the streaks are comprised mainly of magnetic flux that is being transported towards the polar region by the meridional circulation. This flux is comprised mainly of the trailing polarities of the magnetic bipoles. These polarities are carried polewards by the meridional circulation, where they cancel with the existing polar field. This eventually causes the polar fields to reverse sign and build up strength in the declining phase of the cycle.

Figure 2.17 shows graphs of the signed magnetic flux from the Kitt Peak magnetograms at (a) 20° latitude, (b) -20° latitude, (c) 40° latitude and (d) -40° latitude. Using these images allows us to

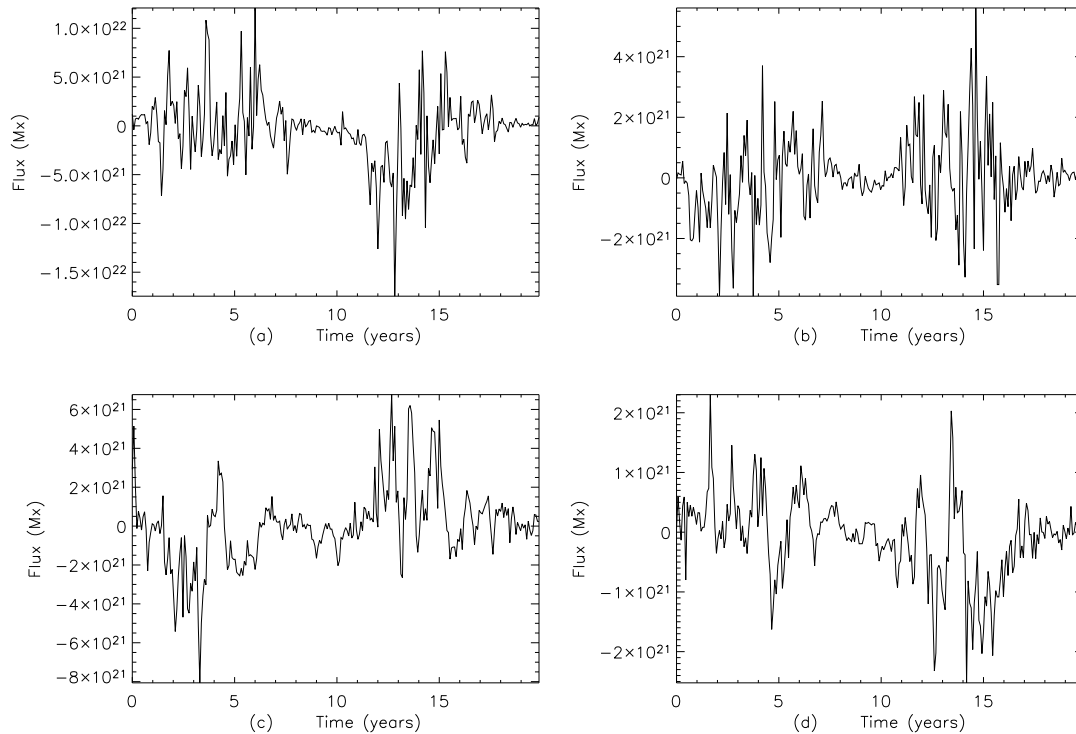


Figure 2.17: Graphs showing the total signed value of flux against time at (a) 20° latitude, (b) -20° , (c) 40° and (d) -40° . Comparing these flux values with the averaged butterfly diagram allows comparisons as to the behaviour of the two observed solar cycles to be drawn.

determine the dominant flux at each latitude, and hence the orientation of the magnetic bipoles within each cycle. Figure 2.17 (a) shows the signed magnetic flux at 20° latitude. During the first cycle the magnetic flux at this latitude is mainly positive, during the second cycle it is mainly negative. Comparing this with Figure 2.17 (b), which shows the signed magnetic flux at -20° latitude. During the first cycle, the majority of the magnetic flux at this latitude is negative, while during the second cycle it is mainly positive. This tells us about the tilt angle and orientation of the magnetic bipoles at these latitudes. Figure 2.17 (c) shows the signed magnetic flux at 40° . During cycle one, most of the magnetic flux at this latitude is negative, while during cycle two most of the magnetic flux is positive. Conversely, Figure 2.17 (d) shows the signed flux at -40° . At this latitude, during cycle one most of the flux is positive, while in cycle two, most of the magnetic flux at this latitude is negative. Comparing these graphs with Figure 2.16, it can be seen that these flux readings would be expected.

Figure 2.18 shows plots of the total absolute average magnetic flux from the Kitt Peak synoptic mag-

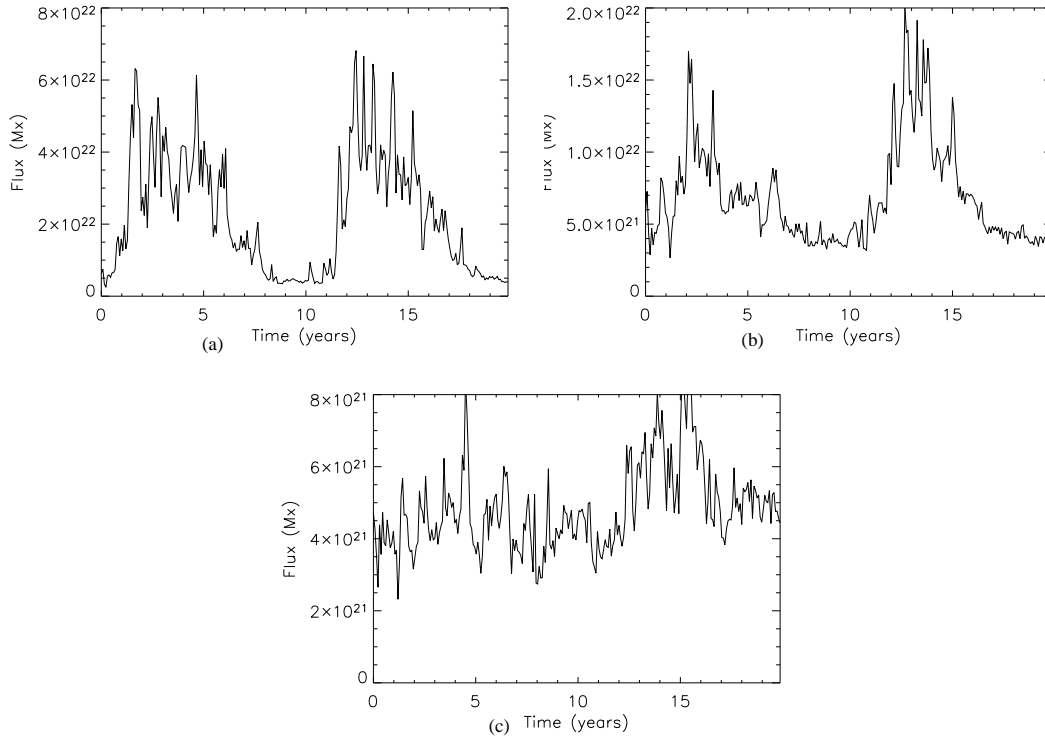


Figure 2.18: Graphs of the total absolute value of flux against time at (a) 20° , (b) 40° and (c) 55° latitude, taken from the Kitt Peak synoptic magnetograms. The magnetogram data represents cycles 21 (June 1976 - August 1986) and 22 (September 1986 - April 1996).

netograms at (a) 20° latitude, (b) 40° latitude and (c) 55° latitude. Similar graphs can be produced for (-20°) latitude, (-40°) latitude and (-55°) latitude. Figure 2.18(a) shows a plot of the absolute value of magnetic flux at 20° latitude from the Kitt Peak magnetograms, versus time. The value of flux here can be seen to rise slowly at the start of the cycle. This value then peaks at solar maximum and then shows a gradual decline through the declining phase of the cycle. The value of flux around solar minimum remains fairly constant, and is comparable between cycles. Figure 2.18(b) shows a plot of the magnetic flux at 40° latitude versus time. Here, the peak value of magnetic flux can be seen to occur very early in the solar cycle, during the early stage of the rising phase. The value of flux then gradually decreases throughout the rest of the solar cycle, through the maximum and declining phase. As the new cycle begins, the same flux patterns can be observed. Figure 2.18(c) shows a plot of the magnetic flux at 55° latitude versus time. There is only a very weak cyclic variation in flux level here. This is due to the inaccuracy of the Kitt Peak observations above $\pm 55^\circ$ latitude. The behaviour in Figures 2.18(a) and (b) can be explained by the pattern of flux emergence that is known to occur on

the sun. At the start of the solar cycle, magnetic bipoles emerge at higher latitudes on the sun. Their latitude of emergence then decreases and gets closer to the equator, while the number of emerging bipoles increases. Figures 2.18(a) and (b) show this emergence pattern. Figure 2.18(a) initially shows only a small amount of magnetic flux. As the cycle progresses through the rising phase, the latitude of emergence of the bipoles decreases. This is mirrored by the fact that the amount of flux at 20° latitude is seen to increase during the rising phase of the solar cycle. The flux is then seen to peak around solar maximum and decrease during the declining phase. Again, this follows the general emergence patterns of the magnetic flux. The amount of flux after solar maximum decreases during the declining phase as the number of emerging magnetic bipoles declines. At 40° latitude, the level of magnetic flux would peak early due to the higher emergence of magnetic bipoles during the rising phase of the cycle. This level then steadily decreases as both the latitude of emergence and amount of magnetic flux decreases through the various stages of the solar cycle.

2.4 Conclusions

In this chapter the radial surface flux transport simulation has been discussed. Equation 2.12 is derived and used as the base boundary condition within the main simulation. In order to understand the basics of flux evolution several simulations were run. Various aspects the magnetic bipoles were altered, including latitude of emergence and tilt angle. As the tilt angle of a bipole increases and becomes more positive with respect to the north-south line, more of the leading polarity can escape across the equator. This means that there will be more flux present within the simulation. If the tilt angle is larger but negative, the two polarities are pushed together before the meridional circulation takes effect and separates the polarities. This cancellation means that there is now less magnetic flux within the simulation. A simulation was then run where both meridional circulation and differential rotation were neglected in order to understand the effects of diffusion and using the spherical harmonics to create the magnetic field. It can be concluded that as the number of nodes in the harmonics increases the rate of diffusion increases. This is due to the number of zeros present, and hence locations of cancellation, increasing. Meridional circulation and differential rotation were re-introduced to the simulation, however, now the peak value of the meridional circulation was increased. This has the effect that, as the size of meridional circulation increases, polarities are pushed polewards at a faster

rate. The meridional flow then localises these polarities within the polar field, and a large amount of cancellation occurs. As more of both polarities are cancelling with each other, the end net flux value is lower for a higher peak value of meridional flow. These simulations were run in order to gain a basic understanding of the factors that can affect the evolution of the magnetic field and the amount of magnetic flux present within the simulation. It can be seen that the characteristics of the bipole, as well as that of the profiles of the various flows on the solar surface, can have a significant effect on the evolution of the surface field configuration, and hence the evolution of magnetic flux on the solar surface.

The Kitt Peak synoptic magnetograms were then investigated. The evolution of magnetic flux throughout the solar cycle was shown to follow the emergence rates of the magnetic bipoles. As the number of bipoles increases, the amount of magnetic flux increases. Flux at various latitudes was then calculated. This is a key part of the overall simulation as the radial flux transport simulation will be matched to the Kitt Peak magnetograms at low latitudes where the Kitt Peak measurements are accurate. The higher latitude fields will then be self-consistently produced by the flow profiles. This technique is used due to the inaccuracy of the flux measurements within the Kitt Peak magnetograms at higher latitudes. Figure 2.15 gives an explanation as to the inaccuracy of these measurements. This matching is done as the evolution of the higher latitude fields are key to this investigation. The connection to the overlying global dipole is a key element investigated here. Given that the global dipole originates from the polar field region, the correct modelling and evolution of these higher latitude field are key.

3

3D Coronal Field and Null Points

In the previous chapter we have discussed the magnetic flux transport model that will be used to model the time evolution of the radial magnetic field at the level of the photosphere. This field component will act as a lower boundary condition for the construction of a coronal magnetic field.

In this chapter the equation and constraints of the overlying coronal field will be discussed. The equations for deriving all three components of the magnetic field at all heights within the corona will be given. These equations will be shown to be derived by solving the solenoidal constraint $\nabla \cdot \mathbf{B} = 0$, with various boundary conditions applied. Two test cases will then be discussed. Each of these test cases will be set up such that the existence of at least one coronal null point is guaranteed. This will be done via a combination of a magnetic bipole and an overlying polar coronal field in the first case, and solely two magnetic bipoles in the second. In both of these examples, the null point finding technique of Haynes and Parnell (2007) will be applied in order to locate the coronal null point that should exist. The height of the calculated null point will then be compared to the calculated height of the field line orientation change. These should provide a good match each other. The variation of the height of the coronal null point as the strength of the bipole(s) and the degree of separation between polarities is altered will then be discussed.

Finally, a trilinear method for locating null points (Haynes & Parnell, 2007) will be discussed. The implementation of this method within the simulation will be used in Chapter 4 to consider the location and variation of coronal null points over 2 solar cycles.

3.1 Potential Field Extrapolation Technique

Within the solar corona the dominant force is the Lorentz force and any magnetic field that is in equilibrium satisfies to the zeroth order the force free equation, $\mathbf{j} \times \mathbf{B} = 0$. As a result the electric current $\mathbf{j} = \frac{1}{\mu_0} \nabla \times \mathbf{B}$ can be written in the form $\mathbf{j} = \alpha(\mathbf{r})\mathbf{B}$, where various solutions are dependent on the chosen form of $\alpha(\mathbf{r})$. The two most useful of these are when $\alpha = 0$, giving a potential field and $\alpha = \alpha(\mathbf{r})$, giving a non linear force field. When α is non-zero, the field may be regarded as sheared. Observations of the solar corona in H α and X-rays show localised, highly sheared regions called solar filaments and sigmoids, along with less or very weakly sheared regions such as coronal loops. However, white light observations show that the large scale field may be approximated by a field which is close to potential. In recent years much work has been done in constructing global MHD models from potential field extrapolations of a single surface map (Riley et al., 2006) or non-linear force-free field evolutions over period of months based on observed magnetograms (Yeates et al., 2007, 2008; Yeates & Mackay, 2009). In the study of Riley et al. (2006) the authors found that global potential field solutions closely matched those found from MHD simulations when potential field extrapolations of single surface maps are carried out.

The three components of the magnetic field are subject to the condition that magnetic flux must be in balance in order that no magnetic monopoles are discovered. Basically, this means that magnetic flux through a closed surface must be in balance. This means that the solenoidal constraint $\nabla \cdot \mathbf{B} = 0$ must be satisfied. However, for a potential field it is known that $\nabla \times \mathbf{B} = 0$, which is solved by setting $\mathbf{B} = -\nabla \Psi$. Combining these equations gives Laplace's equation,

$$\nabla^2 \Psi = 0. \tag{3.1}$$

The solutions to Laplace's equation are well known (Jackson, 1962), and in spherical coordinates may be expressed as:

$$\Psi(r, \theta, \phi) = \sum_{l=0}^n \sum_{m=-l}^l [a_{lm} r^l + b_{lm} r^{-(l+1)}] Q_l^m(\theta) e^{im\phi}, \tag{3.2}$$

where $Q_l^m(\theta)$ represent the associated legendre polynomials of degree l and n is taken to be the number of nodes within the simulation. The angular components of this equation can be written as $Y_{lm}(\theta, \phi) = Q_l^m(\theta)e^{im\phi}$, which represent the spherical harmonics, which were discussed in Chapter 2. Using the condition that $B_r = -\frac{\partial\Psi}{\partial r}$ it can be deduced that,

$$B_r(r, \theta, \phi, t) = \sum_{l=0}^n \sum_{m=-l}^l B_{lm}(r, t) Y_{lm}(\theta, \phi), \quad (3.3)$$

where $B_{lm}(r, t) = [(l+1)b_{lm}r^{-(l+2)} - la_{lm}r^{(l-1)}]$ represents the mode amplitudes, l indicates the harmonic degree and m indicates the azimuthal mode number. The coefficients a_{lm} and b_{lm} are constants which arise from solving Laplace's equation given a boundary condition. Taking the ratio of the magnetic field at any height, r , to the field at the solar surface, $r = R_\odot$, a new term for the mode amplitudes at all heights within the corona is determined. This ratio will describe how the mode amplitudes fall off with height in the corona. This gives,

$$\frac{B_r(r, \theta, \phi, t)}{B_r(R_\odot, \theta, \phi, t)} = \frac{(l+1)b_{lm}r^{-(l+2)} - la_{lm}r^{(l-1)}}{(l+1)b_{lm}R_\odot^{-(l+2)} - la_{lm}R_\odot^{(l-1)}}. \quad (3.4)$$

Using this means that the radial mode amplitude term can be rewritten as,

$$B_{lm}(r, t) = B_{lm}(R_\odot, t) \left[\frac{(l+1)b_{lm}r^{-(l+2)} - la_{lm}r^{l-1}}{(l+1)b_{lm}R_\odot^{-(l+2)} - la_{lm}R_\odot^{l-1}} \right]. \quad (3.5)$$

In order to eliminate either a_{lm} or b_{lm} , the condition at the upper boundary of $R_{ss} = 2.5R_\odot$ is used, namely that the magnetic field is purely radial (i.e. $B_\theta = B_\phi = 0$) at $2.5R_\odot$. To use this the angular components of $\mathbf{B} = -\nabla\Psi$ are calculated using Equation 3.2. This gives,

$$\begin{aligned} B_\theta &= -\frac{1}{r} \frac{\partial\Psi}{\partial\theta} = -\sum_{l=0}^n \sum_{m=-l}^l [a_{lm}r^{(l-1)} + b_{lm}r^{-(l+2)}] \frac{\partial Q_l^m(\theta)}{\partial\theta} e^{im\phi} \\ B_\phi &= -\frac{1}{r \sin\theta} \frac{\partial\Psi}{\partial\phi} = -\sum_{l=0}^n \sum_{m=-l}^l \frac{-im}{\sin\theta} [a_{lm}r^{(l-1)} + b_{lm}r^{-(l+2)}] Q_l^m(\theta) e^{im\phi}. \end{aligned} \quad (3.6)$$

Using these equations, the condition is satisfied by solving $a_{lm}R_{ss}^{(l-1)} + b_{lm}R_{ss}^{-(l+2)} = 0$. Solving this gives $a_{lm} = \frac{-b_{lm}}{R_{ss}^{(2l+1)}}$, which is then substituted back into Equation 3.5. Cancelling out the b_{lm} terms in this equation and then dividing through top and bottom by $R_{\odot}^{-(l+2)}$ gives the new term for calculating the radial mode amplitudes,

$$B_{lm}(r, t) = B_{lm}(R_{\odot}, t) \left[\frac{(l+1)\left(\frac{r}{R_{\odot}}\right)^{-(l+2)} + l\left(\frac{r}{R_{\odot}}\right)^{(l-1)}\left(\frac{R_{ss}}{R_{\odot}}\right)^{-(2l+1)}}{l+1 + l\left(\frac{R_{\odot}}{R_{ss}}\right)^{2l+1}} \right]. \quad (3.7)$$

Through this we know B_r at any radii out to R_{ss} as long as we know B_r at $r = R_{\odot} = 1$. We now need to determine B_{θ} and B_{ϕ} . To do this we need to determine the scalar function Ψ . This may be found by using the solenoidal constraint and the angular component of $\mathbf{B} = -\nabla\Psi$. This yields,

$$\frac{1}{\sin\theta} \frac{\partial}{\partial\theta} \left(\sin\theta \frac{\partial\Psi}{\partial\theta} \right) + \frac{1}{\sin^2\theta} \frac{\partial^2\Psi}{\partial\phi^2} = \frac{\partial}{\partial r} (r^2 B_r). \quad (3.8)$$

The right hand side of this equation is calculated by substituting in the earlier expression for B_r (Equation 3.3). The only radial dependence in the equation for the magnetic field comes from the $B_{lm}(r, t)$ term. This means that in order to calculate the right hand side of Equation 3.8, $\frac{\partial}{\partial r} (r^2 B_{lm}(r, t))$ must be calculated. This gives,

$$\frac{\partial}{\partial r} (r^2 B_{lm}(r, t)) = B_{lm}(R_{\odot}, t) l(l+1) \left[\frac{\frac{r^l}{R_{ss}^{l-1}} \left(\frac{R_{ss}}{R_{\odot}}\right)^{-(2l+1)} - \frac{r^{-(l+1)}}{R_{\odot}^{-(l+2)}}}{l+1 + l\left(\frac{R_{ss}}{R_{\odot}}\right)^{-(2l+1)}} \right]. \quad (3.9)$$

Using expression 3.9 in Equation 3.8 and the relation that $\nabla_{angular}^2 \Psi = l(l+1)\Psi = \frac{\partial}{\partial r} (r^2 B_r)$ we find the expression for $\Psi(r, \theta, \phi, t)$ becomes,

$$\Psi(r, \theta, \phi, t) = B_{lm}(R_{\odot}, t) \left[\frac{\frac{r^l}{R_{ss}^{l-1}} \left(\frac{R_{ss}}{R_{\odot}}\right)^{-(2l+1)} - \frac{r^{-(l+1)}}{R_{\odot}^{-(l+2)}}}{l+1 + l\left(\frac{R_{ss}}{R_{\odot}}\right)^{-(2l+1)}} \right] Y_{lm}(\theta, \phi). \quad (3.10)$$

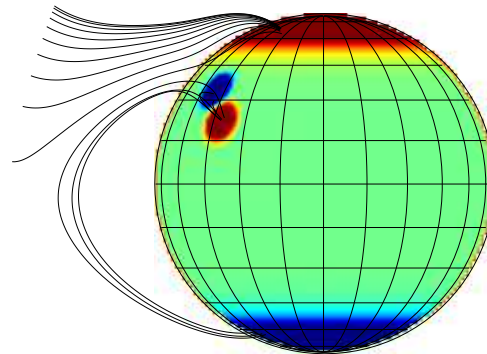
This is used to give the equations for the angular terms of the magnetic field. This means that all three components of our magnetic field are represented at all radial heights in the corona by the equations:

$$\begin{aligned}
B_r &= \sum_l \sum_{m=-l}^l B_{lm}(r, t) Y_{lm}(\theta, \phi) \\
B_\theta &= \sum_l \sum_{m=-l}^l C_{lm}(r, t) \frac{\partial Q_l(\theta)^m}{\partial \theta} e^{im\phi} \\
B_\phi &= \sum_l \sum_{m=-l}^l \frac{im}{\sin \theta} C_{lm}(r, t) Y_{lm}(\theta, \phi), \tag{3.11}
\end{aligned}$$

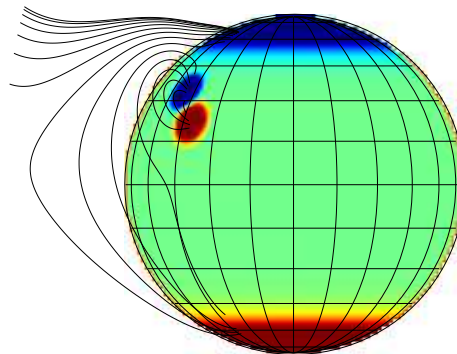
where $B_{lm}(r, t) = B_{lm}(R_\odot, t) \left[\frac{(l+1)(\frac{r}{R_\odot})^{-(l+2)} + l(\frac{r}{R_\odot})^{(l-1)}(\frac{R_{ss}}{R_\odot})^{-(2l+1)}}{l+1+l(\frac{R_\odot}{R_{ss}})^{2l+1}} \right]$ are the radial mode amplitudes, $C_{l,m}(R_\odot) = B_{lm}(R_\odot, t) \left[\frac{(\frac{r}{R_\odot})^{-(l+2)} - (\frac{R_{ss}}{R_\odot})^{-(2l+1)}(\frac{r}{R_\odot})^{l-1}}{l+1+l(\frac{R_\odot}{R_{ss}})^{2l+1}} \right]$ are the angular mode amplitudes, $Y_{lm}(\theta, \phi) = Q_l^m(\theta) e^{im\phi}$ are the spherical harmonic components and Q_l^m are the associated Legendre Polynomials. Therefore, once $B_{lm}(R_\odot, t)$ are known, a unique potential field may be determined.

3.2 Test Cases

Two test cases are now discussed. In each of these examples surface flux configurations are set up such that a coronal null point is known to exist. The first of these consider inserting one bipolar active region in addition to a polar field existing in the north and south pole. The second example requires the insertion of two bipoles such that a null point may form in the coronal region between them. Field lines are then plotted around the line of symmetry of the bipoles. The direction of these field lines are then calculated and used as a indication of the height at which the magnetic field changes direction. This will give an indication as to the height of the null point that should be lying in this region. This technique works relatively well for indicating the height of the null point when the system has a high degree of symmetry. In section 3.3, an alternative method will be described which is more robust and will be applied to non-symmetric situations. This method will also be applied to the symmetric situations and compared with the results of the field line orientation test. Through these comparisons, we can be confident that the null point finding technique is implemented correctly. This provides a good basis for understanding the behaviour of the coronal field and the impact that various surface effects will have on the presence of a coronal null point.



(a)



(b)

Figure 3.1: Images showing a sample configuration from the simulation (a) before global dipole reversal and (b) after global dipole reversal. Between these images the polar field has reversed polarity, meaning that the overlying global dipole is the same orientation to the underlying bipole. In this image red indicates positive flux, blue indicates negative flux.

Figure 3.1 shows a sample field configuration similar to the first of the two test cases that will be investigated. Both images in Figure 3.1 show a magnetic bipole inserted with a small positive tilt

angle in the northern hemisphere. A polar field is then prescribed, which will provide the overlying global dipole. In Figure 3.1(a), the overlying global dipole is of opposite orientation to the underlying active latitude flux as would occur in the rising phase of the cycle. This will produce a coronal null point above the central region of magnetic flux produced by the magnetic bipole. Figure 3.1(b) shows the magnetic field extrapolated after global dipole reversal, as would occur in the declining phase of the cycle. In this case the overlying magnetic flux is of the same orientation to the underlying magnetic flux. In this case, no coronal null point is produced, however, two photospheric null points exist. These null points are located on the photosphere between the each polarity of the bipole and its respective polar field region. These field configurations represent typical, albeit simplified, possible field configurations from throughout the solar cycle. Figure 3.1(a) could be a field configuration from during the rising phase, prior to polar field reversal, while Figure 3.1(b) could represent the field after polar field reversal. Given the change in overlying global dipole field orientation between the images, we can determine that the orientation of the overlying global dipole could be opposite to that of the underlying magnetic flux during the rising phase of the solar cycle, but of the same orientation during the declining phase. Whilst this setup can be viewed as fairly simplified, it can still raise the question as to the dependence of the null points upon the global dipole. If the null points are found to be exclusively connected to the global dipole, this albeit simplified setup implies that there is the possibility that no nulls would occur in the declining phase of the solar cycle. This could mean that the breakout model would only be applicable during the rising phase of the solar cycle as a possible method for explaining CME occurrence. This will be further investigated in Chapter 4.

3.2.1 Single Bipole, Overlying Global Dipole

The first test simulation involves inserting a bipolar active region, with a 90° tilt angle about the equator. The setup is illustrated in Figure 3.2 where both the bipole and the polar field may be seen. In this plot red is positive flux and blue is negative flux. This setup mimics that of Antiochos (1998), where the polar field in each hemisphere is of opposite polarity to the emerged polarity from the bipole within that region. The peak strength of this bipole is then varied from 1 gauss to 150 gauss. This gives our bipole flux ranging from approximately 6×10^{20} to 2×10^{22} Maxwells, where the absolute value of the polar flux in each hemisphere is 9.8×10^{22} Mx. Using the coronal field

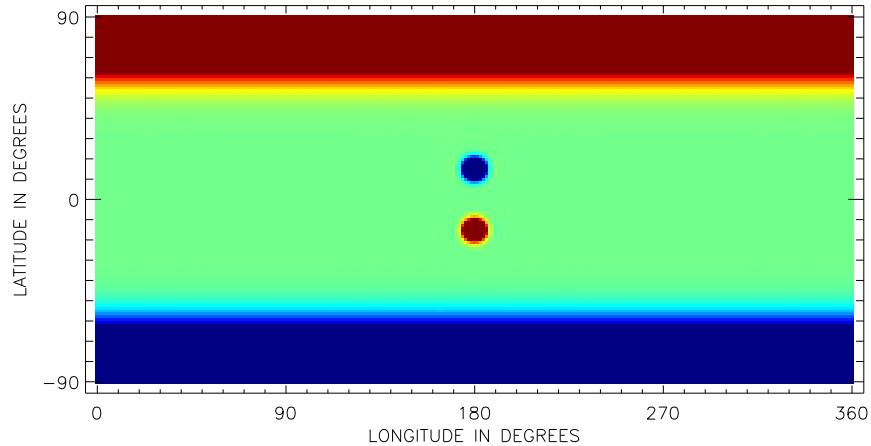


Figure 3.2: Image showing the radial field surface distribution of the first test simulation. A magnetic bipole has been inserted with a 90° tilt angle about the equator. This gives the bipole polarities the opposite orientation to the prescribed polar field in each hemisphere.

extrapolated from this the height of the change in orientation of the magnetic field above the central region of flux between the bipole polarities is calculated. This change in orientation indicates the change in direction of the magnetic field and the location of the coronal null point located between the two regions of oppositely orientated flux. This technique is then repeated for bipoles with a larger separation between the polarities. The polar field in each hemisphere is of opposite polarity to the emerged polarity from the bipole within that region. Figure 3.3 shows an orthographic plot of the radial surface field with overlying coronal field lines. The coronal field set up of this model is very similar to the initial configuration of the breakout model of Antiochos (1998). The overlying dipolar field is of opposite orientation to the underlying field from the bipole, and the approximate height of this will now be calculated to give an estimate to the height of the null point which will form between these two regions.

Figure 3.4(a) shows a plot of the height of the change in orientation of the magnetic field lines, which illustrates the approximate radial location of the null points. When the height is 1 this means that the 2 polarities of the bipole are not connected and no coronal null point exists. Each change in magnetic field direction is calculated at $\phi = 180^\circ$ and $\theta = 90^\circ$. Each colour within the plot represents a different degree of separation between the two polarities of the bipole. Black indicates 5° half separation between the polarities, purple 10° half separation, blue 15° , green 20° and orange 25° half separation.

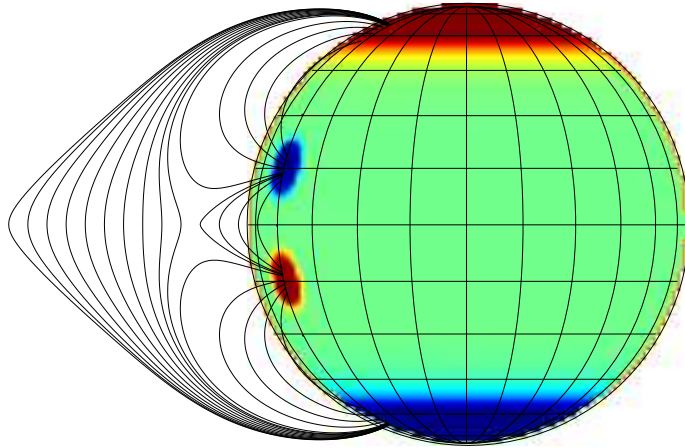


Figure 3.3: An orthographic image of the set up of the first test simulation. The radial surface field consists of a magnetic bipole inserted with a 90° tilt angle such that its orientation of polarities is opposite to that of the polar field within each hemisphere. The potential coronal field extrapolated from this gives a field configuration similar to that of the initial set up of the breakout model (Antiochos, 1998). The plot is made for a flux ratio of bipole to arcade flux of 0.10. Here we define arcade flux as magnetic flux between the two polar field regions, while bipole flux goes between the two polarities of the magnetic bipole.

This figure shows that the separation between the bipoles along with the ratio of bipole/polar flux has a direct effect on (1) when in the simulation the field lines from the bipole polarities can connect between each other and (2) that the height of the reversal of direction of the magnetic field between the field from the bipole and the field from the overlying global dipole increases as the flux ratio increases. If the separation between the polarities is sufficiently small, the magnetic field connects between them for low flux values. As this separation increases, the amount of flux required for the two bipoles to connect increases also. This is due to both the distance that the magnetic field must travel between the polarities increasing and the strength of the polar field restricting the underlying

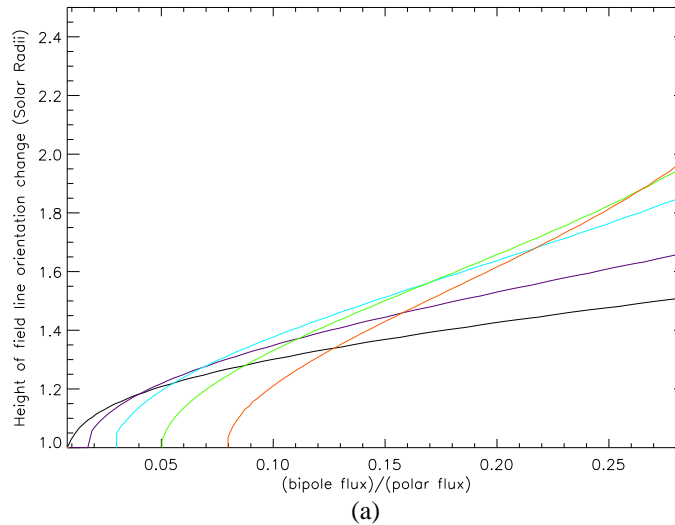


Figure 3.4: Graph showing the height of the change in field orientation giving the approximate location of the null point in the first test simulation. Each line represents a different degree of half separation (namely the number of degrees between one polarity and the equator): the black line indicates 5° half separation, purple indicates 10° half separation, blue shows 15° , green indicates 20° and orange represents 25° half separation.

central region of flux from reaching out into the corona and between the polarities.

3.2.2 Two Bipolar Active Regions

In the second test simulation, two bipolar active regions are inserted along the equator with no overlying polar field. These regions were emerged such that the polarities allow a similar coronal field set up to that of the breakout model, but now with all of the magnetic flux originated within the active regions. Figure 3.5 shows an image of the radial surface field showing the initial set up of the simulation, where two bipolar active regions emerge along the equator. The orientation of the polarities is such that the orientation of the bipoles is the same in each case. Figure 3.6 shows an orthographic plot, viewed from the south pole region, showing field lines plotted throughout the corona. This shows that the coronal field topology is similar to that of the breakout model.

Two different tests are then carried out in order to calculate the height at which the orientation of the field lines change over the central region of the flux (taken at $\theta = 90^\circ$, $\phi = 180^\circ$) and at which radial height the location of the coronal null occurred. The first simulation involves holding the size of the inner polarities constant and increasing the size of the outer polarity from a peak strength of 1 Gauss

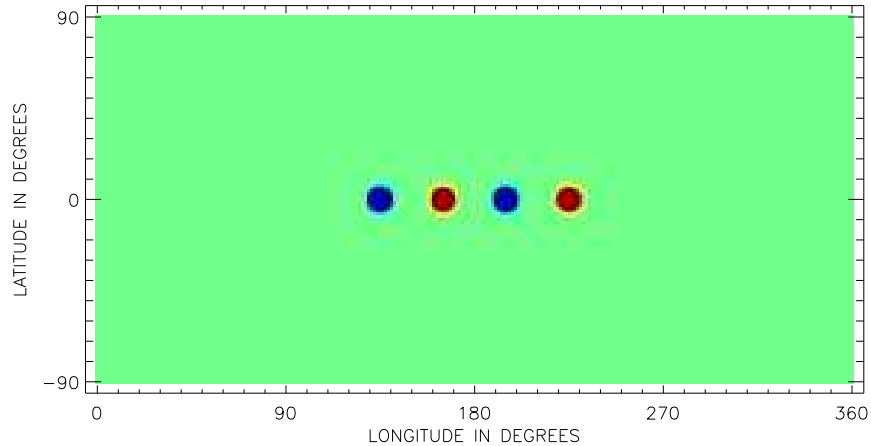


Figure 3.5: Image showing the radial surface field distribution in the second test simulation. Two magnetic bipoles have been inserted along the equator with zero tilt angle. This is a setup similar to the surface configuration of the breakout model as it is also a quadrupolar field configuration. In the image red indicates positive flux and blue indicates negative flux.

up to 200 Gauss. The second simulation involves holding the strength of the outer polarities constant and varying the peak strength of the inner polarities from 1 to 200 Gauss. Figure 3.7 shows a plot of the height of the field reversal within the simulation, demonstrating the location of the null points. The dotted line indicates the height change when the strength of the outer polarities is held constant, the solid line indicates the height change when the inner polarities strength is held constant. In these simulations, the non changing bipole is held constant at a strength of approximately 20 Gauss. Clearly both simulations produce different, but expected, behaviour within the magnetic field. When the size of the outer bipole is held constant and the inner bipole is very weak, the overlying field from the outer bipole restricts the field from the inner bipole from reaching out into the solar corona. This means that the height of the change in orientation of the magnetic field is low down. As the size of the inner bipole increases, the field lines reach higher into the solar corona. This means that the height at which the angle change occurs (and hence null point will form) is higher in the corona. Eventually, as the size of the inner bipole becomes much greater than the size of the outer bipole the magnetic field from the inner regions extend out through the corona and pass out beyond $2.5R_{\odot}$. This means that the field reversal between the two regions of flux is no longer picked up as the flux from the inner polarity reaches beyond the outer boundary of the model.

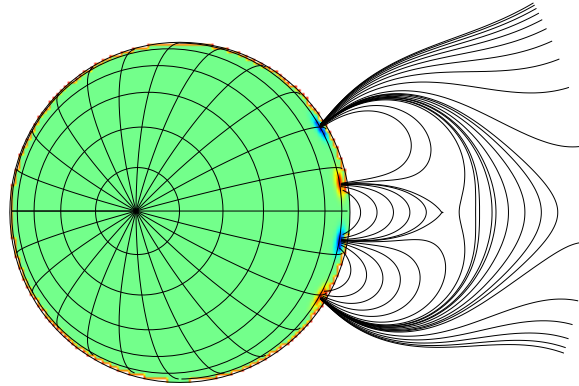


Figure 3.6: Image showing an orthographic plot and field lines of the set up of the second simulation. The extrapolated coronal field shows a configuration similar to the coronal field set up within the initial configuration of the breakout model.

Conversely, when the size of the inner bipole is held constant and the size of the outer bipole is varied we see the opposite effect. As the size of the outer bipole starts very weak, the field from the inner bipole dominates and reaches out beyond the outer boundary of the simulation. As the size of the outer bipole increases, the amount of magnetic flux from the inner bipole connecting to the outer bipole increases. This means that the height of the change in orientation between the two regions of flux decreases as the amount of flux from the outer magnetic bipole increases and compresses the flux from the inner bipole. This happens very rapidly as the outer bipole strength builds up.

This method provides a good starting point for looking for nulls within the field configurations. these simple field configurations are done to provide a first estimate as to the location of the coronal null point. However, the method is very simplified and ideal for use on highly symmetric cases. In general, actual solar magnetic field configurations are much more complex, so this technique would not work.

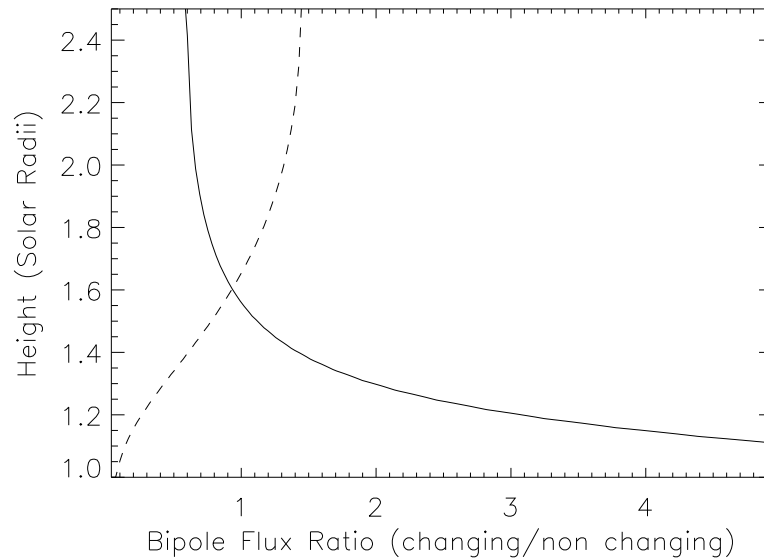


Figure 3.7: Plot showing the height in solar radii of the field line orientation change when (a) the inner bipole strength is held constant and the outer bipole strength is increased (solid line) and (b) the outer bipole strength is held constant and the inner bipole strength is increased (dashed line).

A much more rigorous technique will be needed for use throughout our main simulations.

3.3 Null Point Finding Technique

While the method of looking for reversals in the horizontal field component may find null points in highly symmetric cases a more general method is required for complex, non-symmetric situations. This technique is now described.

In order to scan a coronal field for the location of null points ($|\mathbf{B}| = 0$), the trilinear null finding method of Haynes & Parnell (2007) is used within the spherical geometry of the code. The method is split into three distinct parts; reduction, trilinear analysis and then locating the null point to sub grid resolution through a root finding technique. In the reduction stage every grid cell is scanned and a simple test is used to determine whether or not, a null point may exist. Each grid cell has longitude and latitude size of 1.40625 degrees (17,082.4 km), and a radial height ranging from 17,293.8km just above the solar corona up to 41,842.8km at the outer boundary. A necessary, but not sufficient condition for a null is that all three field components as defined on the corners of the cube must reverse

sign. This condition implies that the components go through at least one sign change within the cube.

The second stage of the method is a trilinear analysis of each cell that is remaining. This is based on the fact that if a null point exists then it must lie on all three of the zero curves, $B_r = B_\theta = 0$, $B_\theta = B_\phi = 0$ and $B_\phi = B_r = 0$. Within the grid cells, these curves can have one of two forms: (1) a circuit within the cell or (2) a curve that extends through the boundary of the grid cell at either end. The trilinear method was developed in order to detect nulls which would occur in the second configuration. This is because nulls with the form of (1) would imply that the grid cell contains 2 null points and means that a finer sub grid structure would have to be used in order to detect them. As we are looking at large scale magnetic structures within our simulation, the trilinear method is sufficient for the null points that we will be looking to detect. The existence of these curves is first considered on the faces of each cell, where the lines $B_r = 0$, $B_\theta = 0$ and $B_\phi = 0$ are considered. To consider this, each field component is expressed in terms of a bilinear equation,

$$B_i = a_i + b_i x + c_i y + d_i xy, \quad (3.12)$$

where i indicates the component of the magnetic field considered and x and y represent the spherical coordinates, within the plane of the cell face. For simplicity, it is assumed that the range of each x and y value is normalised such that $0 \leq x, y \leq 1$. The constants are determined from the values of the field on the cell corners such that $a_i = B_{i(0,0)}$, $b_i = B_{i(1,0)} - B_{i(0,0)}$, $c_i = B_{i(0,1)} - B_{i(0,0)}$ and $d_i = B_{i(1,1)} - B_{i(1,0)} - B_{i(0,1)} - B_{i(0,0)}$ (where $B_{i(0,0)} = B_i(0, 0)$). To solve for any single intersection, pairs of equations $B_i = B_j = 0$ are considered and the values of x and y which satisfy this and lie between $0 \leq x, y \leq 1$ are found.

These points represent the location where zero curves threading through the interior of the cell cross the boundary of the cell. A necessary condition for a single null to occur in the cell, is that each possible combination of these zero curves, must pierce the boundary of the cell in pairs, however, it is possible for one zero curve to cross the boundary at more than one pair of points. A null exists if and only if, along any given zero curve the third component of the field is of opposite sign at the end points which lie on the face. The sign of this component is determined using Equation 3.12.

Once the existence of a null has been confirmed, it is then located down to sub-grid resolution using

a 3D version of the Newton-Raphson method for finding roots of equations. The Newton-Raphson method is repeated until $|\mathbf{B}| \leq 1 \times 10^{-4}$. Various starting points are used until the iterative method is successful within the cell. Should the method fail, the grid is then split up into eight sub-grid cells, using trilinear interpolation, and the trilinear process is then repeated on these sub-cells.

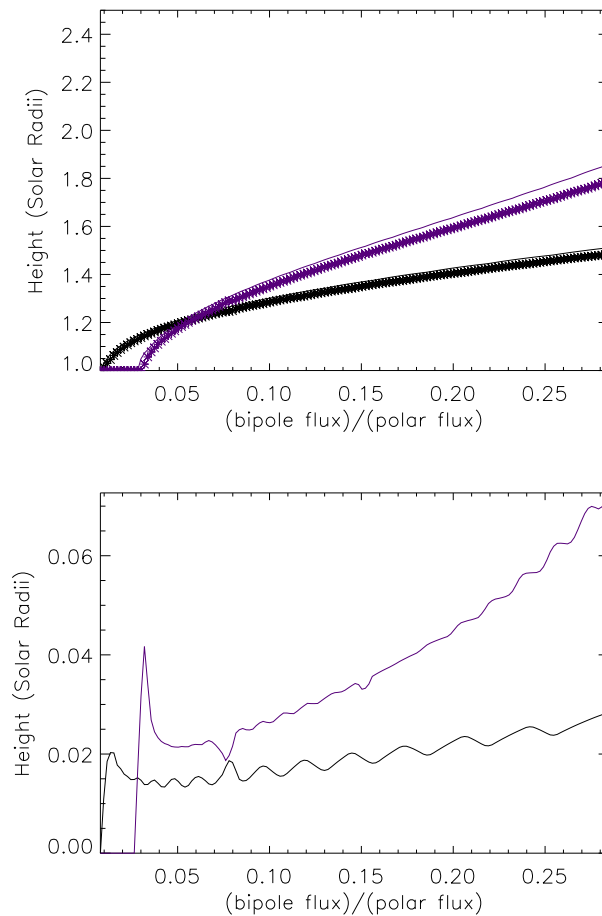


Figure 3.8: Plots showing (a) the calculated height of the coronal null point using the base boundary condition described in Figure 3.2 and (b) the difference between the height in field orientation previously calculated and the height of the null point. In both images the black line shows when the bipole polarities are emerged with 15° half separation, while the orange line shows 5° half separation. In image (a), the stars indicate the height of the null point calculated using the null finding technique, while the solid line indicates the height of the field line orientation change.

Figure 3.8 shows an example of applying the null finding code to the setup of Figure 3.2 for 5° half separation and 15° half separation. In this example a bipole is inserted with a 90° tilt angle about the equator, with a polar field in each hemisphere (the absolute value of the polar flux in each hemisphere is $9.8 \times 10^{22} \text{Mx}$). This setup mimics that of Antiochos (1998), where the polar field in each

hemisphere is of opposite polarity to the emerged polarity from the bipole within that region. The peak strength of the bipole is then increased from 1 Gauss to 150 Gauss, giving bipole fluxes ranging from approximately 6×10^{20} to 2×10^{22} Maxwells. The null finding code is then applied to the extrapolated coronal field, the results of which can be compared to the field line orientation change. Figure 3.8(a) shows a plot of the radial height of the coronal null point located at approximately the same longitude and latitude as the calculated field line orientation change. There is a slight difference between them due to resolution in the main code, but this difference is very small. This figure shows that the height of the null point follows the expected behaviour calculated using the field line orientation change, in that as the bipole flux increases, the field lines reach out higher into the corona and cause the null point to form at higher radial heights. Figure 3.8(b) shows the difference in the calculated height of the coronal null point and the height of the field line orientation change and it can be seen that the average difference is very low (less than $0.075R_{\odot}$). However, it is still well within an acceptable range. It should be noted that, while only the height of the coronal null point close to the central region is used, several null points along the separatrix between the bipole flux and the overlying flux are discovered when applying the null finding code, which was to be expected. These null points occur due to the connections between the polar regions of magnetic flux and the flux between the two polarities of the magnetic bipole. All of the flux between the two polarities of the bipole creates a shell of flux in the central region of the configuration. Above this, the flux from the polar region is of opposite orientation over the whole shell of the bipoles, creating a line of null points between the two distinct regions of magnetic flux.

Figure 3.9 shows an example of applying the null finding code to the setup of Figure 3.5. In this example, two bipoles are emerged along the equator. Two situations are then considered. The first involves holding the strength of the inner bipole constant (at 30 Gauss), and varying the peak strength of the outer bipole from 1 Gauss, to 200 Gauss. The second involved the reverse, namely varying the strength of the inner bipole while holding the outer bipole strength constant. The null finding code was applied to each coronal field extrapolation, the results for the radial height of the null have been plotted on top of the earlier results for the change in field line orientation (Figure 3.9(a)). The red dimonds indicate when the outer bipole strength is varied, the blue stars indicate when the inner bipole is varied. It appears that both sets of simulations, using the robust null finding technique, match up well to the earlier results from the field line orientation test at all heights in the corona, and follow

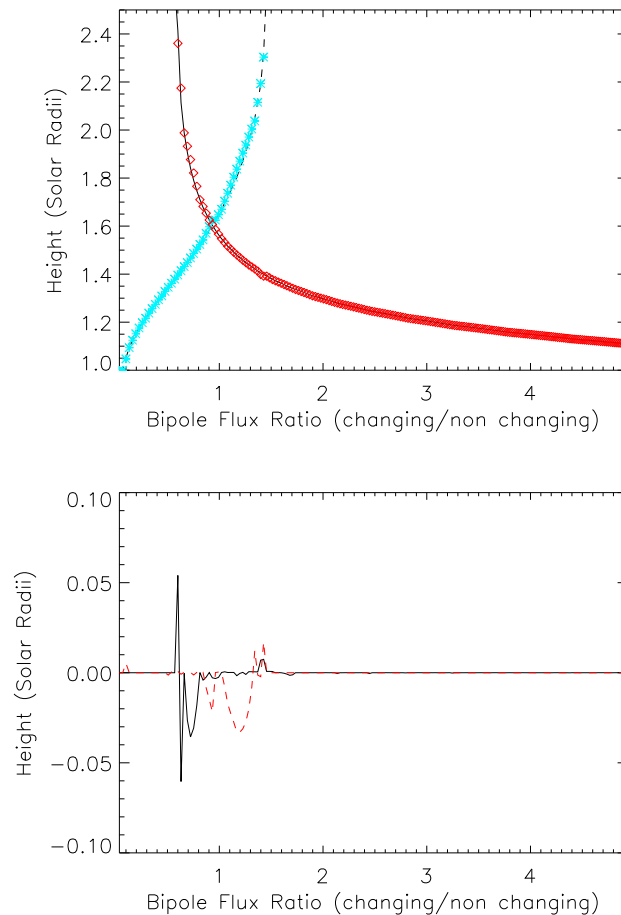


Figure 3.9: Plots showing (a) the calculated height of the coronal null point using the base boundary condition described in Figure 3.5 and (b) the difference between the height in field orientation previously calculated and the height of the null point. In image (a) the red diamonds represent when the inner bipole flux is held constant, the blue stars represent when the outer bipole flux is held constant. In image (b) the black line represents the difference when the inner bipole flux is held constant, while the red line indicates the difference when the outer bipole flux is held constant.

a similar variation as discussed earlier. While they match up well it should be noted that here we are only calculating the radial height of the null and not its θ or ϕ position. It is expected that if we also consider the values deduced for the θ or ϕ position, then a bigger difference is expected, with the null finding technique producing better results. Figure 3.9(b) shows a plot of the difference in calculated radial height between the field line orientation change and the calculated radial height of the null point using the null finding technique. It can be seen that there is only a very slight variation in the calculated radial heights of the null points compared with the field orientation change. At higher radial heights, the difference between the null point height and the height of the field orientation change is slightly

higher than at lower radial heights. This is because of the change in distance between grid points increasing with radial height. This gives a much larger distance between grid points for interpolating and calculating the null, which means a slightly higher error may occur. This simple test allows us to conclude that the null finding code has been implemented correctly. This means that the null finding code can now be applied to each extrapolated coronal field within our simulation in order to deduce the behaviour and variation of coronal null points throughout the solar cycle.

3.4 Conclusions

Within this Chapter, the potential field extrapolation technique has been discussed. Equation 3.11 is used to describe all three components of the magnetic field within the simulation, between R_{\odot} and $2.5R_{\odot}$. This led to the postulation of one of the main questions within this thesis: what is the variation of coronal null points in the large scale corona and what is their link to the overlying global dipole and surface magnetic field? In order to gain a basic initial understanding as to null point location and variation, two different example simulations, using different radial surface field configurations were discussed. These examples were used to illustrate an initial understanding as to the location of the null points, depending upon the underlying surface flux. The location of the coronal null point is compared with a simple test looking at the change in field line orientation within the coronal configuration. This allows the conclusion that the null finding code has been adapted into spherical coordinates correctly, at least for the simple configurations considered here. The height of field line orientation change, and hence null point location, is dependent upon both the overlying magnetic dipole configuration and the underlying configuration of surface flux. The interactions of polarities from multiple bipoles can cause a great variation in the complexity and configuration of the overlying coronal field. It can also be seen that the overlying global dipole acts as a restrictive force for magnetic bipoles with any given separation of polarities. This overlying global dipole field restricts the underlying magnetic flux from reaching out into the solar corona.

After using the height change of the magnetic field as an initial guess as to the height of coronal null points, the null point finding method was then described as the method that will be used in order to calculate the location of all of the coronal null points within the simulation. This method is required as it can find nulls in non-symmetric situations. This method provides the location of the coronal null

points to sub grid resolution in three steps. The first step applies a simple algorithm to eliminate any grid cells where a null point does not exist. The second step involves looking for sign changes in the location of the $B_r = B_\theta = 0$, $B_\theta = B_\phi = 0$ and $B_\phi = B_r = 0$ on the faces of each grid cell where a null point may possibly exist. Finally the Newton Raphson method is then employed in order to locate the coronal null point to sub grid resolution. In order to test that the code has been adapted properly it was applied to the coronal field extrapolated using the base boundary conditions described in 3.2.2. This simple setup was used in order to ensure that the null finding code was working correctly. These simple setups were used as they gave coronal configurations similar to the initial setup of the breakout model. This guaranteed not only a single null point at the top of the interior coronal arcade from the bipole in the central region of the setups, but also an arcade of null points created due to the 3D nature of the configuration. This provided a stiff test for the null finding code and gives us confidence that it is working correctly and can be applied to our main simulation.

In the next chapter we now run full solar cycle simulations over 2 solar cycles to investigate the occurrence of coronal null points.

4

Application of the Null Finding Code Over Two Solar Cycles

Having described the potential field extrapolation technique and the null point finding method, these can now be applied to the main simulation in order to investigate the variation of coronal null points over 2 simulated solar cycles. Two different simulations, classified by a different base boundary condition, will be run. The first simulation involves using the time evolution of the radial magnetic field at the solar surface, as given by Equation 2.3, as the base boundary condition. A potential coronal field is then extrapolated out to $2.5R_{\odot}$ from this. This simulation is run for 3 solar cycles, the first being used to remove the unrealistic condition of an axisymmetric polar field. Here we class polar field as being the magnetic field originating from above 70° in the northern hemisphere and below -70° in the southern hemisphere. This first cycle is discounted from the coronal null point analysis. The latter two cycles are then scanned for the existence of coronal null points, using the previously described null finding method. The second set of simulations use a different base boundary condition. Using the magnetic field distributions from the first run, a simple conversion algorithm is applied in order to turn them into simulated synoptic magnetograms. These are then used as the base boundary condition for construction of a potential field. This is done in order to give a base boundary condition that is comparable to the way in which Kitt Peak synoptic maps are created. The variation of coronal null points within both of these simulations will then be used to determine the connection between the null points and the emerging magnetic flux on the solar surface, and also their dependence upon

the overlying global dipole. A method of classifying the coronal null points using the radial surface field distribution which results in their creation is then discussed.

This chapter will be ordered as follows. Initially a brief reminder as to why the Kitt Peak synoptic magnetograms are not being directly used is given (Section 4.1). Then a description of both simulation techniques is given. The first simulation, called the instant day simulation, will be created, then matched with flux levels from the Kitt Peak magnetograms (Section 4.1.1). Using this simulation, the simulated synoptic magnetograms are then be created (Section 4.1.2). These will be shown to give a better match in terms of flux values to the Kitt Peak magnetograms, due to the similarities in their creation. The variation of coronal null points within both simulations will then be discussed (Section 4.2). Initially their variation throughout the solar cycle will be investigated (Section 4.2.1). In Section 4.2.2 the null point numbers in relation to the number of emerging bipoles will be discussed. Finally, in Section 4.2.3, the null points will be classified using the underlying surface field configurations which led to their creation.

4.1 Simulation Techniques

When creating the simulation, the question of whether or not to use the observed solar magnetograms from Kitt Peak as a base boundary condition for construction of a potential field arose. After careful consideration, these were not used due to the inaccuracy of the measurements above and below $\pm 60^\circ$ latitude. This inaccuracy arises due to the way in which the measurements are recorded. They are recorded as line of sight measurements of the radial field component of the magnetic field. This means that, closer to the equator, the measurements will be more accurate, whereas, at higher latitudes, the measurements will be less accurate. For our simulations it is necessary to accurately model the field in both low and high latitude regions, as in the high latitude regions is where the overlying global dipole field on the sun originates.

In order to accurately model this, a simulation was created by inserting bipolar active regions, created to follow the known patterns of bipole emergence during the solar cycle. The strength of these active regions was prescribed such that the flux in our simulation approximately matches the flux observed in the Kitt Peak solar magnetograms at various latitudes heading polewards. Matching the strength of

this lower latitude field between the instant day simulations and the Kitt Peak magnetograms allows the conclusion that the poleward transport of magnetic flux and subsequent strength of the polar fields has been accurately modelled. This is an issue of key importance when investigating the connection between the coronal null points and the overlying global dipole. Due to the overlying global dipole originating from within the polar field, it is important to accurately model the strength and evolution of this field at all times.

This evolution of the radial surface field, coupled with Equations 3.11 for modelling the overlying coronal field, giving the “Instant Day Simulation”. In this simulation, the radial magnetic field at the solar surface is evolved forward in time using Equation 2.12. Using this as a base boundary condition, the coronal field is extrapolated every 27 days. This information is then saved as an instant day map with extrapolated coronal field. Full details of this are given in Section 4.1.1.

Using the Instant Day Simulation data, a conversion algorithm is then applied converting the instant day maps into “Simulated Synoptic Magnetograms”. This allows a better comparison to the Kitt Peak synoptic magnetograms as the data is now more comparable to the observations it is being compared to. In doing this, a clearer picture of what data/information is lost through the conversion will be given. A comparison between the variation of coronal null points within each simulation type can also be considered.

4.1.1 Instant Day Simulation

Magnetic flux at the solar surface evolves through the processes of emergence, advection and surface diffusion. New flux emerges at the solar surface in the form of newly emerged bipolar regions (Archontis et al., 2004; Murray et al., 2006; Murray & Hood, 2007) . The flux is then evolved via large-scale flows such as differential rotation and meridional flow. The flux transport code used in this study includes these effects along with surface diffusion as a result of super-granular convection in order to evolve forward the radial component of the magnetic field at the solar surface (Wang et al., 1989; van Ballegooijen et al., 1998; Schrijver & Title, 2001; Baumann et al., 2006).

When creating the Instant Day Simulation, bipolar active regions are emerged throughout the solar cycle, and the magnetic flux is then evolved forward at the solar surface using the large scale flows of

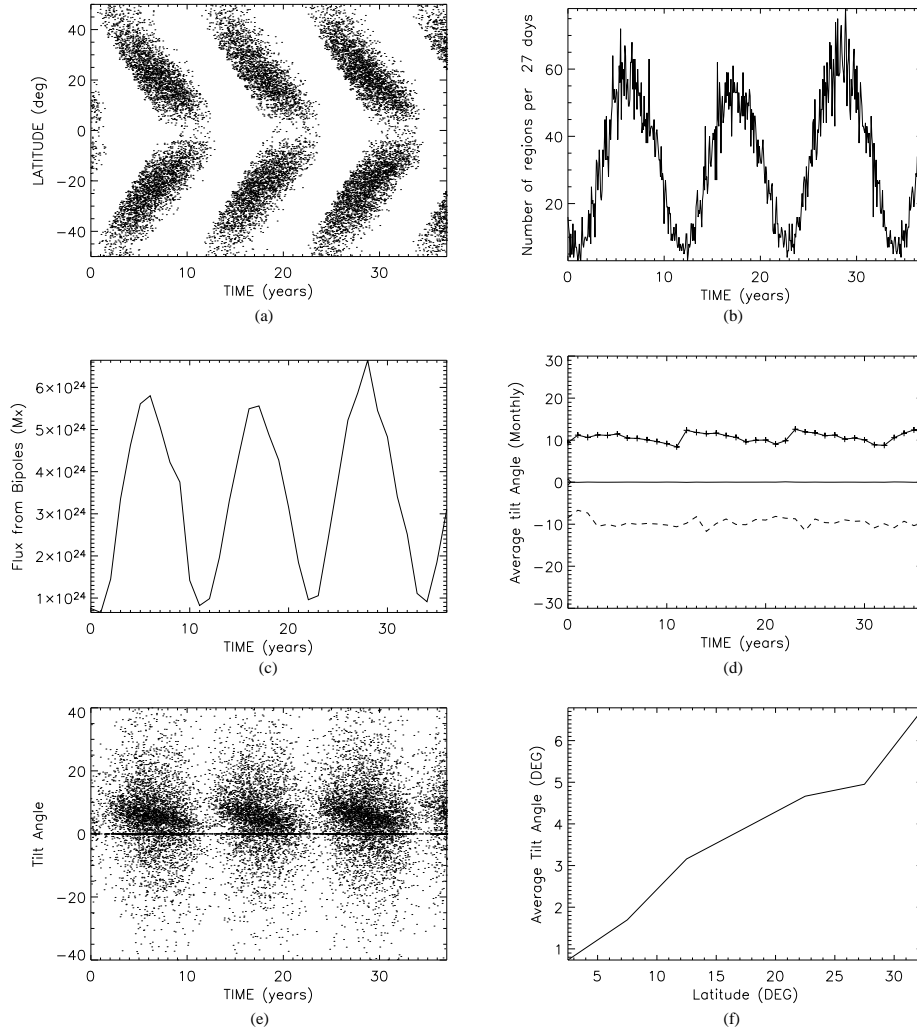


Figure 4.1: Graphs showing the properties of the bipoles emerged within the simulation. (a) The distribution of bipole emergences as a function of time and latitudes, (b) the numbers of bipoles emerging per 27 days, (c) the total flux within the emerging bipoles per year, (d) the average monthly tilt angle of the bipoles, (e) tilt angle distribution throughout the simulation and (f) the average tilt angle vs. latitude. The first cycle depicted in the plots above was used as a “control” cycle to initiate the simulation. The work presented here will only analyse cycles two and three where flux values have been scaled to KP synoptic data.

differential rotation and meridional circulation, coupled with diffusion. This simulation is approximately matched to the observed Kitt Peak magnetograms by matching flux values at various latitudes. This is done by changing various parameters of the magnetic bipoles that are emerged (i.e. tilt angle, latitude of emergence, size etc.), while using five sizes of bipole, ranging from 10^{19} Mx to 10^{22} Mx (Mackay et al., 2002; Mackay & Lockwood, 2002). Altering the tilt angle, latitude of emergence

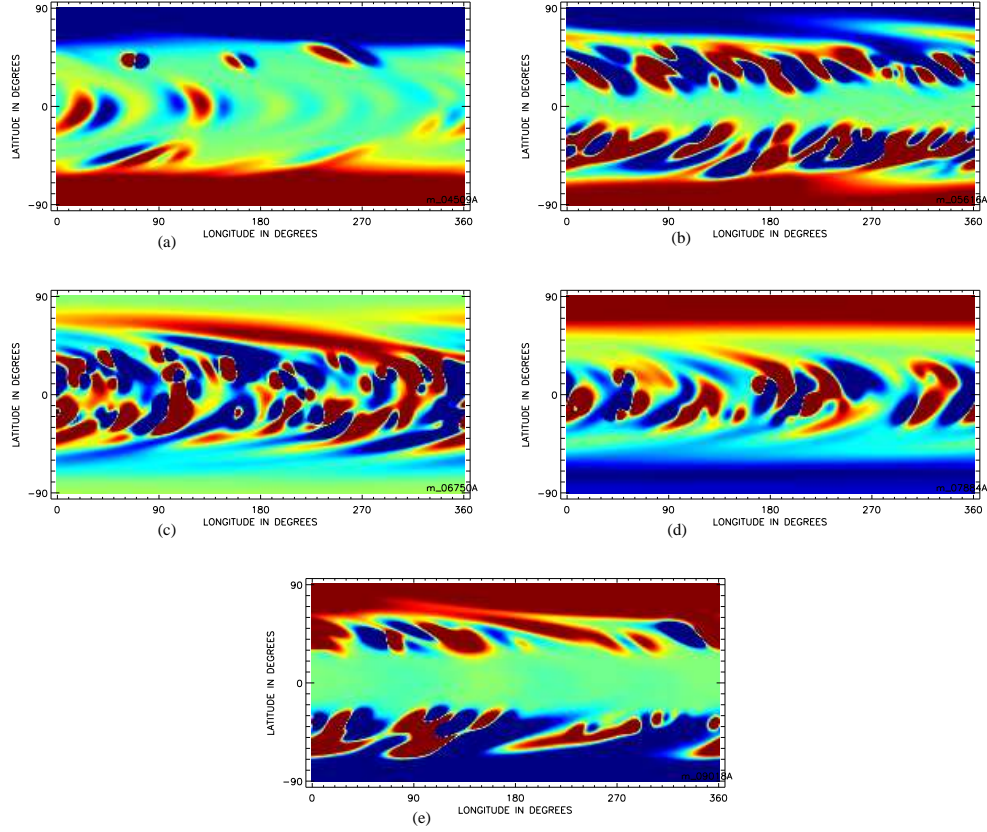


Figure 4.2: Sample radial surface maps taken from various stages of one of the solar cycles within the instant day simulation. Each map shows a different stage of the cycle. These are (a) solar minimum, (b) rising phase, (c) solar maximum, (d) declining phase and (e) solar minimum. Within the diagrams, red indicates positive magnetic flux and blue indicates negative magnetic flux, where the field strength saturates at 10G.

and other parameters of the bipoles allows us to alter the way in which the flows effect the bipole's evolution and thus the evolution of the magnetic flux on the solar surface and also allow us to ensure that the known characteristics of the solar cycle are upheld within our simulation, for example higher latitude of emergence early in the cycle, variation in bipole numbers throughout the cycle etc. The initial distribution of the radial field of the newly emerged bipoles is given by:

$$\Delta B_{r,init}(R_{\odot}, \theta, \phi) = B_{r,init}^{(+)}(R_{\odot}, \theta, \phi) - B_{r,init}^{(-)}(R_{\odot}, \theta, \phi), \quad (4.1)$$

where $B_{r,init}^{(\pm)}(R_{\odot}, \theta, \phi) = B_{max} \left(\frac{\beta_{init}}{\beta_0} \right)^2 \exp \left(\frac{-2[1 - \cos(\beta_{\pm}(\theta, \phi))]}{\beta_0^2} \right)$ are the distributions of the positive and negative polarity flux at the solar surface (van Ballegooijen et al., 1998). Here, β_{init} is the angular

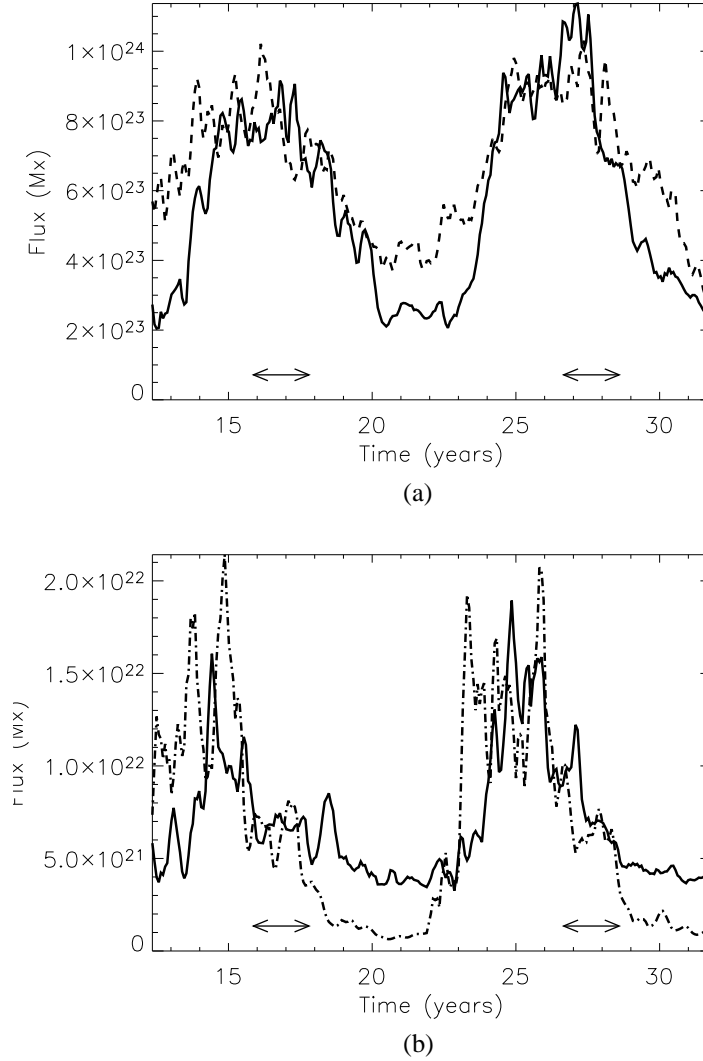


Figure 4.3: Graphs showing the surface flux from our “instant day” simulation. Graph (a) shows the total surface flux while (b) shows the flux at 40° latitude. In each case the solid lines denote the flux values deduced from the Kitt Peak synoptic magnetograms where the dashed curve denotes the results of the simulations. The double ended arrows in each graph denote a 2-year time period around cycle maximum determined from the peaks in bipole emergence rate.

width of each polarity component (assumed to be proportional to the angular separation between the two poles), β_0 is the angular width at which the poles of the bipole are inserted into the radial surface distribution (here $\beta_0 = 4^\circ$), B_{max} is the initial peak flux density (assumed to be 1100 Gauss for all bipoles) and $\beta_{\pm}(\theta, \phi)$ is the heliocentric angle between the latitude and longitude of emergence θ and ϕ and the center of the positive or negative polarity, (θ_+, ϕ_+) or (θ_-, ϕ_-) respectively. The term $\left(\frac{\beta_{init}}{\beta_0}\right)^2$ accounts for diffusion in the early phase of development, occurring as the magnetic flux tube

which causes the bipole rises through the convection zone and emergence at the solar photosphere. The emergence rates of the bipoles are matched to the known patterns that occur throughout the cycle, and is inversely proportional to the size of the region (Harvey & Zwaan (1993); Schrijver & Harvey (1994)). Figure 4.1 shows graphs which indicate the various properties of the magnetic bipoles that were used within our simulation. Graph (a) shows a plot of the latitude of emergence of the bipoles vs time. The distinctive butterfly diagram of bipoles is clearly visible, where bipoles emerge at a higher latitude at the beginning of the solar cycle, and emerge closer to the equator later on in the solar cycle. This plot also shows how we emerge approximately the same number of bipoles in both hemispheres of our simulation. Graph (b) shows a plot of the number of bipoles emerging every 27 days vs time. It can clearly be seen that, as the cycle progresses to solar maximum more bipoles emerge, which is the characteristic used to define this. As the cycle goes through the declining phase, the number of bipoles emerged gradually drops until solar minimum. Graph (c) shows a plot of the total flux from the emerging bipoles vs time, and this follows a similar pattern to graph (b). As more bipoles emerge in the rising phase, more flux will be available from them. As the numbers of bipoles begins to drop during the declining phase, the amount of flux that comes from the bipoles will also drop. Graph (d) shows the average monthly tilt angle of the bipoles, while graph (e) shows the distribution of tilt angles throughout the solar cycle. Graphs (d) and (e) show that at the start of the solar cycle, the average tilt angle of the bipoles can be seen to be larger than at the end of the cycle, with a fairly steady decline in tilt throughout the solar cycle as the bipoles begin to emerge at lower latitude. Graph (f) shows the average tilt angle vs latitude of emergence. As bipoles emerge at a higher latitude of emergence, they have a higher tilt angle. The graph seems to show the much shallower variation as suggested by Schüssler & Baumann (2006) of tilt angle of the emerging bipoles versus latitude of approximately $\frac{\lambda}{5}$. This is different from the previously calculated value of $\frac{\lambda}{2}$ found in Mackay et al. (2002) and Mackay & Lockwood (2002).

Figure 4.2 shows various radial surface maps taken from the instant day simulation. These maps cover all of the stages throughout a solar cycle. Figure 4.2(a) shows the distribution around solar minimum. At this stage, the numbers of magnetic bipoles emerging are very low, approximately one every day or two. The latitudes at which these bipoles emerge are also higher than later in the solar cycle, around $\pm 40^\circ$ latitude. At this point, the majority of the flux sits in the polar regions. As the cycle progresses through the rising phase (Figure 4.2(b)), the numbers of emerging bipoles increases. Their

latitude of emergence also gets closer to the equator. Throughout this stage, the emerged magnetic flux is being skewed in the longitudinal direction due to the differential rotation. Due to this the bipoles at this stage appear more tilted in the east-west direction. The meridional circulation has also taken affect and carried some of the magnetic flux polewards. This has the effect that the emerging bipoles are pushed into the polar region and begin to cancel with the polar flux as the trailing polarity, which is of opposite sign to the polar field reaches the poles first. Figure 4.2 (c) shows the field distribution just after solar maximum, which is determined as the stage around which the number of emerging bipoles peaks. At this stage, the polar fields have begun to reverse sign due to the meridional circulation carrying magnetic flux polewards. The latitude of emergence of the magnetic bipoles has also decreased to be around the equatorial region, while the numbers of emerging bipoles has peaked. As solar maximum is passed, the declining phase is entered. An example field configuration from this time is illustrated in Figure 4.2 (d). The numbers of emerging bipoles has decreased considerably. The strength of the polar field is increasing, but is now of opposite sign to that at the start of the cycle. This field configuration will continue until the end of the cycle, when the radial surface field will have a configuration similar to that of Figure 4.2 (e). At this stage, the sun is once again at solar minimum. The numbers of emerging bipoles is at its lowest amount. At this point, the total magnetic flux on the sun is at its minimum, while the polar field strength will peak around this time. The next solar cycle will follow the same characteristics as described above. These examples show that the simulation is following the known patterns of bipole emergence and evolution. The computed flux values that are present at the various stages of the solar cycle are now considered.

Using the combinations of properties of bipoles that have been calculated, combined with the bipole sizes, the flux values within the Instant Day Simulation are approximately matched to that of the Kitt Peak magnetograms over the whole surface, and at various latitudes. Figure 4.3 shows graphs of the flux within the Instant Day Simulation. Graph (a) shows the total surface flux, while graph (b) shows the flux at 40° latitude (a similar graph was produced for -40° latitude). In both graphs, the dashed line indicates the result from the Instant Day Simulation, while the solid line indicates the result from the Kitt Peak Synoptic magnetograms. A good match between the two sets of data can be observed in these images. The flux at the higher latitude of 40° matches fairly well in both sets of data. Using the fact that the flux matches fairly well in both sets of data at lower latitudes, we can conclude that we have modelled the transport of flux on the solar surface fairly accurately and that our values

for differential rotation, diffusion and meridional circulation are fairly accurate. This means that we should have a good approximation to the correct evolution and magnitude of the polar magnetic field, and hence, the overlying global dipole.

While the flux values are a very good approximation in this simulation, they are noticeably slightly higher, especially at solar minimum. This is because the Instant Day simulation evolves forward the radial field component daily and does not lose any information, as is the case for observations. When creating the Kitt Peak Synoptic magnetograms, the central meridian section of a full disk magnetogram is stored each day of a carrington rotation. This then forms a single Kitt Peak synoptic magnetogram. The main problem with this technique is that information on the solar surface may be lost. A bipole could emerge after the central meridian section and either be heavily diffused and weakened, or may not be picked up at all within an observation. Similarly, a bipole may emerge on the opposite side of the sun, which could be heavily weakened or even completely diffused by the time that it revolves around to central meridian. This forces us to ask the question as to whether creating Simulated Synoptic Magnetograms from our Instant Day simulations could give us a better approximation of flux over the surface and at various latitudes.

4.1.2 Simulated Synoptic Magnetograms

In order to convert the instant day maps into the form of simulated synoptic magnetograms, the relevant data from each of the instant day maps must be identified and extracted. To do this, initially a latitudinal strip with a width of 13.5° longitude is taken from the rightmost edge of the first instant day map. This portion of the instant day map is defined to be the portion that is initially lying at central meridian. This information is then stored as the rightmost strip of the first simulated synoptic magnetogram. A second latitudinal strip, of the same width, is then taken from the left edge of where the previous strip ended, but from the next instant day map, representing the fact that this would be the next strip to lie at central meridian. This is then stored as the next section of the simulated synoptic magnetogram. This method is then continued over 27 days of the instant day maps, making up a single simulated synoptic magnetogram covering one carrington rotation. This process is then repeated with each successive 27 instant day simulations, producing one subsequent simulated synoptic magnetogram per 27 days. Once constructed the simulated synoptic magnetograms are then

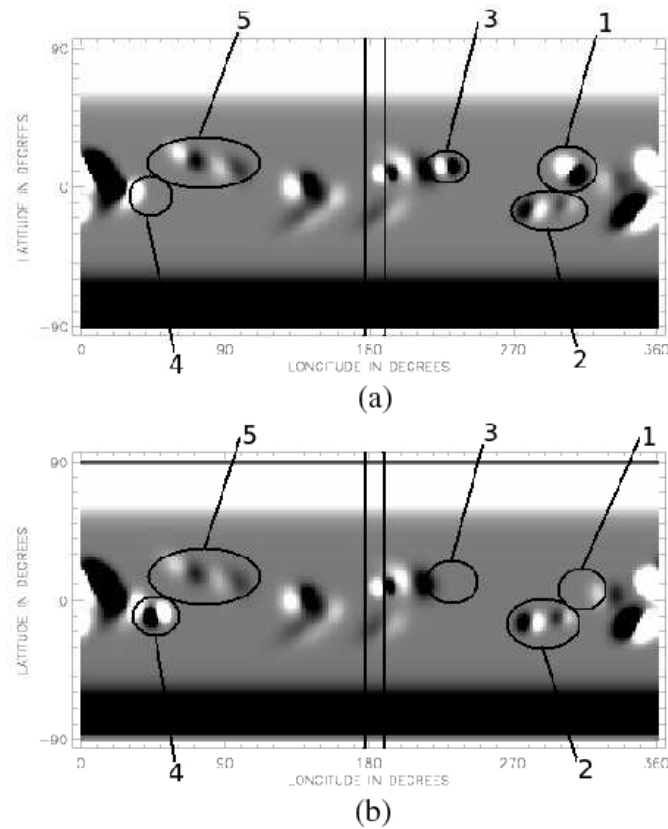


Figure 4.4: Image showing (a) a typical instant day map and (b) a simulated synoptic magnetogram. The 27 day period covered by the simulated synoptic magnetogram is the same 27 day rotation period the instant day example is taken from. The area within the vertical black lines corresponds to the portion of the instant day map that lies at central meridian and is extracted and inserted into the simulated synoptic magnetogram. Several key features have been marked on both the instant day map and the simulated synoptic magnetogram.

corrected for flux balance, which usually involves only a small correction. This involves merely totaling up the flux imbalance within the synoptic map and then adding flux of opposite sign to every pixel which has strength equal to the imbalance averaged out over the entire map in order that the surface field is now in balance. This is usually a very small correction.

Figure 4.4 shows a comparison between one of the simulated synoptic magnetograms (Figure 4.4(b)) and one of the instant day maps that was used to create it (Figure 4.4(a)). It can be seen that the method for creating simulated synoptic magnetograms produces a good average representation over a rotation. Comparing several of the features between the two images in Figure 4.4 gives a good understanding of what information and data are lost or missed when creating simulated synoptic

magnetograms. A key point to remember is that the black line in Figure 4.4(a) denotes the portion of the instant day map that lies at central meridian. This portion of the map is also highlighted in the simulated synoptic map. The information to the right of the black lined section in Figure 4.4(b) has already been extracted from the instant day maps, while the information to the left has yet to be extracted in relation to the shown instant day map.

Comparing feature 2 in both images shows that, in the instant day map the active regions appear slightly weaker, and more longitudinally sheared than in the simulated synoptic magnetogram. This is due to its extraction at an earlier time than the time of the current instant day map. Feature 5 shows bipolar regions, within the instant day map that have yet to be extracted for the simulated synoptic magnetogram. These bipolar regions appear less sheared and stronger in the instant day simulation than the corresponding regions in the simulated synoptic magnetogram. Therefore this shows the opposite effect to that of feature 2, where the large scale solar flows and diffusion have not had as much of an affect upon it, as they will have by the time the field information is extracted. Feature 4 shows a bipole that is yet to emerge in the instant day map, but is picked up for the simulated synoptic magnetogram. Conversely, features 1 and 3 show two bipolar regions that have been missed by the conversion into simulated synoptic magnetogram form. This is a key point, as information may be missed when converting into synoptic form thereby artificially impacting the complexity of the field distribution.

After converting the instant day maps into simulated synoptic magnetograms the same flux measurements are taken as before, shown in Figure 4.5. The simulated synoptic magnetograms show a better match than the instant day maps. The peaks of flux at solar maximum occur at approximately the same time and magnitude. The minima give a better match between the two data sets than before. This is because the simulated synoptic magnetograms lose some information compared to the instant day simulations (in the same way that the Kitt Peak magnetograms lose information). By comparing the simulated synoptic magnetograms to the Kitt Peak Synoptic magnetogram, data produced by a similar technique are compared. From this we have confirmation that our low latitude field distributions are realistic, at least in terms of absolute flux values, and subsequently will produce consistent high latitude fields.

Figure 4.6 shows plots which allow us to confidently see that the flux values within the simulated

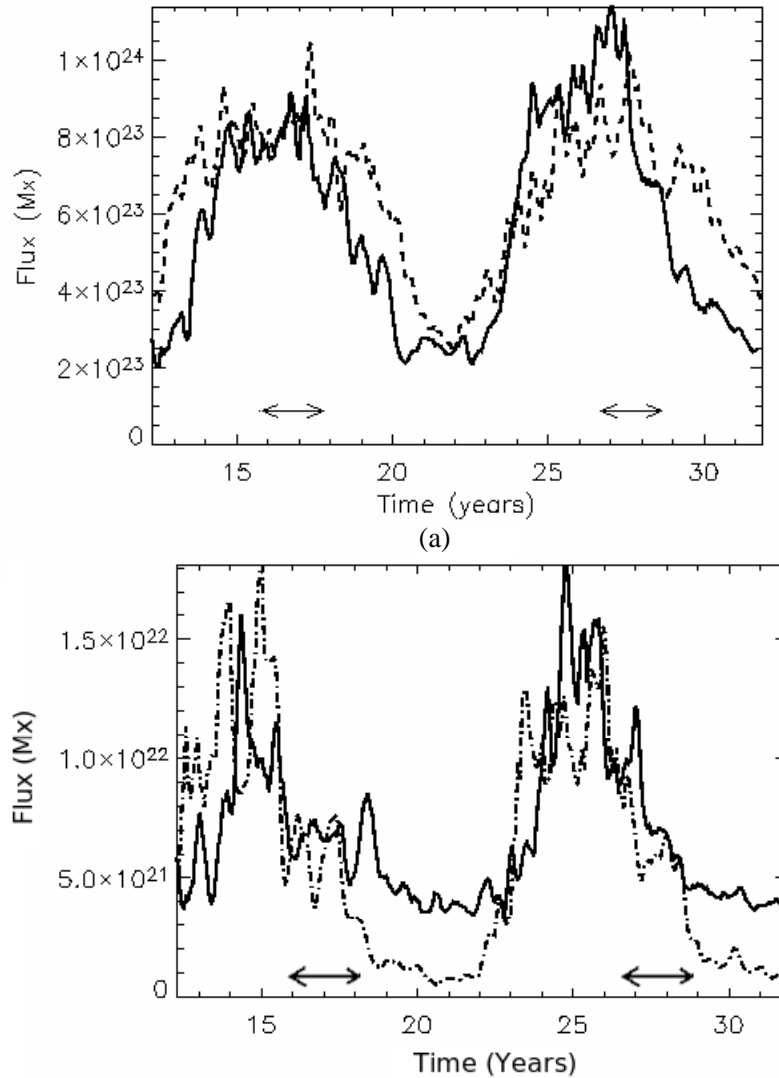


Figure 4.5: Graphs showing the surface flux from our simulated synoptic magnetogram conversion data. Graph (a) shows the total surface flux while (b) shows the flux at 40° latitude. In each case the solid lines denote the flux values deduced from the Kitt Peak synoptic magnetograms where the dashed curve denotes the results of the simulations. The double ended arrows in each graph denote a 2-year time period around cycle maximum determined from the peaks in bipole emergence rate.

synoptic data are a slightly better match to the observed levels of flux within the Kitt Peak synoptic magnetograms than the instant day simulation. Graph (a) shows a plot where the solid line represents the difference in flux between the Kitt peak magnetograms and the simulated synoptic magnetograms, whilst the dashed line represents the difference in flux between the Kitt peak magnetograms and the instant day simulation. This graph allows us to see that, in general, the simulated synoptic magne-

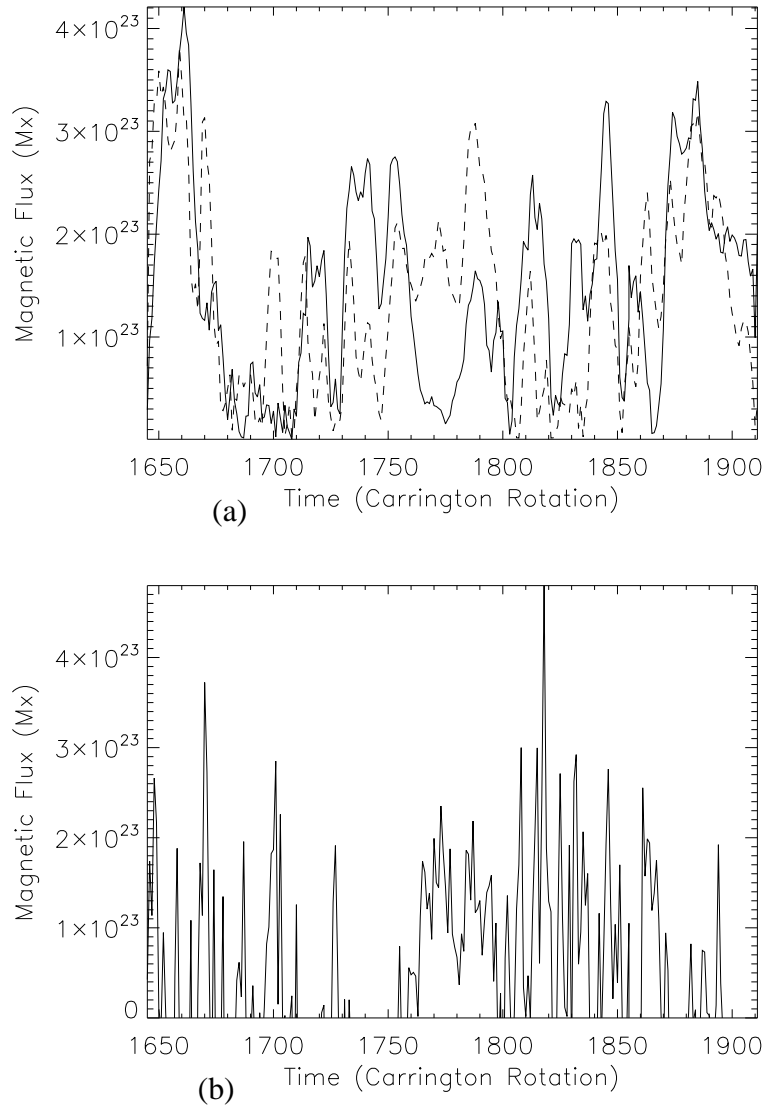


Figure 4.6: Graph (a) shows the difference between the amount of magnetic flux within the Kitt Peak magnetograms and the instant day simulation (dashed line) and the difference between the amount of magnetic flux in the Kitt Peak magnetograms and the simulated synoptic magnetograms (solid line). Graph (b) is a plot of the difference between these two properties, where the range of y has been limited to positive values only. This second graph highlights the points throughout the solar cycle where the flux values within the simulated synoptic maps give a better match to the flux values within the Kitt Peak magnetograms than those within the instant day simulation.

tograms provide a better match to the flux levels of the Kitt Peak magnetograms than the instant day simulation, due mostly to the fact that they are both created in the same way and will miss the same information (see Figure 4.4 for full details on this). Graph (b) shows a plot of the difference between the errors in the flux values of the two sets of data. The y axis has been limited between zero and the

maximum value of this in order to highlight the points during the solar cycle where the flux values of the simulated synoptic data better match the Kitt Peak magnetograms i.e. any point on this graph where positive values are plotted indicates a better match between the simulated synoptic data. This graph shows that, in general, the simulated synoptic data provides a slightly better match to the Kitt Peak data than the instant day simulation. The differences in flux levels, especially around solar maximum, can be seen to provide a closer estimation to the Kitt Peak data. This means that it is prudent to determine the behaviour of coronal null points using both sets of data as a base boundary condition for potential coronal field extrapolation.

4.2 Coronal Null Point Behaviour

Using both sets of the radial magnetic field distributions as base boundary conditions, a potential field is extrapolated out to 2.5 solar radii. This field is then scanned, using the trilinear null finding technique of Haynes et al.(2007) to determine the properties of the null points that are present throughout the two solar cycles. Using the locations of these null points we will investigate the variation of the number of null points throughout the solar cycle, the relationship between the number of emerging bipoles and the number of null points found and the classification of the null points using the underlying surface field configurations that lead to their formation.

4.2.1 Properties of Coronal Null Points

Figure 4.7 represents the variation of coronal null points within the instant day simulation (graphs a and b) and within the simulated synoptic magnetogram simulation (graphs c and d). The graphs show the results for cycles 2 and 3, which have been matched to Kitt Peak Synoptic magnetograms. Graphs (a) and (c) show the variation of coronal null points through the two cycles as a function of time, while graphs (b) and (d) show the variation of coronal null points that are calculated to be linked to the overlying global dipole as a function of time. Here, a null is classed as being linked to the overlying global dipole if one of the field lines plotted immediately around the null point has an end point within the polar regions. In the instant day simulation a sampling rate of 27 days is used. Both sets of data show that the variation of coronal null points varies cyclically throughout the solar

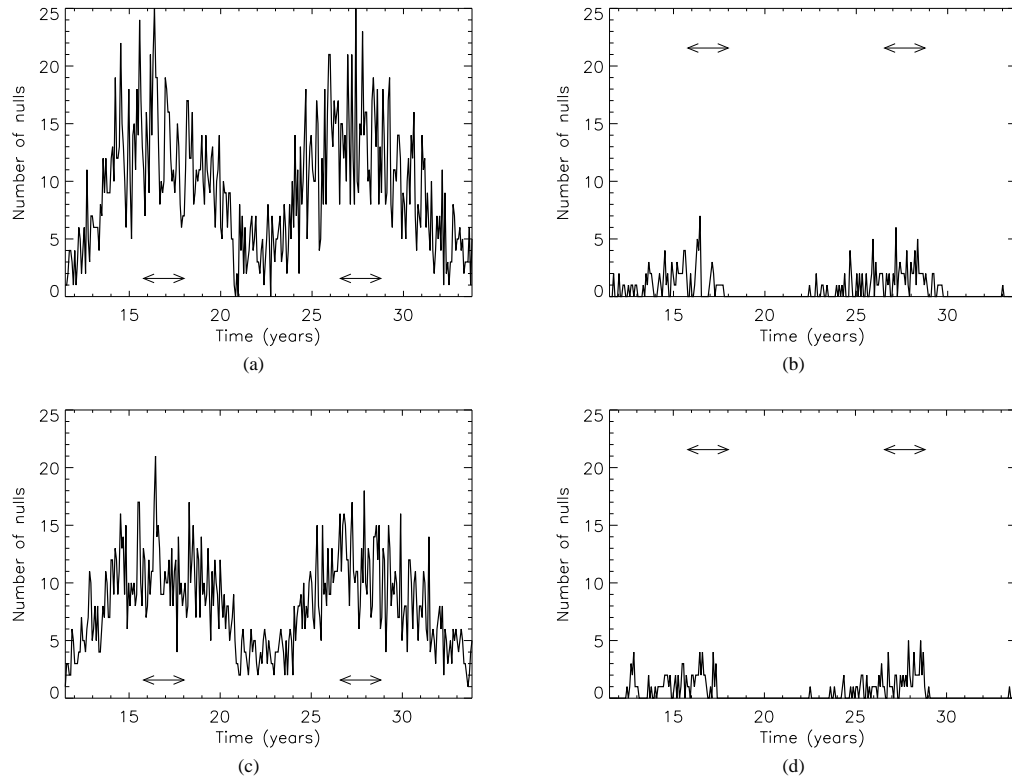


Figure 4.7: Graphs showing the variation in total number of nulls found in (a) the instant day simulation and (c) the simulated synoptic simulation. The number of those nulls connected with the overlying global dipole can also be seen for (b) the instant day map simulation and (d) the simulated synoptic simulation. The double ended arrows in each graph denote a 2-year time period around cycle maximum determined from the peaks in bipole emergence rate

cycle. More null points are present at solar maximum, while fewer null points are detected at solar minimum. This variation suggests that the number of coronal null points present at any time in the solar cycle is dependent upon the emergence rates of solar flux on the solar surface. It is important to note that we are only looking at large scale magnetic flux, and not the small scale flux on the sun.

Direct comparison between the number of null points in the instant day simulation and the number in the simulated synoptic magnetograms also shows another interesting result. In the instant day simulation, there is a total of 2843 null points located, while in the simulated synoptic data only 2437 null points are located. This shows a reduction of approximately 15%. From this, it can be seen that converting the data to the form of synoptic data means that we lose 406 of the total coronal null points (approximately 1/6). This loss of coronal null points stems from the reduction in complexity of the magnetic field that occurs when creating the simulated synoptic magnetograms. This important point

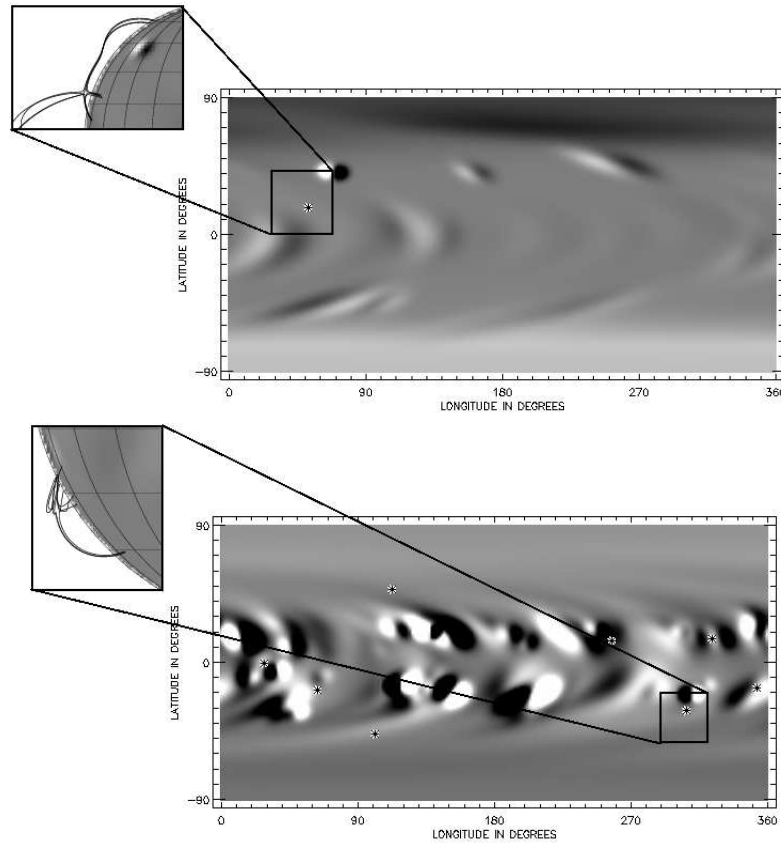


Figure 4.8: Images showing a field line plot around a null that is connected with the overlying global dipole (top) and not connected with the global dipole (bottom).

must be kept in mind when working with observed synoptic magnetogram style data.

Graphs (b) and (d) show the coronal null points that are determined to be connected with the overlying global dipole. This is done by plotting field lines around the null point, and calculating their end points. If either of the end points of the field line is lying in either of the polar regions (north or south), then the null point is determined to be connected with the overlying global dipole. This is because the overlying global dipolar field is deemed to originate within these polar regions. The significance of this quantity is used in order to determine the dependence of coronal null points, and their associated breakout topologies, upon the overlying global dipole and, hence, determine the applicability of the breakout topologies as a possible mechanism for coronal mass ejections throughout the solar cycle. In the instant day simulation only 8% of the total null points are connected with the overlying global dipole, while in the simulated synoptic magnetograms it is only 7%.

Figure 4.8 shows field line plots around two of the coronal null points within the simulation. The top

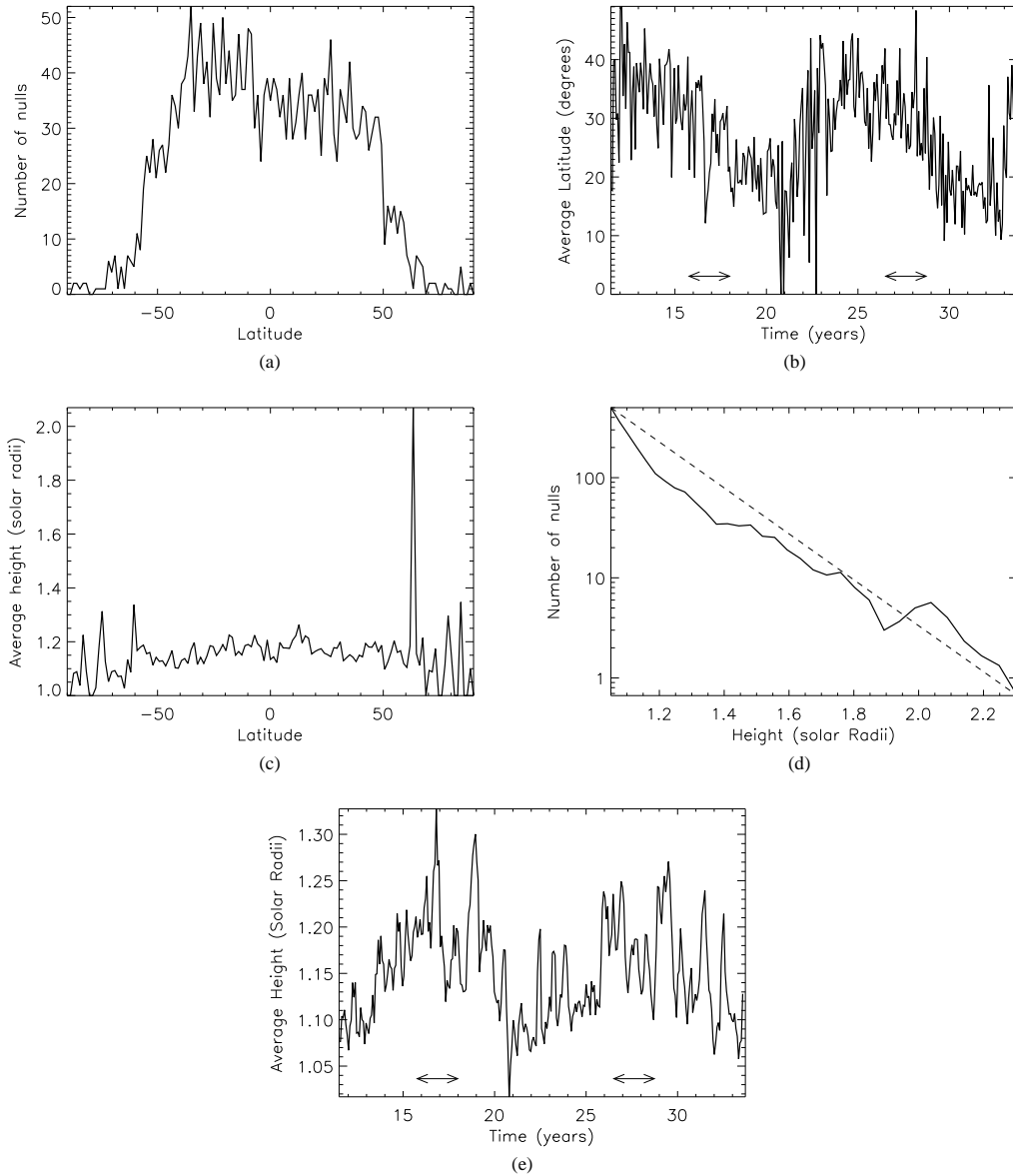


Figure 4.9: Graphs showing the variation of certain properties of coronal null points, located in the instant day simulation. Graph (a) shows the distribution of null points with latitude, (b) shows the average absolute value of latitude as a function of time, (c) shows the average radial height of coronal null points as a function of latitude, (d) shows the number of coronal null points as a function of radial height in the corona and (e) shows the average radial height as a function of time.

image shows a plot around a null point which is connected to the overlying global dipole. The field lines that surround the null point and cause its formation extend and originate up within the polar field (above $\pm 70^\circ$ latitude) on the surface map. This is where the global dipole is known to originate. In the bottom image, the field lines all connect with various polarities from the surface configuration

almost directly below the null point. This means that none of the magnetic field which causes this null to form is connected with the overlying global dipole.

Figure 4.9 shows the variation of null point properties located within the instant day simulations. Similar graphs are found for the simulated synoptic data, however are not shown here as the features present are nearly identical to the features seen in the graphs in Figure 4.9. Figure 4.9(a) shows the distribution of null points with latitude. The majority of null points can be seen to occur within $\pm 50^\circ$ latitude within the active latitudes of the emerging magnetic flux. One of the key features of this graph is the presence of null points over the equatorial region of the Sun. If null points occur in the equatorial plane then the breakout model could possibly account for earthwardly directed CMEs that lie within the equatorial plane. Figure 4.9(b) shows the average absolute value of latitude of null points over time. It can clearly be seen that as the solar cycle progresses the latitude of the null points gets closer to the equator, following the butterfly diagram. This suggests an almost direct link between the null points and the emerging magnetic flux on the sun, which follows this same general behaviour.

Figure 4.9(c) shows the average radial height of the coronal null points as a function of latitude. The average radial height increases slightly as the null points occur closer to the equator, while the average radial height remains very low in the corona (peaking below 1.25 solar radii). Figure 4.9(d) shows the number of coronal nulls against radial height in the corona, represented as a logarithmic plot. From this graph it can be seen that the majority of null points occur below 1.5 solar radii. For comparison, the dashed line denotes a line of slope -3 which indicates that the nulls fall off with radial distance as $1/r^3$. This matches the results of Longcope et al. (2003) who found this relation in terms of isolated point sources.

Figure 4.9(e) shows the average radial height with time. It can clearly be seen that the average height of coronal null points follows a cyclic variation throughout the solar cycle. As the overlying global dipole field weakens, the underlying active latitude flux is able to extend out further into the corona. Throughout the declining phase, the global dipole strengthens, restricting the underlying field from extending out into the solar corona, reducing the height at which coronal null points occur. To consider whether averaging may reduce the slight scatter within the graph and produce simpler trends the present simulation has been extended by adding three additional theoretical cycles. Doing so only

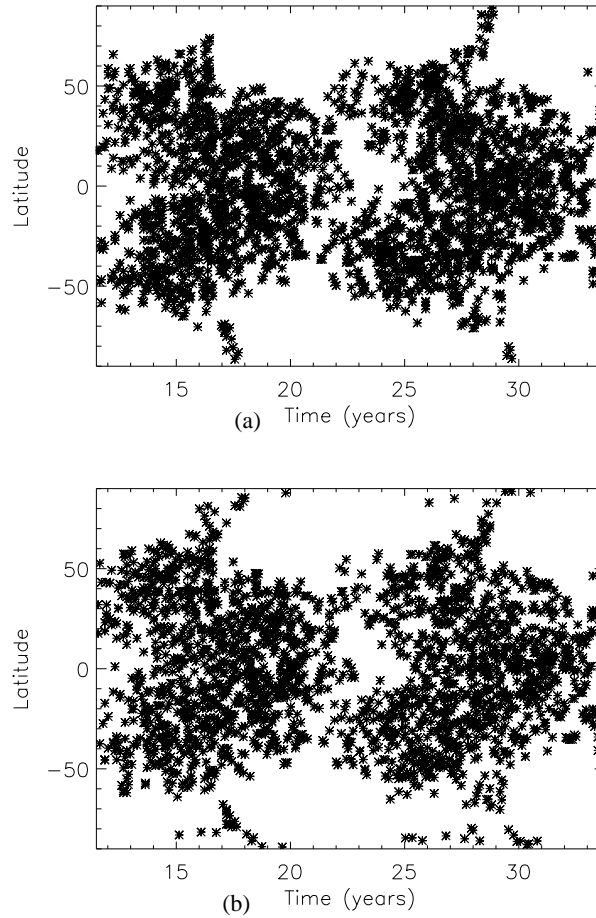


Figure 4.10: Butterfly diagrams showing the distribution of null points in (a) the instant day map simulation and (b) the simulated synoptic magnetogram simulation (right).

slightly reduces the scatter, so we believe that the slight scatter is a true feature where it is the result of the complicated underlying photospheric fields.

Figure 4.10 shows butterfly distributions of the coronal null points in (a) the instant day simulation and (b) the simulated synoptic magnetogram data. The location of null points in both simulation types can be seen to follow the pattern of sunspot emergence, with sunspots emerging closer to the equator as the cycle approaches maximum, and throughout solar minimum. One main difference in the comparison of Figure 4.10 and Figure 4.1(a) is that the null point butterfly diagram has a much wider spread than the bipole emergence butterfly diagram. One noticeable feature of both images in Figure 4.10 is that there is a steady stream of null points that are forming closer to the polar caps at approximately cycle maximum. After solar maximum, and the subsequent reversal in polar field,

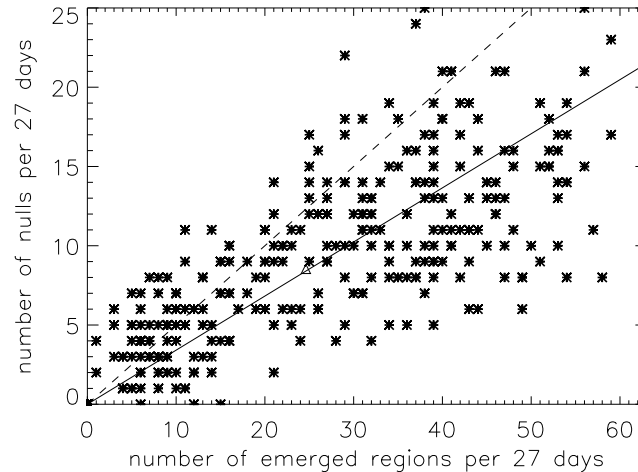


Figure 4.11: A scatter plot of the number of null points found every 27 days vs. the number of bipolar regions emerged every 27 days. The triangle in the centre indicates the mean point of both data sets. The solid line denotes a gradient of $1/3$ while the dashed line $1/2$.

these null points disappear until the following cycle. Each of these null points is connected to the overlying global dipole.

An important result from this study is the dependence of the formation of coronal null points on the underlying active latitude flux. This implies that, as the overlying global dipole field reverses sign just after solar maximum, the occurrence of coronal null points will not disappear throughout the declining phase of the solar cycle. While it is true that some of the null points are linked to the overlying global dipole, the majority are not. The implication of this is that null points will occur throughout all stages of the solar cycle, and the breakout model is applicable throughout all stages of the solar cycle.

4.2.2 Null Numbers in Relation to Bipole Emergence Rates

To fully understand the dependence of coronal null points on lower latitude active region flux, an investigation into the relationship between the number of coronal null points and the emergence rates of magnetic flux is carried out. Figure 4.11 shows a scatter plot of the number of coronal null points discovered every 27 days against the number of bipoles emerged every 27 days. It can be seen that there is a positive, linear association, where the relation of approximately $1/3$ of the bipoles emerged to the number of coronal null points located (this is denoted by the solid line, and a best fit gives a

gradient of 0.29). Even though there is this rough linear fit, it can be seen that there is still a lot of scatter either side of the line of best fit. Generally, this means that, as the number of emerged bipoles increases, the number of coronal null points also increases. The value is less than the theoretical value of $1/2$, where it is assumed that every two bipoles, emerging in a quadrupolar configuration, would produce one null point. This fairly simplified value is derived using the initial setup of the breakout model, where two bipolar active regions produce a single coronal null point. However, this value of $1/2$ is still within the range of the scatter in the diagram. This indicates that active periods of the solar cycle would have more coronal null points than inactive periods and, consequentially, more possible locations would exist for breakout configurations. In Figure 4.11, an interesting feature should be noted when the emergence rates of bipoles is low. When the emergence rate falls below 15 regions per 27 days, a wide scatter is found, and there is no clear relationship between regions emerged and the number of null points located. The upper limit in this scatter provides a near one-to-one relationship between bipoles emerged and null points located. The reason for this is discussed in the next section, where the coronal null points are classified using the surface magnetic flux that causes their creation.

Figure 4.12 shows the number of coronal null points found in the instant day simulation when (a) 100% (8694 bipoles), (b) 75% (6521 bipoles), (c) 50% (4347 bipoles) and (d) only 25% (2173 bipoles) of the bipoles were emerged. The number of bipoles are reduced by randomly removing them from the previous run. It can clearly be seen that, as the number of bipoles emerged within the simulation decreases, the total number of null points decreases. Between Figures 4.12 (a) and (d) where the number of bipoles is reduced by 75% we find that the total number of nulls reduces by 63%. Therefore the loss in number of nulls is slightly less than that of bipoles, but the rates of decrease are consistent with one another and Figure 4.11. Therefore the gradient of $1/3$ obtained in Figure 4.11 only holds for large emergence rates and as the emergence rate dips to lower values, the result is not robust. The reason for this is explained in the next section where the location of null points are considered in relation to the underlying distribution of radial flux at the photosphere.

4.2.3 Null Point Configuration Classification

After locating all of the null points within the instant day simulation, the photospheric distribution that causes the coronal null point to exist is used in order to classify them. The four types of pho-

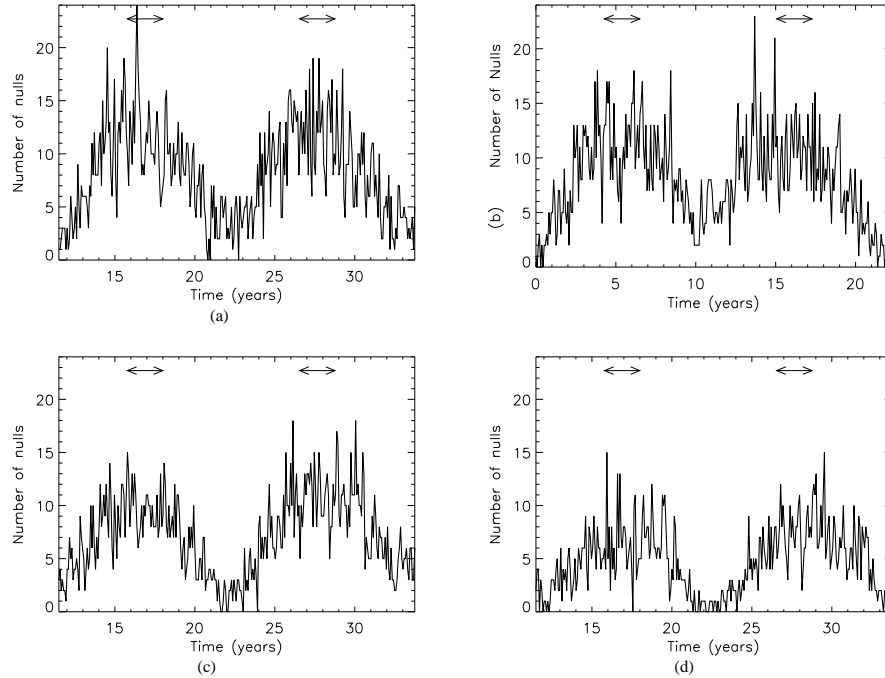


Figure 4.12: Graphs showing (a) the number of nulls found in the instant day map simulation with 100% of the bipoles emerged, (b) the number of nulls found in the instant day map simulation with 75% of the bipoles emerged, (c) the number of nulls found in the instant day map simulation with 50% of the bipoles emerged and (d) the number of nulls found in the instant day map simulation with 25% of the bipoles emerged. The double ended arrows in each graph denote a 2-year time period around cycle maximum determined from the peaks in bipole emergence rate.

photospheric distribution can be seen in Figure 4.13 and are defined as, from left to right, (a) the triple polarity configuration, (b) a newly emerged quadrupolar flux distribution, (c) an enclosed quadrupolar flux distribution which will occur across the equator as bipoles with opposite orientation in each hemisphere interact and (d) an advected quadrupolar flux distribution. In each case the star denotes the location of the coronal null. For each case, the top image gives an idealised photospheric setup, while the bottom image is taken from the instant day simulation and shows an actual example of each of the four photospheric flux distributions. On close inspection it can be seen that cases (b) and (d) are the same topologically. The distinction we are making between them is that (b) is formed by the emergence of bipoles in close proximity, while (d) requires convergence and interaction between the bipoles before a null can form. This information will enable us to determine whether configurations (a) or (d) are responsible for the extended width of the null point butterfly diagram.

Figure 4.14 shows the number and variation of null points that exist, within each of the four config-

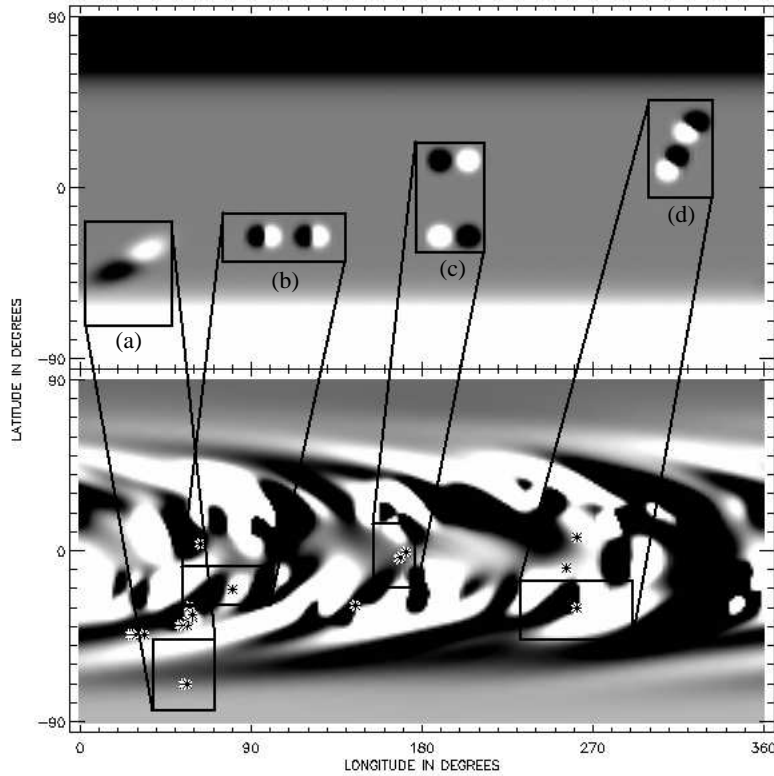


Figure 4.13: Images showing examples of the photospheric flux distributions used in order to classify the null point configuration. The first example (a) is a triple polarity configuration, (b) a newly emerged quadrupolar flux distribution, (c) an enclosed quadrupolar flux distribution and (d) an advected quadrupolar flux distribution.

uration types. It can be seen that the majority of coronal null points occur due to a newly emerged quadrupolar flux system on the photosphere (Figure 4.14(b)). The numbers of coronal nulls of this type of configuration vary cyclically with emerging bipole numbers, indicating their dependence upon the newly emerging bipoles within the solar cycle. Figure 4.14(d) shows the number of coronal nulls that are classified as an advected quadrupolar flux distribution on the solar surface. The number of nulls of this form starts off low at the start of the cycle. Then as the newly emerging surface flux begins to evolve due to meridional flow, differential rotation and diffusion, and bipoles converge towards one-another. This causes the advected quadrupolar formations and associated null points to form. Figure 4.14(a) shows the number of coronal null points that are classified as a triple polarity photospheric configuration. These type of null points seem to occur throughout the rising phase of the cycle, and for a limited time after solar maximum, at which point they do not exist until the following cycle. This is due to the fact that the null points with this classification occur almost exclusively as pictured in Figure 4.13. The null is formed due to the magnetic field from one bipolar region and

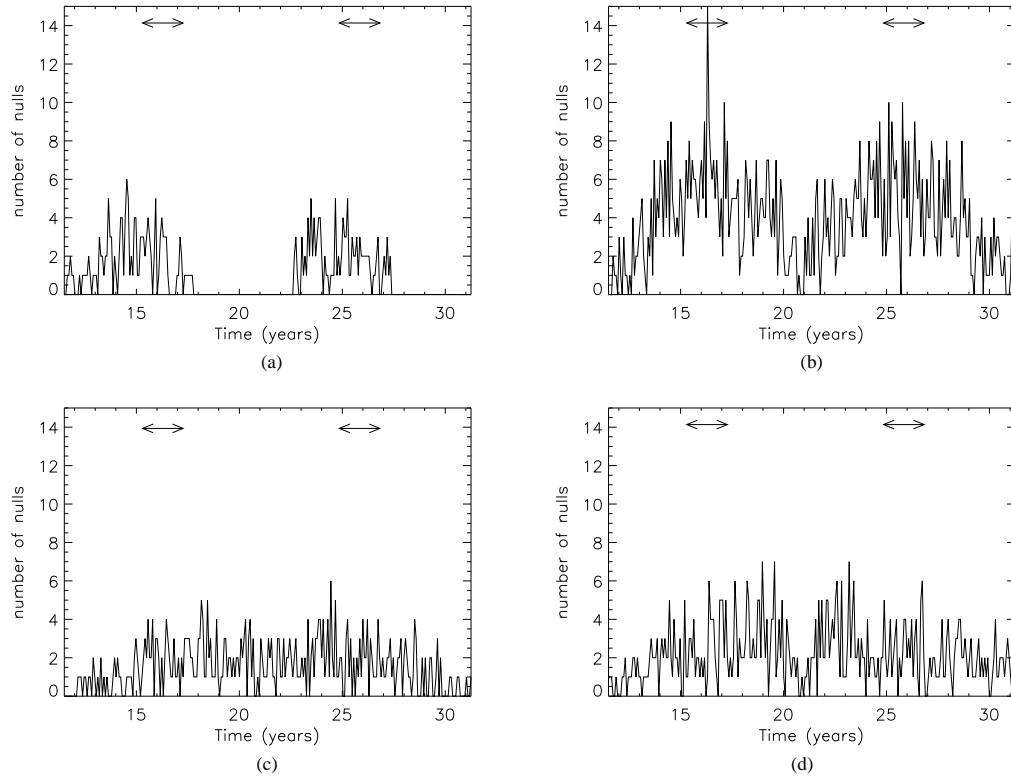


Figure 4.14: Graphs showing the classification of the null points within the instant day simulation. The graphs show results for (a) a triple polarity configuration, (b) newly emerged quadrupolar configuration, (c) an enclosed quadrupolar configuration and (d) advected quadrupolar configuration. The double ended arrows in each graph denote a 2-year time period around cycle maximum determined from the peaks in bipole emergence rate.

the polar field. At the start of the cycle and throughout the rising phase, the bipoles emerge at higher latitudes on the solar surface and in fewer numbers. This will cause several of the bipoles to have connections with the polar field within that hemisphere resulting in coronal null points. Later in the cycle, at approximately solar maximum and throughout the declining phase of the cycle, the bipolar regions emerge at lower latitudes and in greater numbers. This means that there are more interactions between the flux of one bipolar region and another and nulls of a quadrupolar configuration are more likely to occur. This also explains why a 75% decrease in bipole emergence rates only results in a 63% decrease in the number of nulls. When fewer bipoles emerge there is an increased chance of a single bipole interacting with the polar field and producing a null, thus compensating for the decrease based on bipole-bipole interactions. As both the advected quadrupolar and triple polarity configurations have significant numbers this illustrates why the width of the null point butterfly diagram is

much wider than that of the bipole emergence butterfly diagram. Nulls may form at any point as bipoles are advected across the solar surface not just when bipoles emerge. Figure 4.14(c) shows the number of coronal null points that are classified by an enclosed quadrapolar flux configuration on the photosphere. The number of null points of this type remains fairly constant throughout the simulation. A slight peak exists around solar maximum, due to the complexity of the photospheric field at that point, which has the highest rate of emergence. The constancy of this value fits the fact that these null points require cross equatorial interactions and as bipoles emerge throughout the cycle at random longitudes there should be equal probability of this occurring.

In terms of all of the coronal null points that occurred in the simulation, approximately 45.3% had a photospheric flux distribution of the newly emerged quadrapolar type, 25.4% had an advected quadrapolar flux distribution on the photosphere, 17.6% had an enclosed quadrapolar photospheric flux distribution and 11.7% have a triple polarity photospheric flux distribution. The triple polarity photospheric flux distributions are of a higher percentage compared to the number of nulls connected to the global dipole. This is because in some cases the triple-polarity configurations may occur when bipoles interact with uni-polar regions that do not lie at the poles.

4.3 Conclusions

In this Chapter the variation of coronal null points located within the simulation are discussed. Two sets of simulations were run, each with a different base boundary condition. The first simulation, termed the instant day simulation, involved using the time evolution of the radial surface field as the base boundary condition for the simulation. The second simulation involved the conversion of these instant day maps into simulated synoptic magnetograms. These simulated synoptic magnetograms are then used as the base boundary condition in a second simulation. A coronal field is then extrapolated from this out to $2.5R_{\odot}$ in both sets of simulation. This coronal field was then scanned for the location of null points using the trilinear null point finding technique of Haynes et al. (2007). Both simulations yielded similar results.

Coronal null points were found to be connected to the emerging magnetic flux, with little or no dependence upon the overlying global dipole. The emerging active regions provided enough complexity

to the overlying coronal field to account for both the underlying and overlying magnetic flux which caused a null point to occur. This was further justified by the fact that null points were found to occur mainly within the active latitude regions of the sun, $\pm 50^\circ$. This implied that the emerging active regions were directly responsible for forming the majority of coronal null points that occurred in the corona. Upon investigating their connection to the overlying global dipole, null points were found to have very little dependence upon it. This means that the phase of the solar cycle will have no bearing upon whether a null point may or may not occur. Less than 8% of the null points within either simulation were found to be dependent upon magnetic flux from the overlying global dipole. When the latitude location of the coronal null points was plotted against time, a butterfly diagram very similar to that of the magnetic bipole emergence butterfly diagram was found. This implies that the formation of coronal null points has no dependence upon the overlying global dipole. It is the active latitude emerging flux which adds complexity to the overlying coronal field that causes null points to occur. An important point of note here is that we are looking at the evolution of large scale magnetic flux and the effect it has on the evolution of the coronal field and null point numbers. We are not looking at the effects of small scale magnetic flux and the null points produced by this.

The ratio between the number of null points and the number of emerging bipoles was then calculated. This ratio was found to be approximately 1:3 for large emergence rates of bipoles. In the initial configuration of the breakout model, a ratio of 1:2 for nulls to bipoles can be approximated due to the fact that the initial set up of the model has one null point occurring for every two magnetic bipoles that are emerged. However, this new ratio discovered here suggests that, in reality, it is more likely to be a 1:3 ratio of nulls to bipoles for the large emergence rates upon the sun.

After investigating this relationship, it was prudent to categorise the coronal null points. This was done by using the radial surface field configuration that led to the creation of the coronal null point. In doing this, four different types of coronal null point could be classified. These types were a newly emerged quadrupolar configuration, advected quadrupolar configuration, enclosed quadrupolar configuration and a triple polarity configuration. Figure 4.13 gives example set ups for each configuration. Using this technique, 45.3% were classed as being of the newly emerged quadrupolar type, 25.4% had an advected quadrupolar flux distribution on the photosphere, 17.6% had an enclosed quadrupolar photospheric flux distribution and 11.7% have a triple polarity photospheric flux distribution.

Comparison of Null Point Properties with Results From Observations

Chapter 4 described the instant day simulation and subsequent simulated synoptic magnetogram conversions, both of which were used as the base boundary condition for potential field extrapolations. This was necessary as the Kitt Peak synoptic magnetograms were initially deemed unsuitable to be used as the base boundary condition, due to the inaccuracy of the higher latitude flux measurements. However, the properties and variation of coronal null points derived from using the Kitt Peak magnetograms as the base boundary condition, will still provide a good comparison to the results of the main simulations. This allows direct comparisons to be drawn between the variation of coronal null points between the simulation and observations, even though the observations have limitations with regard to the missing flux.

In this Chapter the Kitt Peak synoptic magnetogram data is used as the base boundary condition, and a potential coronal field is extrapolated from each of these. The potential field is then scanned for the existence of coronal null points (using the previously described trilinear technique, see Section 3.3). The properties and variation of the identified null points is then compared to the variation found within the instant day and simulated synoptic simulations. The differences in null point variation between these simulations will then be discussed. This will allow conclusions to be drawn on the validity of the simulations and to the importance of using accurate surface magnetic field measurements when calculating the existence and variation of the coronal null points.

The Chapter is ordered as follows. First, the results from using the Kitt Peak synoptic maps as the base boundary condition are discussed (Section 6.1). Next, these results will be compared with the results from the instant day and simulated synoptic magnetogram data (Section 6.2). Conclusions as to the general behaviour of coronal null points will then be presented (Section 6.3).

5.1 Results from Observations

In this set of simulations, the same set of Kitt Peak magnetograms (cycles 21 and 22) used for flux measurement comparisons are used as the base boundary condition. A potential coronal field is extrapolated out to $2.5R_{\odot}$ and is then scanned for coronal null points using the trilinear method previously described. The variation of these coronal nulls is then compared to the variation from within the instant day and simulated synoptic magnetogram simulations (Chapter 4). In doing this similarities between the two sets of results along with the importance of accurate measurements of the magnetic field on the sun will be highlighted.

Figure 5.1 shows images of radial photospheric field distributions used for potential field extrapolations taken from (a) solar minimum and (b) solar maximum stages of the solar cycle. Image (a) is Carrington rotation 1645, dated August 1976, while image (b) is Carrington rotation 1710, dated June 1981. On each image the polarity inversion lines have been plotted (thin black lines). These images are shown to give examples of the Kitt Peak magnetograms used as a base boundary condition when they are represented in terms of the spherical harmonics previously described (Chapter 2). Both images seem to have highly asymmetric amounts of polar flux, which comes from the fact that the Sun has a axial tilt angle of approximately 7.25° (or 0.1265 radians) throughout the solar cycle. As the earth follows its' orbit around the sun, this tilt angle should cause slightly more of one polar region to be observed and slightly less of another. Both images appear to have been taken at the time when the northern pole of the Sun was tilted away from the observation device, causing a slight loss of data in the northern polar region. This will cause discrepancies in the calculated overlying global dipole as emphasized in Figure 2.15.

The graphs in Figure 5.2 show the results of scanning the coronal field for null points when the observed Kitt Peak magnetograms are used as a base boundary condition for potential field extrapola-

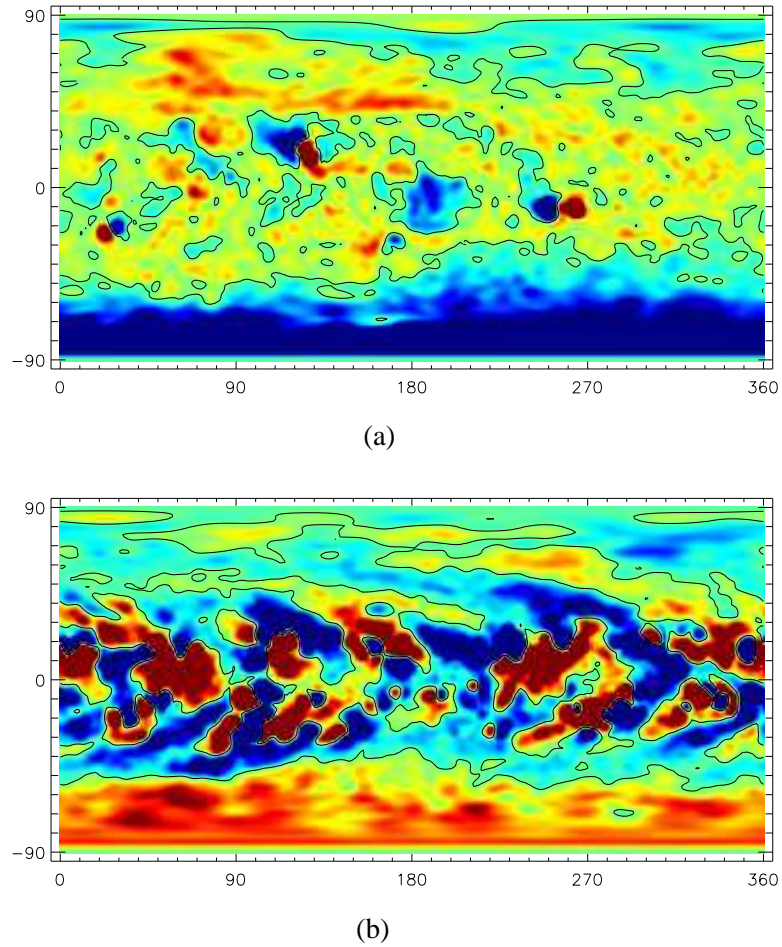


Figure 5.1: Images showing two Kitt Peak magnetograms used as a base boundary condition for potential field extrapolation. Each image is taken from a different stage within the solar cycle. Image (a) is taken from solar minimum (Carrington rotation 1645, dated August 1976) while image (b) shows the photospheric distribution around solar maximum (Carrington rotation 1710, dated June 1981). Each image has the polarity inversion lines drawn on (black lines).

tion. Figure 5.2(a) shows the number of nulls throughout the two observed solar cycles, dating from August 1976 to April 1996. The variation in coronal nulls throughout the solar cycle again follows a distinct pattern that follows the bipole emergence rates. Although it follows this pattern, the pattern is not as distinct as for the simulations in Section 3. This is especially true for the first cycle. It should be noted that for the first cycle the magnetic field measurements were not so systematic or accurate as for the second. During the first year or two of the solar cycle, the number of null points rises rapidly. The number of nulls then remains around the average peak value throughout the rest of the rising phase and solar maximum. During the declining phase, the number of null points then

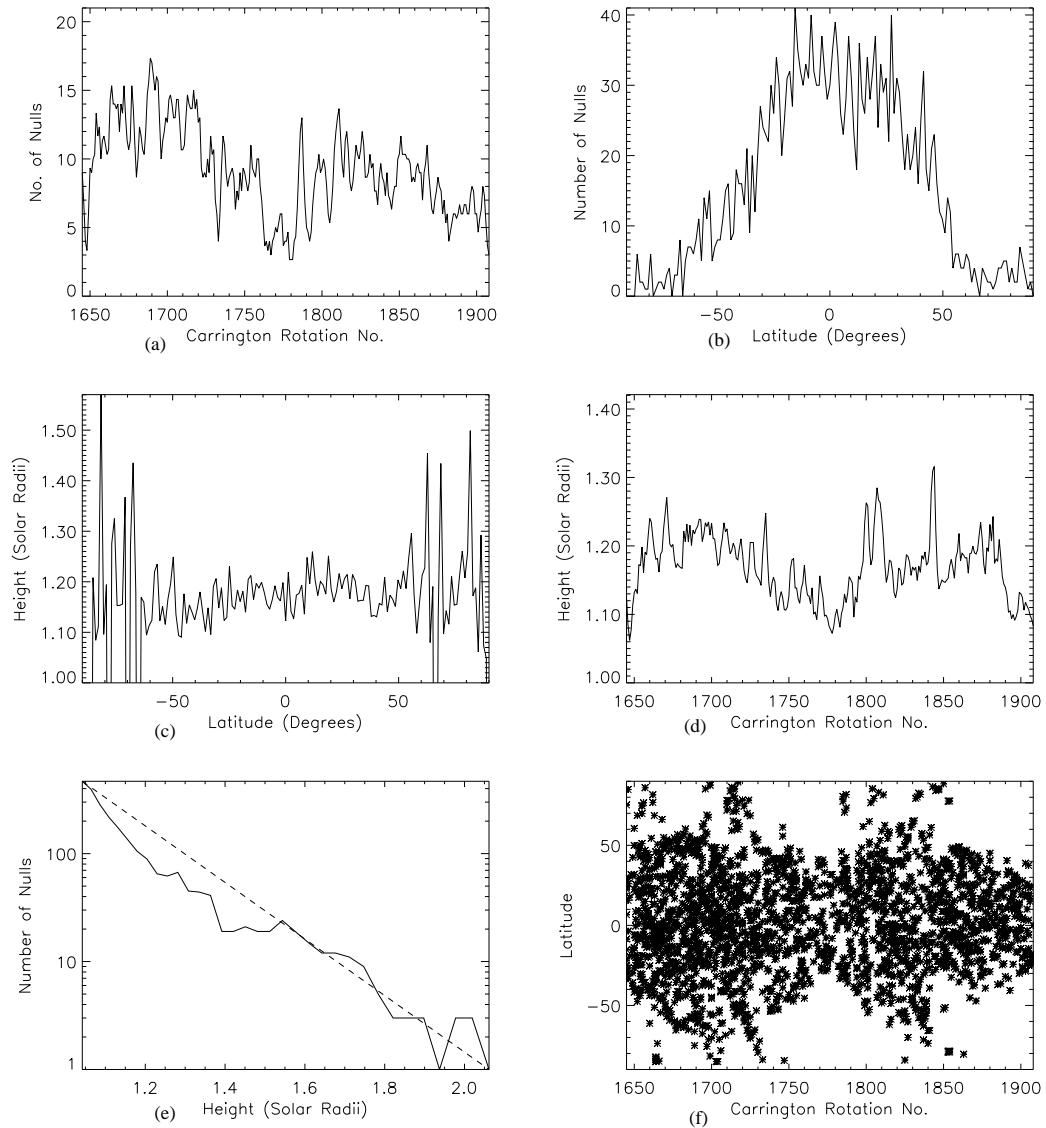


Figure 5.2: Graphs showing the results from a scan for coronal null points determined using the Kitt Peak synoptic maps as a base boundary condition for a potential field extrapolation. Graph (a) shows the number of nulls per map plotted against time, (b) shows a plot of the number of nulls against latitude, (c) shows the average height of the null points plotted against latitude, (d) shows the average radial height of the null points with time, (e) shows the number of null points with radial height plotted on a logarithmic axis in y, with a straight line indicating the gradient of the line of best fit plotted over and (f) shows a butterfly plot of the null point latitudes with time.

gradually decreases until solar minimum. The number of nulls peaks around solar maximum in both cycles. During solar minimum there are significantly less null points located due to there being less emerging magnetic flux on the solar surface. The peak in the number of null points in the first cycle

is around 14 nulls, while the second cycle peaks around 12 nulls. This variation in the peak number of null points is one of the key differences that will be discussed in Section 6.2. In Figure 5.2(a) the second cycle shows a behaviour closer to what was found in Section 4. It should be noted that in the Kitt Peak maps the second cycle, which goes from Carrington rotation 1780 until Carrington rotation 1908, involves more accurate and detailed flux measurements than the first.

Figure 5.2(b) shows the number of null points with latitude. At lower latitudes (between approximately $\pm 30^\circ$ latitude), there are a higher number of null points, the peak value of which is about 30 nulls, occurs over the equator. However, above these latitudes the number of null points drop off fairly rapidly as the magnitude of latitude increases, giving a thin region around the equator where the number of null points is higher. This profile may be the result of the higher latitude fields being inaccurate.

Figure 5.2(c) shows the average radial height of the null points plotted with latitude. The average height of the null points can be seen to remain fairly constant across most latitudes on the sun. The peak value of around $1.18R_\odot$ holds constant throughout the active latitude region of the solar surface, $\pm 50^\circ$ latitude. Above these latitudes, the average radial height of the null points seems to increase slightly. This can be attributed to (i) very few nulls being located at these latitudes, hence increasing the average radial height, and (ii) the inaccuracy of the Kitt Peak measurements at these latitudes. These inaccuracies mean that the surface magnetic field in these regions is incorrectly measured and modeled, hence the polar field extrapolations will not show an accurate representation of the actual coronal field at this latitude. This trend is similar to what is found in the simulations and gives us confidence that the simulated data is accurately modeled.

Figure 5.2(d) shows the average height of the null points with time. The average height of coronal null points can clearly be seen to rise rapidly during the rising phase of the cycle. The height of the null points peaks after approximately one year, and then remains fairly consistent for the majority of the remaining cycle, until approximately solar maximum. After solar maximum, a steady decline in the average radial height of the null points occurs until approximately solar minimum, at which point the nulls are located at their lowest height in the solar corona. The peak height of the null points in the first cycle is approximately $1.17R_\odot$, while in the second cycle it is around $1.15R_\odot$, which suggests a fairly consistent peak in the average height of the null points between cycles. This trend is similar to

what is found in the simulations.

Figure 5.2(e) is a plot of the number of null points with radial height, plotted on logarithmic axes. The dashed line indicates the gradient of the line of best fit. The number of null points located at a height just above the solar surface is very high. This number then falls off rapidly with height. Above $2.05R_{\odot}$ almost no null points are located. The dotted line on the graph indicates a plot of the line of best fit. This line has a steeper gradient when using the Kitt Peak observed data of approximately 5 (i.e. the variation of coronal null points falls off as approximately $\frac{1}{r^5}$). This is greater than within the simulated data but can be attributed to the inaccurate modeling of the overlying global dipole field, which originates within the polar regions of the sun, and emphasizes the importance of accurate modeling of the polar field on the solar surface, as this is where the overlying global dipole originates.

Figure 5.2(f) is a butterfly plot of the latitude of null point occurrence. In this image, the butterfly pattern of the null points is clearly visible. At solar minimum, the spread in latitude of the null points is slightly greater than expected from the earlier simulation, but well within acceptable limits and not hugely extreme. The latitude of the null points should follow the emergence patterns of the surface magnetic bipoles, implying that the latitude of occurrence should occur closer to the equator and at lower latitudes throughout the declining phase and at solar minimum. Here such a feature is found but there is a slightly wider spread in the null point latitudes at solar minimum than in the previous simulations. A further key point of this image is that, throughout both cycles there are distinct clusters of null points that occur above $\pm 50^{\circ}$ latitude. After solar maximum, these null points would be expected to disappear and not to occur due to the reversal of the sign of the polar field. In general this occurs, but the pattern is not so distinct as in the previous simulations.

The results from Figure 5.2 are compared to the results from the instant day and simulated synoptic magnetogram data presented in Chapter 4. This will highlight the key difference between the two sets of simulations, and allows us to directly compare the two sets of results in order to deduce how much of an impact the accurate modeling of the overlying global dipole and polar field will have on the calculated variation of coronal null points.

5.2 Comparison Between Kitt Peak Observational Results and Simulation Results

The calculated variation of coronal null points within the instant day and simulated synoptic magnetograms (see Chapter 4) is now compared to the calculated variation within Figure 5.2.

Figure 5.2(a) shows a plot of the number of coronal null points that occur with time when the Kitt Peak magnetograms are used as a base boundary condition for potential field extrapolation. This graph can be compared with Figure 4.6(a) and (c). These plots show the number of null points when using the instant day maps (Figure 4.6(a)) and the simulated synoptic magnetograms (Figure 4.6(c)) as a base boundary condition for potential field extrapolation. The cyclic variation that is present within the null point numbers within the instant day and simulated synoptic magnetograms is present, but not as well defined, within the Kitt Peak results. The null point numbers in Figure 5.2(a) are peaking within the first year or two of the solar cycle. In the first cycle, the numbers seem to remain fairly consistent until during the declining phase, at which point the number of null points gradually declines. In contrast, for the second cycle a more cyclic behaviour is found. This is probably due to the fact that the later measurements are more accurate with measurements taken more regularly at Kitt Peak. This second cycle does follow the previously described pattern where the number of null points follows the emergence rates of magnetic bipoles: As the number of bipoles emerging increases, the amount of magnetic flux present increases, and hence the number of coronal null points increases. Another key point in comparing the two sets of graphs is the peak value of coronal null points in each graph. The peak value of null points between cycles when using the Kitt Peak magnetograms is approximately 15 nulls in the first cycle and approximately 12 in the second cycle. Comparing this with the peak values observed in the instant day simulation, which was approximately 16 nulls per cycle shows a reasonable match in terms of peak value of null points. Comparing the peak values of using the Kitt Peak data to using the simulated synoptic magnetograms, which peak at around 11/12 null points per cycle, shows a very good match, particularly in the second cycle. This illustrates the fact that by using synoptic data some information as to the magnetic flux on the solar surface may be lost. The variation of the numbers of coronal null points around this peak value is less than that of the variation within the instant day simulation. This shows that the general variation of null point numbers when using the Kitt Peak magnetograms as a base boundary condition gives a reasonable

match to those calculated in the earlier simulations.

Figure 5.2(b) shows a plot of the number of coronal null points versus latitude. This figure is comparable with Figure 4.8(a). Both graphs show that the number of null points with latitude peaks around the equator. The peak number of the null points around this latitude when using the Kitt Peak magnetograms is approximately 30, while in the instant day simulations the peak in null point numbers is 35. One key difference between the images is the width of the section within which most of the null points lie. In the instant day and simulated synoptic magnetogram data, the null points lie mainly within the active latitude on the solar surface, between $\pm 50^\circ$ latitude. However, when using the Kitt Peak magnetograms, the majority of the null points appear to lie between $\pm 35^\circ$ latitude. This thinner peak section in the observations is due to the fact that the field above $\pm 35^\circ$ latitude in the Kitt Peak magnetograms has some inaccuracies within it due to line of sight effects previously described. Null points were previously shown to occur throughout all active latitudes, and the results from Figure 5.2(b) suggests a much thinner active latitude band where the null points would occur. However, we still see the same general behaviour in null point occurrence, with more nulls occurring across the solar equator and throughout the active latitudes of the Sun. The numbers of nulls then decline as we move higher into the higher latitude and polar regions of the Sun. This gives us confidence that the general behaviour of null points versus latitude has been correctly calculated, despite the small discrepancies that occur due to the higher latitude polar fields having a slight error in them from the Kitt Peak magnetograms.

Figure 5.2(c) shows a plot of the average radial height of the null points versus latitude when using the Kitt Peak magnetograms. This graph is comparable with Figure 4.8(c). Both graphs show similar variations in the average radial height of the null points at lower latitudes on the sun. The average height peaks around the equator and decreases as latitude increases. The average peak radial height around the equator when using the Kitt Peak magnetograms is $1.18R_\odot$, which is approximately the same as when using the instant day and simulated synoptic data. This shows a good match between the three sets of simulations at lower latitudes. At higher latitudes, the variation in the average height of the coronal null points has a greater variation than found within the instant day and simulated synoptic magnetogram data. This variation is due to the inaccuracies in the dipole strength from one rotation to the next within the Kitt Peak magnetograms. This also shows that there is a good match between the simulations at lower latitudes and the Kitt Peak magnetograms.

Figure 5.2(d) shows the average radial height of the coronal null points versus time when using the Kitt Peak magnetograms as a base boundary condition for potential field extrapolation. This graph is comparable with Figure 4.8(e). Figure 5.2(d) shows that, when the Kitt Peak magnetograms are used as a base boundary condition for potential field extrapolation, the average height of the null points peaks early in the cycle at around $1.2R_{\odot}$ in the first cycle. This height then remains fairly constant until the declining phase, when it slightly decreases. The second cycle shows a slightly more distinct cyclic variation, again attributed to the more accurate measurements that occurred at this time. There is a steady increase in the height of the null points until around solar maximum, where it peaks at $1.16R_{\odot}$. The average height then varies around this value until the declining phase of the cycle, at which point it steadily decreases. This shows that the variation of the average height of the coronal null points, especially in the second cycle, varies in sync with the previously calculated variation. Initially, the number of null points and average radial height of the null points peaks within the first year of the cycle. Throughout the cycle, the average radial height and number of null points remains constant around the peak value until the declining phase. During the declining phase, they then decrease until solar minimum. This shows a fairly good match, especially in the second cycle, to the previously calculated variation within the instant day and simulated synoptic magnetogram simulations.

Figure 5.2(e) shows the number of null points versus radial height plotted on logarithmic axis in the y direction. This is comparable with Figure 4.8(d). At lower heights, there are more null points that occur due to the emerging magnetic flux on the photosphere. As the radial height increases, the number of null points decreases. This follows the previously calculated variation. One of the key differences is that when using the Kitt Peak synoptic magnetograms as a base boundary condition for potential field extrapolation, very few null points, if any, are located above $1.95R_{\odot}$. However, Figure 4.8(d) shows that there are significantly more null points above $1.95R_{\odot}$, up to the outer boundary of the coronal field extrapolation. The difference in results can be explained by the slight discrepancies that occur in the measurement of the photospheric flux at higher latitudes within the Kitt Peak magnetograms (see Figure 2.15). As the global dipole originates from here, this will lead to the extrapolation of an overlying coronal field with slight discrepancies, which accounts for the differences at this height. However, given the similarities in the general behaviour of the coronal null points, we can be confident that the correct variation has been calculated.

Figure 5.2(f) shows a butterfly plot of the null point latitudes with time within the Kitt Peak simulation. This is comparable to Figure 4.9. There are some differences between the previously calculated butterfly diagrams of the instant day and simulated synoptic simulations, but these are minor. At the start of the solar cycle, the null points will occur at higher latitudes. We conclude this based on the work in earlier chapters where we were able to say that, in general, the formation of nulls points depends upon the interactions of the emerging magnetic flux on the photosphere. The latitude of null point occurrence then decreases throughout the solar cycle until solar minimum, at which point the null points occur at lower latitudes closer to the equator. This follows the pattern of magnetic bipole emergence known on the solar surface. While this pattern is not as distinct when using the Kitt Peak magnetograms as a base boundary condition, the null points follow the general behaviour previously calculated, with a slightly wider spread. In Figure 4.9, there are visible streaks of null points heading towards the polar region just prior to reversal. Figure 5.2(f) shows null points occurring in these streaks mainly around solar maximum, but also some others throughout the solar cycle. In general, this fits the behaviour found before.

5.3 Conclusions

In this chapter, the variation of coronal null points when using the Kitt Peak synoptic magnetograms as a base boundary condition for potential field extrapolations has been compared with the earlier null point variation calculated within the instant day and simulated synoptic magnetogram simulations.

The variation of coronal null points throughout the solar cycle when using the Kitt Peak magnetograms differs only slightly from the variation previously calculated in Section 4. The majority of the differences occur in the first cycle between the dates of August 1976 and June 1986, when flux measurements were not so systematic or accurate. The number of null points peaks very early in the first solar cycle, after a year or so. However, in the second cycle, where more accurate measurements exist, a behaviour consistent with the simulation is found. The average radial height of the null points follows a similar variation, peaking early within the cycle, remaining around this height until the declining phase, at which point the average radial height decreases. The number of null points with latitude when using the Kitt Peak magnetograms follows a similar variation to the variation calculated in Section 4 at lower latitudes. The number of nulls peaks over the equator and remains fairly high

as the latitude increases. However, in contrast to the previously calculated variation, the number of nulls with latitude begins to drop off above $\pm 35^\circ$. This differs from the previously calculated variation, in which null points occurred at a fairly high rate throughout all of the active latitudes on the sun, between $\pm 50^\circ$. This may be due to the inaccuracies in the observed maps at higher latitudes. The average radial height of the null points with latitude when using the Kitt Peak magnetograms also follows a variation similar to that previously documented in Section 4, at lower latitudes. The average height of the null points peaks around the equator at a height of approximately $1.18R_\odot$. As the magnitude of latitude increases up to about $\pm 50^\circ$, the average radial height of the null points decreases slightly. However, above these latitudes the average radial height of the null points shows a greater variation compared to the simulations. This is due to the inaccuracies that exist within the Kitt Peak magnetograms above $\pm 50^\circ$ latitude. The plot of the null point latitudes with time when using the Kitt Peak magnetograms did show the known butterfly pattern of null point latitudes, but with a slightly wider spread early on in the cycle compared to that calculated in the instant day or simulated synoptic data. This variation can be attributed to the inaccuracies that may occur due to the line of sight measurements resulting in inaccurate higher latitude field measurements.

Using these comparisons of the behaviour of the coronal null points over two solar cycles, several key conclusions can be drawn. The first is that the inaccuracies within the calculated variation in coronal null points when using the Kitt Peak magnetograms as a base boundary condition cause several inconsistencies within the calculated variation of the coronal null points. This is due to the higher latitude photospheric field measurements being underestimated which affects the extrapolated coronal fields, especially the overlying global dipole element, which is known to originate within the polar field region. Given the fairly reasonable match between the variation of aspects of the coronal nulls at lower latitudes between the two sets of simulations, it can be concluded that the earlier simulations do accurately model the variation of coronal null points and produces clearer trends. Matching the earlier simulation to the Kitt Peak magnetograms via flux measurements at lower latitudes has given a good match between the variation of the coronal null points at these latitudes. This means that the higher latitude field, and hence overlying global dipole, in the instant day and simulated synoptic data will be accurately modeled and provide a good representation of the actual variation of coronal null points within these regions. Using the variation of coronal null point height within both sets of simulations, it can also be concluded that the coronal null points that occur

throughout the solar cycle are dependent upon the emerging magnetic flux on the photosphere and its contribution to the overlying coronal field. Using both sets of results, it can be concluded that null points are mainly produced from the low latitude emerging magnetic flux on the photospheric surface, with the overlying global dipole not playing a key role. Both sets of results show that null points mostly occur at fairly low radial heights within the corona throughout the solar cycle. Null point numbers would also be expected to decline throughout the declining phase of the cycle until the new cycle. Both sets of simulations show null points occurring at all stages throughout the solar cycle and null point occurrence is not dependent upon the overlying global dipole.

6

How Many Breakout Configurations May In Fact Breakout?

The study of coronal null points is currently a key area of research in solar physics. Null points are of interest as they are sites where magnetic reconnection can take place and energy release within the solar atmosphere may occur (Pontin et al., 2004; Aulanier et al., 2005; Pariat et al., 2006; Priest et al., 2003). In the paper of Antiochos (1998) (see also Antiochos et al. (1999); MacNeice et al. (2004); Lynch et al. (2004); Choe et al. (2005)) a coronal null point plays a key role in the escape of Coronal Mass Ejections (CMEs) from the Sun, in what is called the *Magnetic Breakout Model*. The initial configuration of the model consists of a quadrupolar photospheric flux distribution forming a coronal field with four distinct flux domains. The field lines within the two domains which pass over the equator are oppositely orientated to one-another. Between them lies a coronal null point. This coronal null point is a key feature; when the field underneath it is stressed, reconnection may occur allowing the underlying flux to break out. Whilst in a 2D situation a null point is required for reconnection to occur, in a 3D situation, reconnection may also occur at other locations without nulls, such as current sheets (Priest & Démoulin, 1995; Démoulin et al., 1996; Hornig & Priest, 2003; Titov et al., 2003; Galsgaard et al., 2003; Pontin et al., 2005; Haynes et al., 2007). For simplicity, to determine the relevance of the magnetic breakout model, the focus of the study within this thesis has been the existence and variation of coronal null points as they are an easily identifiable topological feature and a key element in the initial configuration of breakout topologies as described by Antiochos

(1998). Thus we use as a proxy the variation of these null points to indicate the variation of possible breakout topologies and CMEs associated with them.

Even though a coronal null point exists, it does not necessarily mean that a CME will be able to break out in the manor described by Antiochos (1998). This is because a necessary, but not sufficient condition for the escape of a CME through the overlying flux, is that more flux must lie below the null than above. Only if this condition is satisfied will the underlying flux be able to reconnect through the overlying flux. In this Chapter, a simple calculation of the amount of magnetic flux above and below each null point is employed. This will indicate how many of the null points may be the sites of allowed CME ejections, via reconnection removing the overlying field.

An important point to note here is the simplicity of the assumed model. Here we are merely looking at the flux above and below the null point in a single snap shot. We do not track the evolution of the fluxes above and below the null throughout time, which means that the model here is being used as a simple way of estimating the number of null points that may or may not breakout. If continued emergence were to be calculated between snapshots at a null point, this may cause variations in the calculated flux above or below the null point. The connections around the null point may even change due to the emergence of magnetic bipoles within the surface configuration which will have an affect upon the overlying field configuration. The model used here also assumes that reconnection only occurs at the null point, when, in reality, 3D reconnection can occur at a variety of sites, including 3D separators. These key points indicate that the simplified model presented here provides just a simple estimate of the applicability of the breakout model throughout the cycle.

In this Chapter, the order is presented as follows: First, a description of the method used in order to determine the amount of flux above and below each null point is given (Section 5.1). Following this, two examples of null points from within the simulation are illustrated (Section 5.2). The results of determining the amount of flux above and below each of the null points, throughout both cycles of the simulation are given (Section 5.3). Conclusions as to the applicability of the breakout model in relation to the work carried out within this chapter are then described (Section 5.4).

6.1 Calculating the flux above and below the null points

Using the locations of the 2843 coronal null points from the Instant Day simulations, a simple calculation of the amount of flux above and below each null point is made. To determine the amount of flux lying above and below each null point, the following process is applied,

1. First the path of the polarity inversion line (PIL) lying on the radial shell directly below each null point is computed. From this path a radial projection of it out to $2.5R_{\odot}$ is made which produces a radial surface, that runs along the PIL and contains the coronal null point. The radial plane directly below the null point is used in every case in order that we can ensure that the PIL directly below the null point goes through or is very close to the null point itself.
2. At each grid cell along the PIL the quantity of $-\nabla B_r$ is computed. This quantity will have a normal to the PIL and points in the direction of positive to negative flux. The unit normal vector may then be calculated, $\hat{n} = \frac{-\nabla B_r}{|-\nabla B_r|}$, which will be perpendicular to the PIL calculated on the radial shell directly below the null point.
3. Once the unit normal to the plane has been found, it can then be used to determine the flux that passes through the plane at all radial heights.

Figure 6.1 shows an illustration of the radial plane extrapolation technique. The green square shows the location of the coronal null point around which the calculation is carried out. The blue area denotes magnetic field that passes over the PIL in the direction of $-\hat{n}$ (i.e. in the opposite direction to the unit normal), red in the direction of \hat{n} . The white line denotes the separatrix surface where there is a rapid change in the field orientation (denoted by a sign change). This shows that calculating the rapid sign change in the magnetic field and using this to indicate the location of the separatrix is essential to ensure correct flux values are calculated for both the overlying and underlying flux. This example is created purely in order to provide a description and reasoning for the techniques given here and it is clear what flux lies below (is enclosed) and what flux lies above (overlying flux) the null point. The projection of the magnetic field in the direction normal to the plane is then multiplied by the area of the relevant grid cell through which it is projected. These magnetic field projections are then used to calculate the height of the separatrix surface on which the null point lies. For each radial height, the

normal field of the current grid cell is multiplied by the normal field through the grid cell at the next radial height. Should $B_{n1} \times B_{n2} < 0$, where B_{n1} indicates the projection through the current grid cell and B_{n2} indicates the projection through the grid cell above, then this indicates a sign change in the magnetic field through the plane. This sign change indicates the position of the separatrix (examples of this will be shown in Figures 6.3 and 6.5). All of the calculated magnetic flux above the null is summed as the flux above the null point, while all of the calculated flux below is summed as the flux below the null point.

Once the amount of magnetic flux above and below the null has been calculated, a conclusion regarding the magnetic fields ability to breakout can then be drawn. If the amount of flux below the null point is greater than the amount of flux above, then all of the overlying magnetic flux may be removed via reconnection. This would allow the underlying flux to eject out from the solar corona, resulting in a CME. Conversely, should there be more magnetic flux above the null point than below, then reconnection at the null point cannot remove all of the overlying flux. This means that the underlying magnetic field would continue to be restricted by the overlying coronal field, and ejection via the removal of the overlying coronal field would not be possible. In which case, if an eruption were to occur then it may be confined.

A key point when calculating the flux above and below the null point is the length of the polarity inversion line along which the radial plane is calculated. If the polarity inversion line is too short, then essential flux that could contribute to the complexity of the magnetic field around the coronal null point would be missed from the calculation. If the polarity inversion line is too long, then flux that does not contribute to the complexity of the magnetic field around the coronal null point would be included in the calculation. In order to account for this, computations are run with a variety of lengths along the polarity inversion line. These range from considering only the immediate grid point around the null, to 5 grid points either side of the null point (11 grid points in total). The length of the polarity inversion line then ranges from 25,000 km for a single grid point up to approximately 250,000 km for 11 grid points. Five grid points either side was taken as the maximum length of the polarity inversion line due to convergence of the results when symmetrically increasing the number of grid points up to 11 (the immediate grid point around the null and five either side of this).

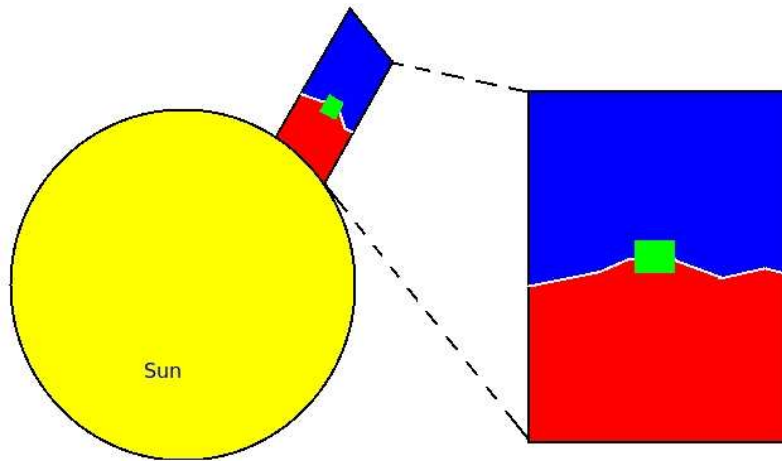


Figure 6.1: Illustration showing extrapolating the radial plane from the solar surface out to 2.5 solar radii. The direction of the magnetic field through the extrapolated plane is then calculated. The plane red indicates a negative direction of magnetic field, blue indicates positive magnetic field, relative to the unit normal $\hat{n} = \frac{-\nabla B_r}{|-\nabla B_r|}$. The white line is the separatrix along which there is a rapid reversal of the field components with height and the green dot shows the position of the null point relative to the plane and separatrix position.

Figure 6.2 shows images taken from one null point example within the simulation, which illustrates the technique. They show (a) field lines plotted above and below the separatrix along the polarity inversion line and (b) an image indicating the sign of the normal field above and below the separatrix (relative to the direction of the unit normal vector \hat{n}), plotted in terms of distance along the PIL versus radial height. Blue indicates positive field in the direction of the unit normal, red indicates negative field. The separatrix upon which the coronal null point lies is clearly not a straight line, but curved. This means that it is necessary to check the sign of the field along the polarity inversion line as the radial plane is traversed.

Using the above method to estimate the amount of flux above and below the null point provides an approximation. This will allow us to estimate the number of these null points that could, potentially, breakout as in the breakout model. We hope to get a good approximation of the ratio of flux above the null to the flux below and get an idea as to if the null point can breakout. A more robust technique would be to determine all the separatrix surfaces, however, this is beyond the scope of the present study. Once the flux above and below the null point has been calculated, a comparison between them is drawn. If flux below is greater than the flux above, this implies that reconnection at the null point may remove the overlying coronal field, allowing the underlying magnetic flux to breakout. If

flux below is less than flux above, then reconnection at the null point would not completely remove the overlying magnetic flux. This means that, should ejection occur, some other mechanism will be required in order to explain the removal of the overlying magnetic field or the ejection of the underlying magnetic flux. Alternatively, there may be a confined ejection. Examples of the above calculations will now be presented for two coronal nulls, one taken at solar maximum and one taken at solar minimum.

6.2 Calculating the Flux Above and Below the Null Points: Two Examples

The plots in Figures 6.2 - 6.5 show images taken from two examples of coronal null points within the simulation. Figures 6.2 and 6.3 are taken for a null point at solar minimum, while Figures 6.4 and 6.5 are taken for a null point occurring around solar maximum. Figures 6.2 and 6.4 show images indicating (a) the surface field distribution, along with field lines and (b) the direction of the magnetic field through the radial plane in which the null point lies, relative to the unit normal $\hat{n} = \frac{-\nabla B_r}{|-\nabla B_r|}$. For each case in (b) where the planes are shown red indicates field in the direction of \hat{n} , while blue indicates field in the direction of $-\hat{n}$. It can clearly be seen that the null point taken at solar minimum, given by the green square, is located lower down in the solar corona. This is due to the strong overlying dipolar field that is present at solar minimum, restricting the lower lying field from reaching up higher into the corona. At solar maximum, the global dipole is severely weakened. This means that the field lines reach higher into the corona, implying that any null point that occurs will form at a higher radial height, as in the second example. In both of these images it can clearly be see that the separatrix along with the null point lies is not merely a straight line at the height of the null point. This means that the rapid angle change between the magnetic field through the radial plane is the best indication of the location of the separatrix, not the height of the null.

Figures 6.3 and 6.5 show the same quantities plotted for each null point. Graph (a) shows the strength of the normal magnetic field through the radial plane against radial height in the grid square where the null point is located. The dashed line indicates the point where the sign of the magnetic field changes from positive (\hat{n}) to negative ($-\hat{n}$). Graph (b) shows the angle between the magnetic field through the plane and \hat{n} , where the dashed line indicates an angle of 90° , therefore parallel to the surface of the plane and the PIL. In this graph the angle between the magnetic field through the plane and \hat{n}

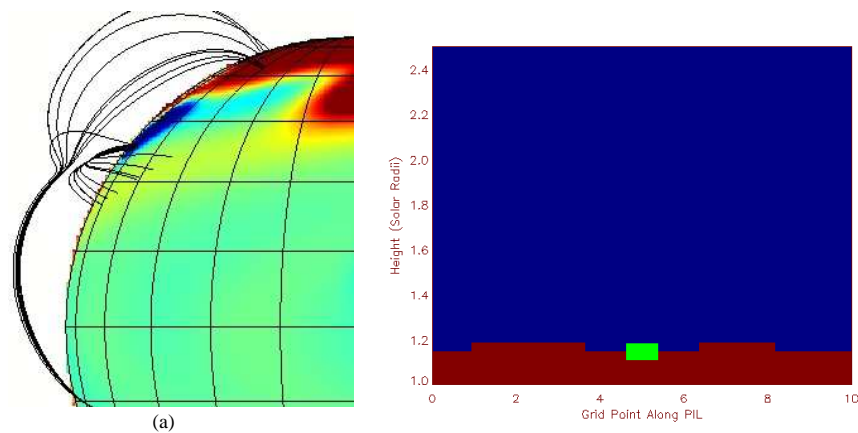


Figure 6.2: Images showing (a) a plot of the field lines directly around the null point and (b) the sign of the projection of the magnetic field through the radial plane taken around a null point occurring at solar minimum. Blue indicates positive field, red indicates negative field, relative to the unit normal vector \hat{n} . The green square in image (b) indicates the position of the null point relative to the extrapolated radial plane.

is measured without regard to the direction of the field. This means that, for example, a 45° angle between the magnetic field and \hat{n} does not tell if the angle is measured in the clockwise or counter clockwise direction. Similarly for angles that exist between 90° and 180° . In the first example, the null point is located at a height of $1.15R_\odot$. Figure 6.3(a) shows that the sign of the field through the plane changes at approximately $1.15R_\odot$, which is around the null point. This illustrates the oppositely orientated field relative to \hat{n} above and below the null. Figure 6.3(b) shows that the angle between the field and \hat{n} becomes greater than 90° around $1.15R_\odot$. This means that the field has become oppositely orientated, and we have passed between the underlying and overlying field. In the second example the null point is located higher up in the corona, at $1.6R_\odot$, as can be seen in the field plot in Figure 6.4(a). Figure 6.5(a) shows that the sign of the field through the plane changes at approximately $1.6R_\odot$, which is around the height of the null point. Figure 6.5(b) indicates that the angle between the field and \hat{n} at the polarity inversion line becomes greater than 90° around $1.6R_\odot$. This means that the field has become oppositely orientated and a null point lies between the two oppositely orientated fields. The slight initial dip in the angle between the field and \hat{n} occurs due to the fact that the magnetic field lines at very low heights, in this case, are not entirely straight, but have a slight angled direction within them caused by interactions with other magnetic flux. This gives a slight angle between the field and \hat{n} until the measurements are taken at sufficient height that the low down magnetic flux has less of an effect.

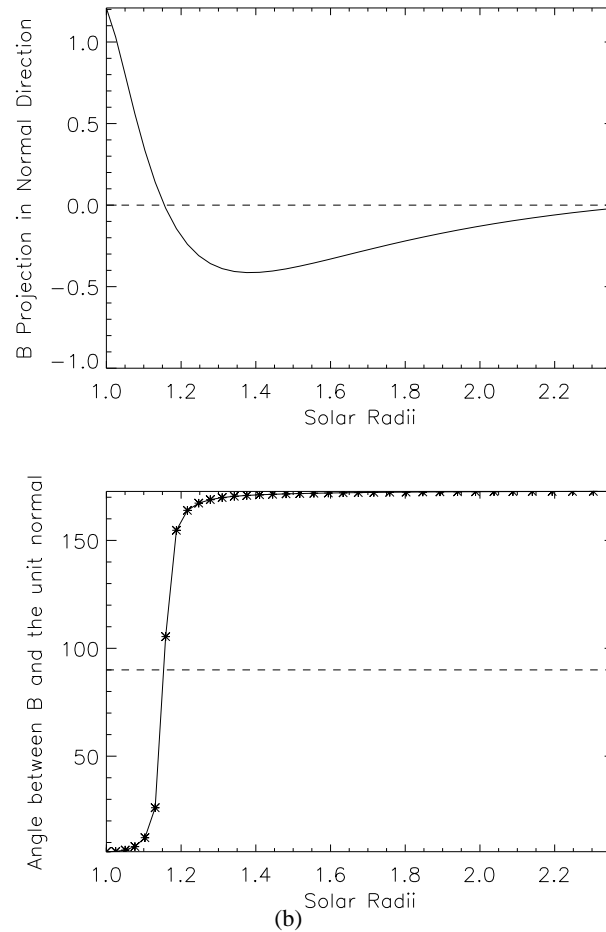


Figure 6.3: Graphs showing (a) strength of \mathbf{B} in the direction of \hat{n} and (b) angle between \mathbf{B} and \hat{n} for a null point located at solar minimum. On graph (a) the dashed line indicates the sign change (and approximate null point location) within the radial plane, and graph (b) the dashed line indicates a 90° angle between \hat{n} and \mathbf{B} , which is the point where the null point is located.

A key feature of both graphs is that as the scanned height within the radial plane increases, the size of the projected field in the direction of B_n decreases. Around the null located at minimum, the absolute strength of the field decreases from approximately 0.86 G at the lowest height, to less than 0.02 G at $2.36 R_\odot$. Around the null located at maximum, the field strength decreases from approximately 7.6 G at the lowest height, to less than 0.01 G at $2.36 R_\odot$. The difference in the size of strength at the lowest height can be explained by the fact that there is significantly more magnetic flux available at solar maximum. These graphs show that as we get higher up in the solar corona, the field is becoming weaker in the normal direction. The weaker magnetic field at higher radial heights suggests that there is a height above which, if a null point were to be located, then flux below would always be greater

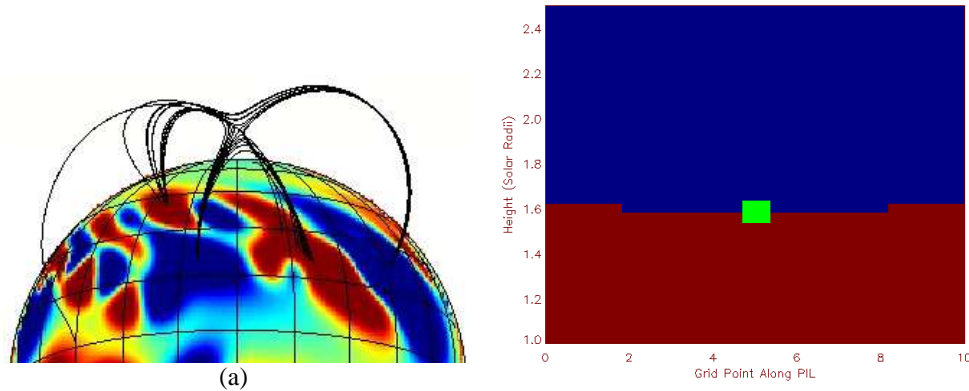


Figure 6.4: Images showing (a) a plot of the field lines directly around the null point and (b) the sign of the projection of the magnetic field through the radial plane taken around a null point occurring at solar maximum. Blue indicates positive field, red indicates negative field, relative to the unit normal vector \hat{n} . The green square in image (b) indicates the position of the null point relative to the extrapolated radial plane.

than flux above and magnetic breakout could always occur.

6.3 Application over two solar cycles

The results of determining the amount of flux above and below the null point are presented in Figures 6.6, 6.7, 6.8 and 6.9. The graphs in Figures 6.6 and 6.7 show the results when the width of the radial plane along the polarity inversion line is taken to be one grid square. The graphs in Figure 6.8 and 6.9 show the results when the radial plane is extended by a width of five grid points either side of the null.

Figures 6.6(a) and 6.8(a) show the fraction of null points that have more flux below them than above, and thus reconnection may remove the flux above allowing the flux below to eject out through the solar corona, versus time and (b) the actual numbers of null points that have more flux below them than above versus time. Graph (c) shows a scatter plot of flux below against flux above the null points, where the lines indicate $10\times$ flux above (dotted), $2\times$ flux above (dashed), flux below equals flux above (solid line), $2\times$ flux below (dash triple dot) and $10\times$ flux below (dot dash). Graph (d) shows a cumulative distribution of the null points, where the solid line indicates the fraction of the total null points that have a ratio of flux below over flux above which is less than the given value on the x axis. The dashed line indicates where flux below equals flux above. During solar minimum,

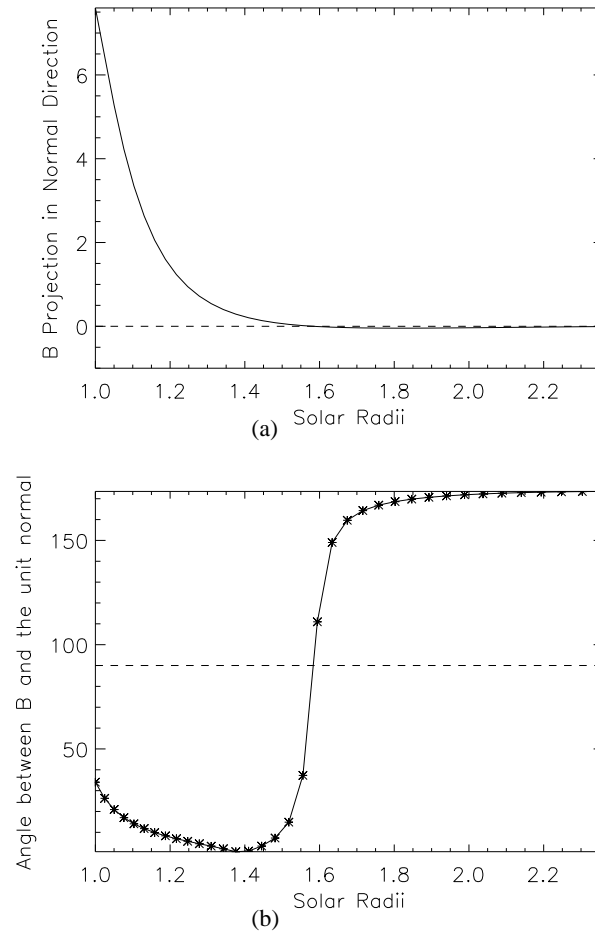


Figure 6.5: Graphs showing (a) strength of the magnetic field in the direction of \hat{n} and (b) angle between \mathbf{B} and \hat{n} for a null point located at solar minimum. On graph (a) the dashed line indicates the sign change (and approximate null point location) within the radial plane, and graph (b) the dashed line indicates a 90° angle between \hat{n} and \mathbf{B} , which is the point where the null point is located.

when the magnetic flux is at its lowest value but the polar field is at its strongest, the fraction of null points that have more flux below than above is very low (approximately 15%-20% when either one grid point or 11 grid points are taken). As the solar cycle progresses to solar maximum, this fraction increases. When only one grid point is used, the fraction of nulls with more flux below than above peaks around 55% to 60%. When 11 grid points are used, this increases slightly to just over 60%. The fraction of nulls with more flux below than above then decreases during the declining phase of the cycle for both sets of data. One key feature of these graphs is that there does not exist a time in either graph where 100% of all of the null points have more flux below than above. This re-enforces the fact that, especially at solar maximum, there is more than just the overlying global dipole restricting

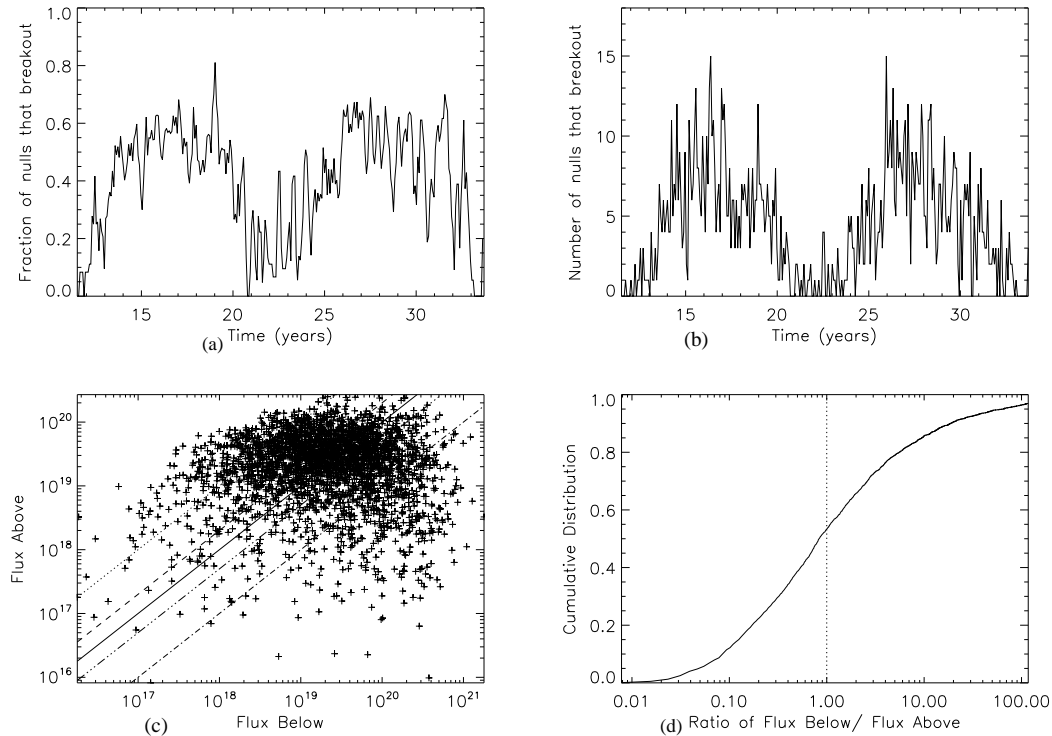


Figure 6.6: Graphs showing results from the flux calculation when only 1 grid point is used, around the coronal null. The graphs show (a) the fraction of null points that have more flux below them than above versus time and (b) the number of null points that have more flux below them than above versus time. Graph (c) shows a scatter plot of flux below against flux above the null points, where the lines indicate $10\times$ flux above (dotted), $2\times$ flux above (dashed), flux below equals flux above (solid line), $2\times$ flux below (dash triple dot) and $10\times$ flux below (dot dash). Graph (d) shows a cumulative distribution of the null points, where the solid line indicates the fraction of the total null points that have a ratio of flux below over flux above which is less than the given value on the x axis. The dashed line indicates where flux below equals flux above.

the underlying magnetic field. Flux from bipoles adding to the complexity of the solar corona must also act as a restrictive mechanism above the coronal null points. Graph (b) shows the number of null points with more flux below than above versus time. As the amount of emerging magnetic flux increases and the strength of the overlying global dipole decreases, more null points exist with higher levels of flux below than above. As the cycle passes through maximum into the declining phase, the amount of flux emergence decreases, but the overlying global dipole strength increases. This implies that not only is there less flux present below the null points at this stage, but also the overlying field from the global dipole is stronger meaning there is more flux above the nulls acting as a restrictive mechanism. The coupling of these two graphs gives a good idea as to the behaviour of the coronal

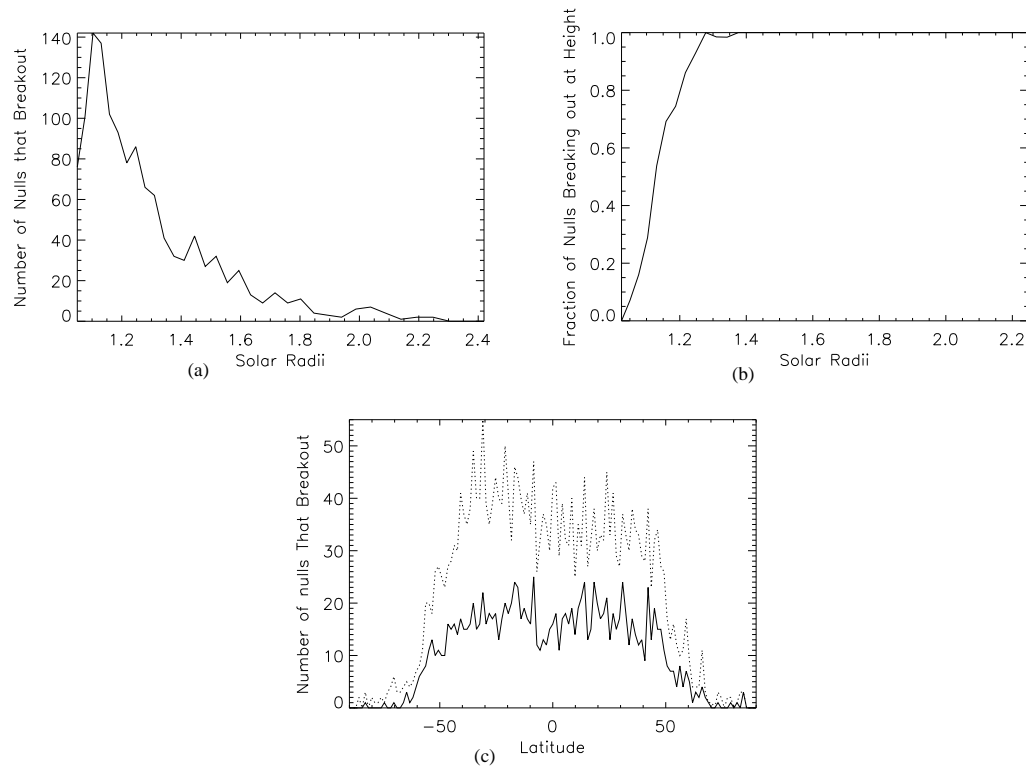


Figure 6.7: Graphs showing results from the flux calculation when only 1 grid point is used, around the coronal null. Graph (a) shows the number of null points that have more flux below them than above against height, (b) shows the fraction of null points that have more flux below them than above at the given radial height and graph (c) shows the number of null points that have more flux below them than above with latitude (solid line). In image (c) the dotted line represents the total number of nulls with latitude plotted over the top.

field and null points throughout the solar cycle.

Graph (c) in each case shows a scatter diagram of the amount of flux above the null point against the amount of flux below the null point, plotted on logarithmic axes. The lines on the graphs indicate the cut off for $10\times$ flux above (dotted), $2\times$ flux above (dashed), flux below equals flux above (solid line), $2\times$ flux below (dash-triple-dot) and $10\times$ flux below (dot-dash). On these graphs, any dot that appears below the solid line indicates a null point that has more flux below than above and hence the underlying magnetic field may eject out into the solar corona. Whereas any dot that appears above the line indicates a null point with more flux above the null than below. Comparing the two graphs shows that scanning the extra grid points either side of the null point increases the eventual amount of flux that is found to lie both above and below the null point by approximately a factor of 10, but in general the shape of the graph maintains its form. Increasing the length of the scan along the PIL by

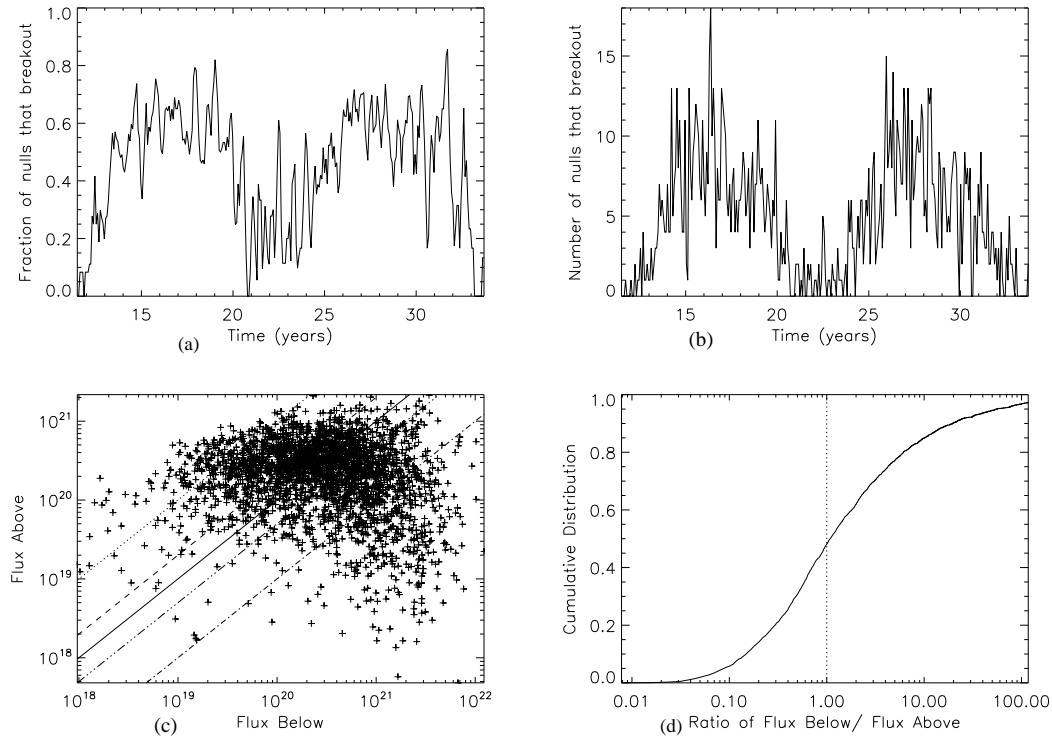


Figure 6.8: Graphs showing results from the flux calculation when the maximum 11 grid point are used along the polarity inversion line. The graphs show (a) the fraction of null points that have more flux below them than above versus time and (b) the number of null points that have more flux below them than above versus time. Graph (c) shows a scatter plot of flux below against flux above the null points, where the lines indicate $10\times$ flux above (dotted), $2\times$ flux above (dashed), flux below equals flux above (solid line), $2\times$ flux below (dash triple dot) and $10\times$ flux below (dot dash). Graph (d) shows a cumulative distribution of the null points, where the solid line indicates the fraction of the total null points that have a ratio of flux below over flux above which is less than the given value on the x axis. The dashed line indicates where flux below equals flux above.

10 grid points only shows an extra 173 null points with more flux below than above over the entire two solar cycles. Therefore we find that this calculation under its simplifying approximation is robust. An interesting feature of these graphs is that while the majority of the null points lie within the region that is between $10\times$ flux above and $10\times$ flux below, there are still null points that have as much as 100 times more flux above or below. These null points are located either extremely low in the solar corona (if there is 100 times as much flux as above), or extremely high in the corona (if there is 100 times as much flux below). These null points occur at key stages during the solar cycle. The incredibly low null points occur around solar minimum, when the overlying global dipole is strongest and restricts

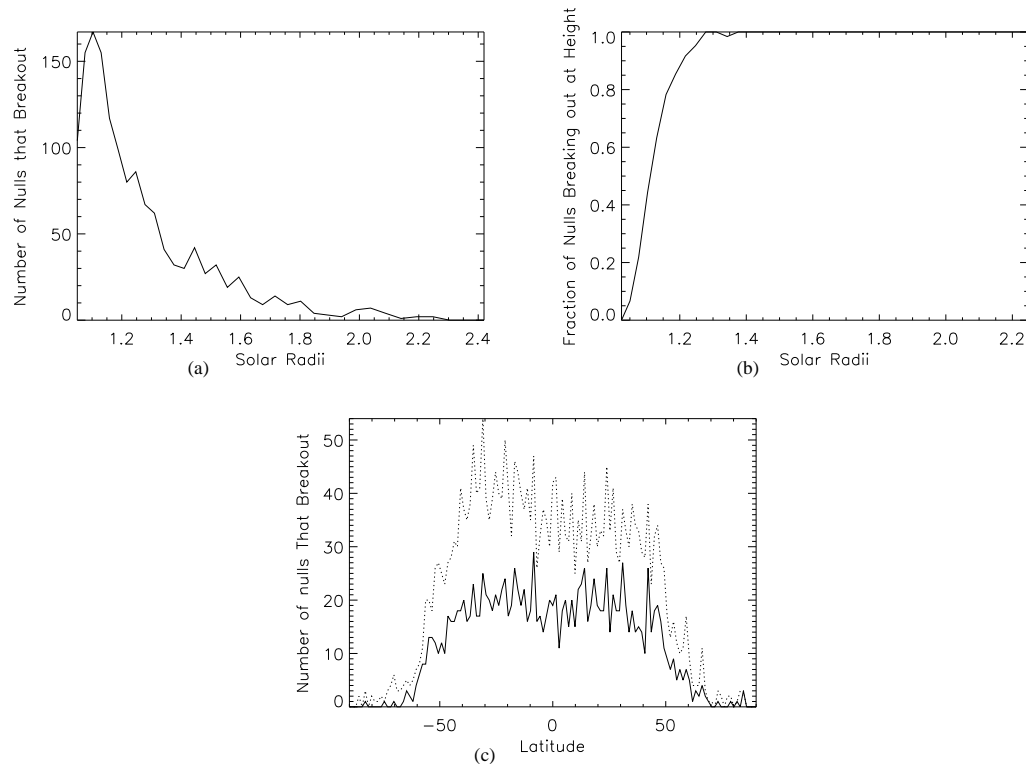


Figure 6.9: Graphs showing results from the flux calculation when the maximum 11 grid points are used along the polarity inversion line. Graph (a) shows the number of null points that have more flux below them than above against height, (b) shows the fraction of null points that have more flux below them than above at the given radial height and graph (c) shows the number of null points that have more flux below them than above with latitude (solid line). In image (c) the dotted line represents the total number of nulls with latitude plotted over the top.

the underlying field from reaching out into the solar corona. The higher null points occur around solar maximum, when the overlying global dipole is weakest, and the underlying flux can reach higher into the solar corona.

Graph (d) shows a cumulative distribution function representing the fraction of null points whose ratio of flux below to flux above is less than the given ratio on the x axis. When the ratio is greater than one, the null has more flux below than above. The dashed line indicates where flux below equals flux above. This graph confirms that approximately 50% of the coronal null points have the required condition that there be more flux below than above the null point, implying that the underlying magnetic field may reconnect at the null and remove the overlying field, allowing ejection to occur. As the amount of flux below the null point increases, the portion of null points that have a ratio of flux below to flux above that is less than the given ratio on the x axis increases. For example, the graph

shows that approximately 60% of the null points would have less than double the flux below to flux above.

Figures 6.7 and 6.9 show graphs indicating various properties of the null points that have been determined to have more flux below than above. Graph (a) in each case shows the number of null points with more flux below than above versus height. This graph shows that as we increase the radial height, the number of null points that have more flux below than above at that height decreases. This graph indicates that the peak height for the number of null points breaking out is approximately $1.1R_{\odot}$. The number of coronal null points with more flux below than above as we increase the height in the corona then decreases. However, comparing this graph with graph (b) enables a much better conclusion to be drawn. Graph (b) shows the fraction of coronal null points that have more flux below than above at each height. This graph shows that above a certain height, all of the coronal null points will have more flux below than above and thus allow the breakout of the underlying magnetic field. For a single grid point or a simulation run with 11 grid points this is approximately $1.35R_{\odot}$. When running simulations with 5, 7 and 9 grid points the average radial height for this to occur is approximately $1.4R_{\odot}$ was discovered. These graphs show that there is a height above which all of the coronal null points have more flux below than above. Conversely, it was also discovered that if the null points occurred at sufficiently low height in the corona then there would always be more flux above than below, approximately $1.02R_{\odot}$. This meant that nulls which occur immediately above the photosphere could not breakout. Thus, comparing graph (b) to graph (a) means we can conclude that, while the number of null points that have more flux below than above decreases with height, the fraction of the total number of nulls found at that height that have more flux below than above is increasing.

Graph (c) shows the number of null points that have more flux below than above versus latitude. The dotted line is a plot of the total number of null points versus latitude. This graph shows that roughly half of the null points at each latitude have more flux below than above. The total number of null points vs latitude roughly sits around 32, while the total number that have more flux below than above is between approximately 13 (1 grid point) and 15 (11 grid points), which shows that roughly half of all the nulls at each latitude satisfy this condition. This also shows that most null points that have more flux below than above are restricted to within the active latitudes of the sun. This implies that not only is the emerging magnetic flux on the solar surface essential for the formation of the coronal null point, but it is also essential in determining whether the coronal null point will have sufficient

flux below it in order to remove the overlying field above the null point and allow the flux below to eject out.

When the number of grid points is changed, the total number of nulls that have more flux below than above remains fairly constant, with little change between them. When only one grid point is considered 1326 null points have more flux below than above (approximately 46.7% of the total null points). However, with five grid points either side only 1449 null points satisfy the condition (approximately 51% of the total null points). Given that the addition of five grid points either side of our null point within the investigation yields an increase of only 173 extra null points with more flux below than above (less than 4%), it can be concluded that approximately 50% of the corona null points located will have more flux below than above. This implies that the breakout model could not account for all of the coronal mass ejections that are seen from the sun, and another model must also be considered to either cause some or all of the ejections.

6.4 Limitations of this Technique

While the previously described technique for calculating the amount of flux above and below the null point can give us a good first estimate, it is prudent to discuss the limitations of such a simple calculation.

Figure 6.10 shows three coronal field configurations which could occur within the simulation wherein the flux calculation code was applied. Figure 6.10(a) shows a setup which is similar to the breakout model of Antiochos (1998). The null point occurs directly above the central section of magnetic flux, and when the radial plane through the PIL below the null point is extrapolated out to $2.5R_{\odot}$, the flux here should be picked up and calculated reasonably. Figure 6.10(b) shows a similar setup, but with a slight difference. The lower latitude bipole is of a much higher strength than the higher latitude bipole, which results in the coronal field extrapolation being non-symmetric about the central region of magnetic flux. The null point which occurs within this region still occurs between the overlying field and the magnetic field within the central region of magnetic flux, but it is situated more to one side, in this case practically above flux between the higher latitude bipole polarities. This means that flux estimated below the null is not of the breakout flux. Figure 6.10 shows another example where

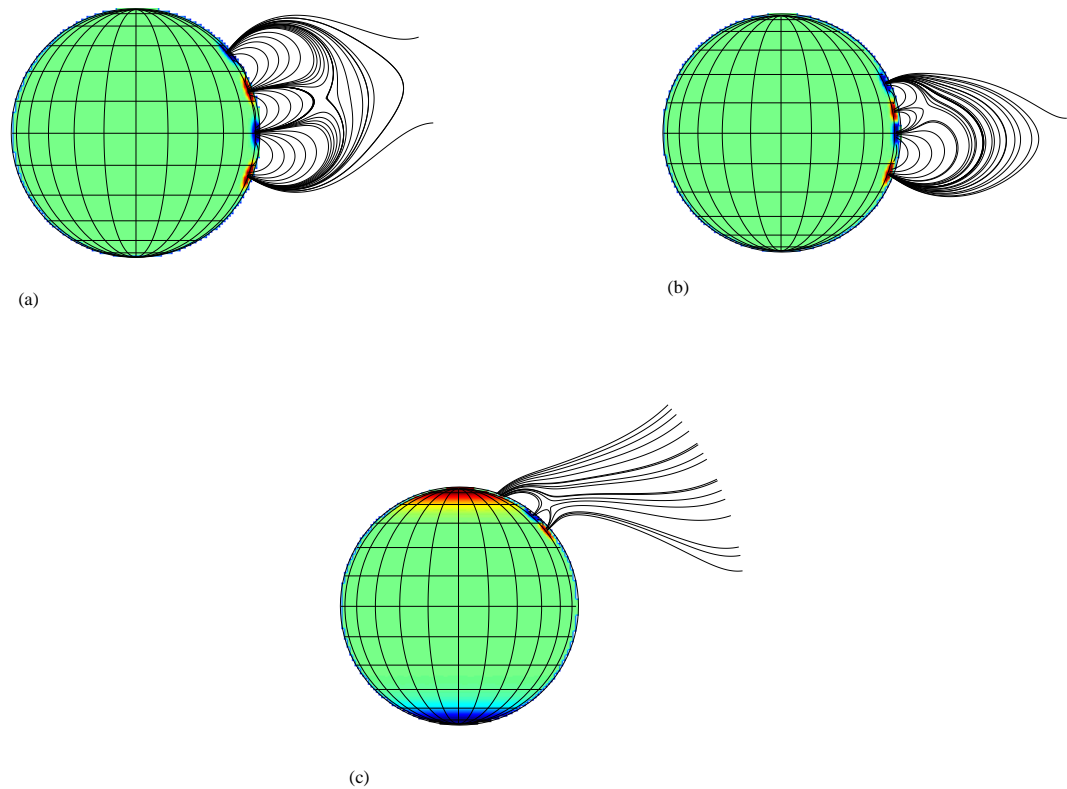


Figure 6.10: Images showing some basic setups and coronal field configurations from examples that could occur within the flux calculation technique: (a) shows our very idealised setup, wherein the idea for our flux calculation technique was derived, (b) shows a setup similar to this, but the lower latitude bipole is stronger than the higher latitude bipole, which results in a non symmetric coronal field extrapolation and (c) shows a coronal field extrapolation when a triple polarity configuration causes a null point to arise.

the plane through which the flux is calculated runs through the wrong region, in this case using a triple polarity photospheric configuration for the coronal field extrapolation. In these cases, there may be some error that comes into effect when calculating the total flux above and below the null point, causing a false identification of whether the null is or isn't likely to breakout. However, we can still be confident that the numbers calculated here are fairly accurate and provide a good first guess at how many of the null points may breakout since only 11.7% of the null points were found to occur in a triple polarity configuration. If all of these were even discounted from the calculation of flux above and below the null point, we would still expect to find that approximately 40-50% of the nulls

would breakout using our current calculation. Another reason we may still be fairly confident with the accuracy of our calculation, is the fact that, regardless of the length of the polarity inversion line which was used when extrapolating our radial plane, between 45% and 55% of the null points were still found to be able to have the sufficient condition to breakout. This still gives us confidence that, while our technique may be improved upon in future studies, it still provides a good first estimate as to the number of null points which may breakout.

One way to improve upon the accuracy of this method is to use not the PIL below the null point, but to calculate the separatrix and magnetic skeleton upon which the null point lies. This could then be used to determine the amount of flux above and below the null point and could improve upon the first guess calculation that has been used here. Recently, Haynes & Parnell (2010) discussed a method which can be used in order to calculate the 3D magnetic skeleton around a coronal null point. This method could be applied to the work described here in order to refine and make it slightly more accurate. The technique could be used to calculate the separatrices, and magnetic skeleton around the located coronal null points. This would then be used to ensure that all of the flux above and below the coronal null point can be accurately calculated and would help to minimize any errors that would occur in configurations similar to the set-ups shown in 6.10(b) and (c).

6.5 Conclusions

In this section, the variation of coronal null points that have a necessary but not sufficient condition to allow the underlying field to breakout have been investigated.

The amount of flux above and below the coronal null point is investigated by extrapolating a radial plane out to $2.5R_{\odot}$. The width of this plane along the polarity inversion line is then varied from 1 grid point wide to 11 grid points wide. The projection of the magnetic field through the plane in the direction of the normal, $\hat{n} = \frac{-\nabla B}{|-\nabla B|}$, is then calculated at all heights of the radial plane. Using the direction of the magnetic field projection, the shape of the separatrix is calculated and used as the defining boundary when calculating the magnetic flux through the radial plane. The magnetic flux below the calculated separatrix height is summed up as the flux below the null point, the flux above the height is summed as flux above the null. Should the amount of flux below the null point be

greater than the amount of flux above the null, then that null point is determined to have a necessary condition to enable the flux below the null to reconnect and breakout. If shearing was to occur and force reconnection to occur at the null point there would be sufficient magnetic flux below the null to completely remove the overlying magnetic field, allowing the ejection of the underlying flux. If the amount of flux above the null point is greater then reconnection would not allow the overlying field to be completely removed. This would result in the continued restriction of the underlying magnetic flux and possibly a failed eruption. In this case, another CME initiation mechanism would have to account for any ejection that would take place.

Using the results of the graphs in Figures 6.6, 6.7, 6.8 and 6.9, conclusions as to the variation of coronal null points that may possibly allow breakout and hence the overall usefulness of the breakout model in predicting the probability of a coronal mass ejection can be made. The main cause of any breakout at a null point that would occur is dependent upon the emerging magnetic field on the solar surface. While the overlying global dipole, which originates within the polar field, acts as a restrictive mechanism in allowing the underlying magnetic flux to reach higher into the corona, during stages of weak polar field, there are still null points that do not have more flux below than above. This implies that the overlying global dipole is not the only factor restricting the underlying magnetic field from ejecting out into the solar corona. Magnetic flux originating within the emerging magnetic bipolar active regions must add sufficient complexity to the overlying magnetic field that it aids in providing a restriction to the underlying magnetic flux. This would explain why, during solar maximum, the underlying magnetic field is still relatively restricted in radial height, but also why there exists coronal null points around solar maximum that don't have more flux below than above. The removal of the polar flux and hence overlying global dipole does not necessarily mean that the magnetic flux at higher radial heights will be completely removed. However, despite the underlying flux contributing to the complexity of the overlying magnetic field, there is still a height above which all of the coronal null points will have more flux below than above. Above approximately $1.4R_{\odot}$, all of the coronal null points should have more flux below than above. This means that while the underlying flux will still contribute to the overlying coronal magnetic field, the overlying field will be so weak that it will be unable to restrict the underlying magnetic flux from breaking out.

A further conclusion arises from the number of null points that have been determined to have more flux below than above. It has been shown that approximately half of the total coronal null points have

more flux below than above, meaning approximately 1420 null points over the two solar cycles (i.e. roughly 710 null points per cycle). It is known that during solar minimum coronal mass ejections occur every day or so, while at maximum this number increases to roughly 5-6 ejections per day (see Figure 1.3 for plots of CME numbers with latitude and time). Comparing this rate of CMEs with the variation of the coronal null points that have been located implies that the breakout model cannot possibly account for all of the coronal mass ejections that take place on the sun. The model could only account for a portion of the total number of CMEs and another model or combination of models must also account for the initiation of a portion of the coronal mass ejections.

We then discussed how the technique used here, while still providing a good first estimate to the number of coronal null points that could possibly breakout, could be improved upon and built up in order to further ensure accuracy within our prediction of the number of coronal null points that could possibly breakout. The method of Haynes & Parnell (2010) was noted as being useful in order to ensure that the complexity of the coronal magnetic field is taken into account when calculating the flux above and below the null point. This method could be applied within our code in order to determine the location of the separatrix surfaces within the coronal configurations around the null point, and these could then be used in order to accurately measure the amount of magnetic flux above and below the null point. This would improve our estimate provided by the technique discussed here and allow us to further our understanding of the amount of magnetic flux above and below the null points, especially those in much more complex coronal configurations.

Application of Magnetic Flux Transport Simulation to Rapidly Rotating Stellar Bodies

In previous chapters, the time evolution of the radial magnetic field at the level of the solar photosphere has been simulated using a magnetic flux transport model. In this Chapter it is theorized that the same equation and code can be used to model the time evolution of the radial magnetic field of rapidly rotating stellar bodies. To consider this, Equation 2.12, which specifies how to evolve forward the radial component of the magnetic field by evolving forward the individual mode amplitudes with time, will be used with an enhanced profile for both the meridional circulation and differential rotation. In doing so we carry out a speculative study to determine whether or not the code is valid and whether the numerical scheme applied still works in more extreme stellar situations. This study is done to deduce whether the numerical code could be applied to these stellar situations, however, we could also take this study further. This would involve taking a vast amount of observations in order to try to determine possible emergence rates, field strengths etc. and using these to accurately model the surface field of the star and its evolution with time.

In the work of Marsden et al. (2007), Zeeman Doppler Imaging was used to reconstruct the photospheric magnetic field of HD171488. Marsden et al. (2007) then extrapolated a coronal configuration of the stellar body using a potential field extrapolation technique which used the stellar surface to extrapolate the coronal configuration out to the source surface radius. HD171488 is a 30 Myr old, rapidly rotating, early G-Dwarf star, in the rapid braking-phase of its life cycle, just prior to becoming

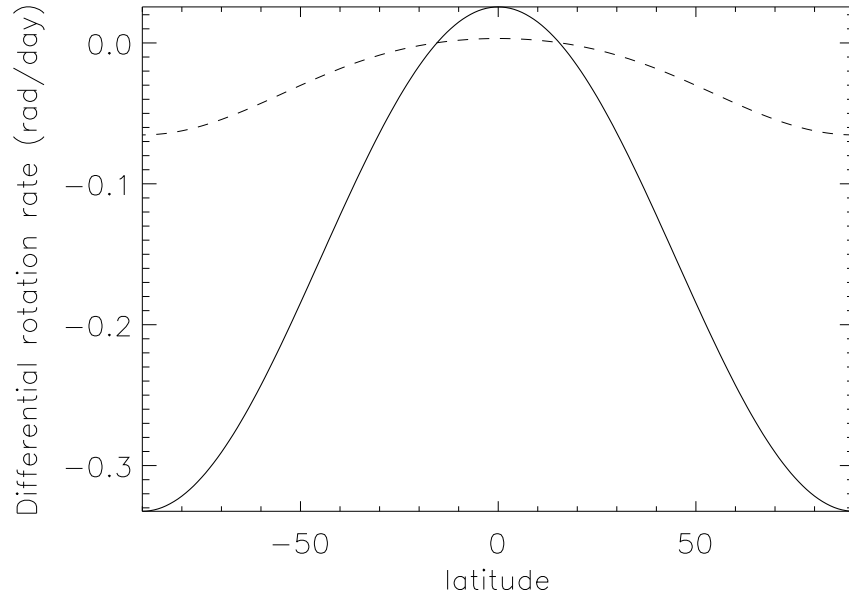


Figure 7.1: Plot of solar differential rotation (dashed line) and the enhanced stellar differential rotation of HD171488 (solid line). A calculated carrington rotation rate for each line has been applied and subtracted in order that the radial surface field does not move within the given frame of reference.

a zero age main sequence star. It has a Lithium abundance that is approximately 140 times that of the sun and the application of a solar like differential rotation law within the imaging process allowed the measurement of the stars differential rotation from observed brightness features, which was found to be approximately 20 times that of the sun. The enhanced differential rotation rate ($\Omega(l)$), at latitude l , was calculated to be:

$$\Omega(l) = \Omega_{eq} - d\Omega \sin^2 l, \quad (7.1)$$

where $\Omega_{eq} = 4.786 \pm 0.013$ rad/day is the equatorial rotation rate and $d\Omega = 0.402 \pm 0.044$ rad/day represents the difference between the equator and the poles. The value of $d\Omega$ was seen to be much higher than previously predicted and over twice that of other early-G dwarf stars.

Figure 7.1 shows a plot of the calculated enhanced differential rotation profile (solid curve) on top of the solar differential rotation profile (dashed line). Here, an inferred carrington rotation rate of $\Omega_{car} = 4.38943$ rad/day for this star has been subtracted from Equation 7.1 in a similar manner as

in previous simulations. The magnitude of the enhanced differential rotation is much larger than that of the solar differential rotation, and depending upon the latitude can be just over six times larger. The enhanced differential rotation acts on a timescale of approximately 0.04 years, compared with the solar timescale of 0.25 years. This indicates that the enhanced differential rotation acts much faster at shearing the magnetic field than solar differential rotation, and using this enhanced differential rotation will produce a stiff test of the numerical scheme. In the test case where the solar value of meridional circulation is used along with the enhanced differential rotation profile, the field will be sheared much faster in an east-west direction than when using the solar differential rotation. This raises the question as to what value of meridional circulation will need to be used in order to minimise this east-west shearing and allow reproduction of photospheric field configurations of a similar orientation to those observed on the stellar body.

In this Chapter, the radial magnetic field simulation is adapted in order to model faster rotating stellar surface fields. The enhanced differential rotation rate is implemented and a new peak value of meridional circulation is calculated such that the evolution of the radial magnetic field remains accurate and similar to that from HD171488. This is done by matching the orientation of the Polarity Inversion Lines (P.I.L.) with respect to the north-south line to similar orientations calculated from HD171488 observations. This will be done using several simulations where five bipoles will be emerged and evolved using the enhanced differential rotation and different peak values of meridional circulation in order to determine the best value of meridional circulation to be used. Multiple bipole simulations will then be run using the new peak values of meridional circulation coupled with the enhanced differential rotation in order to see if we can produce simulations which give field configurations where the orientation of the PILs within the multiple bipole simulations approximately match the orientation of the PILs calculated within the observed radial surface field of HD171488. This will allow fairly accurate evolution of the surface magnetic field in line with the expected variation from observations.

7.1 Initial Steps

Figure 7.2 shows results taken when the observed map from HD171488 is evolved forward using the enhanced differential rotation rate along with solar meridional flow. There is no emergence within this simulation as we are merely looking at the orientation of the magnetic field at this stage. Figures

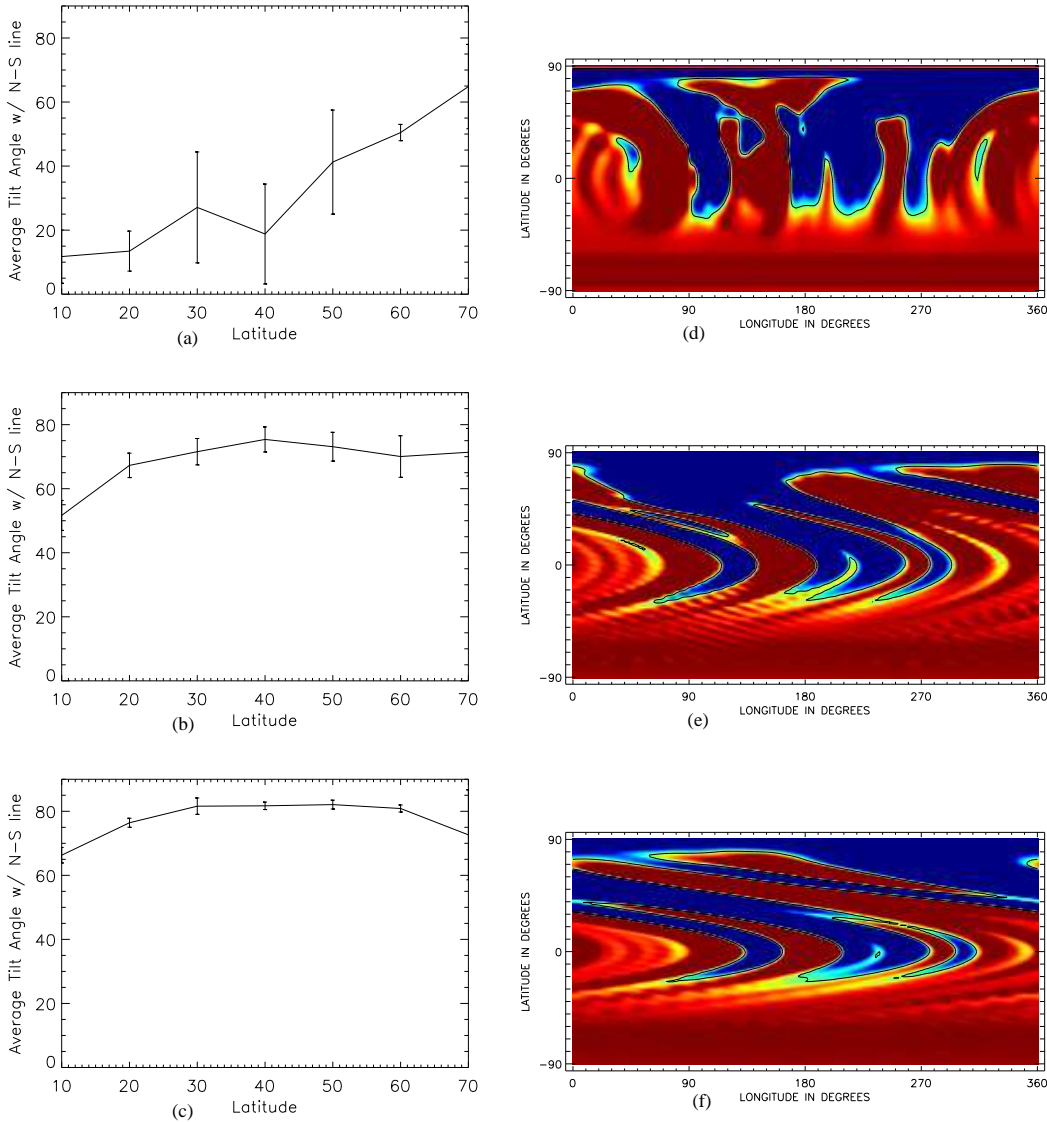


Figure 7.2: Plots showing the average bipole tilt angle versus latitude when the observed map from HD171488 is evolved forward for (a) 0 days, (b) 10 days and (c) 20 days using solar meridional circulation rates. In each graph the error bars represent the distribution of tilt angles at each latitude. The images on the right show the radial surface distribution at (d) day 0, (e) day 10 and (f) day 20, all plotted for a saturation level of 10 Gauss. The Polarity inversion lines are given by the black lines.

(a), (b) and (c) show the average polarity inversion line tilt angle with respect to the north-south line, versus latitude, while Figures (d), (e) and (f) show the radial surface field distribution at (d) day 0, (e) day 10 and (f) day 20 of the simulation. The day 0 image is the observed magnetogram taken from HD171488 using Zeeman Doppler Imaging. The error bars show the distribution of tilt angles

around the calculated mean at each latitude. These figures show that, when using the solar meridional circulation the average tilt angle of the radial magnetic surface field increases drastically throughout all latitudes, after only 20 days.

Figure 7.2(a) shows that in the observed magnetogram at lower latitudes the tilt angle is fairly low (approximately between 10° - 25°). Above 50° latitude the average tilt angle is slightly higher, ranging between 40° and 65° . Figure 7.2(b) shows the calculated tilt angle after only 10 days of evolution, while Figure 7.2(c) shows the same calculation after 20 days. Figures 7.2(e) and (f) show the radial surface distribution at day 10 and 20 respectively. These graphs show that after only a short period of evolution the average tilt angle versus latitude increases sharply throughout the simulation to between 65° and 80° at all latitudes. The distribution of tilt angles at each latitude, indicated by the error bars plotted along the graphs, decreases throughout the evolution due to the shearing effect of the differential rotation. Combining the faster differential rotation with a slow rate of meridional circulation causes a shearing of the field in a east-west direction, which increases the tilt angle of all polarity inversion lines with respect to the north-south line.

The observed radial surface distribution shown in Figure 7.2(d) shows a single snapshot of what has been a continuous evolution of the stars magnetic field. In this plot the flux regions are mainly north-south orientated with small tilt angles. However, only 10-20 days of evolution with enhanced differential rotation combined with a solar style meridional circulation completely changes this. Assuming that Figure 7.2(d) gives a characteristic profile for the magnetic field we ask the question; “What change in the other transport parameters are required to insure that the tilt angles at all latitudes remain similar to those found in the initial observed map, but at later times of evolution?” One possibility is that to model the time evolution of the radial magnetic field of faster rotating stars, then the peak value of meridional circulation should be altered such that the change in tilt angle fits the observations better. In the next Section, several runs are done in order to determine the value of meridional circulation that should be used in order to allow a reproduction of the observed tilt angles at later times. It should be noted that in this we are not trying to reproduce the exact B_r distribution of HD171488, but rather only the tilt angle variation with latitude. Multiple bipole simulations are then run in Section 7.3 where numerous bipoles, which are created and emerged randomly, are emerged over a 60 day period using the enhanced differential rotation profile, coupled with newly calculated peak rate for meridional circulation.

7.2 Several Emerged Bipoles

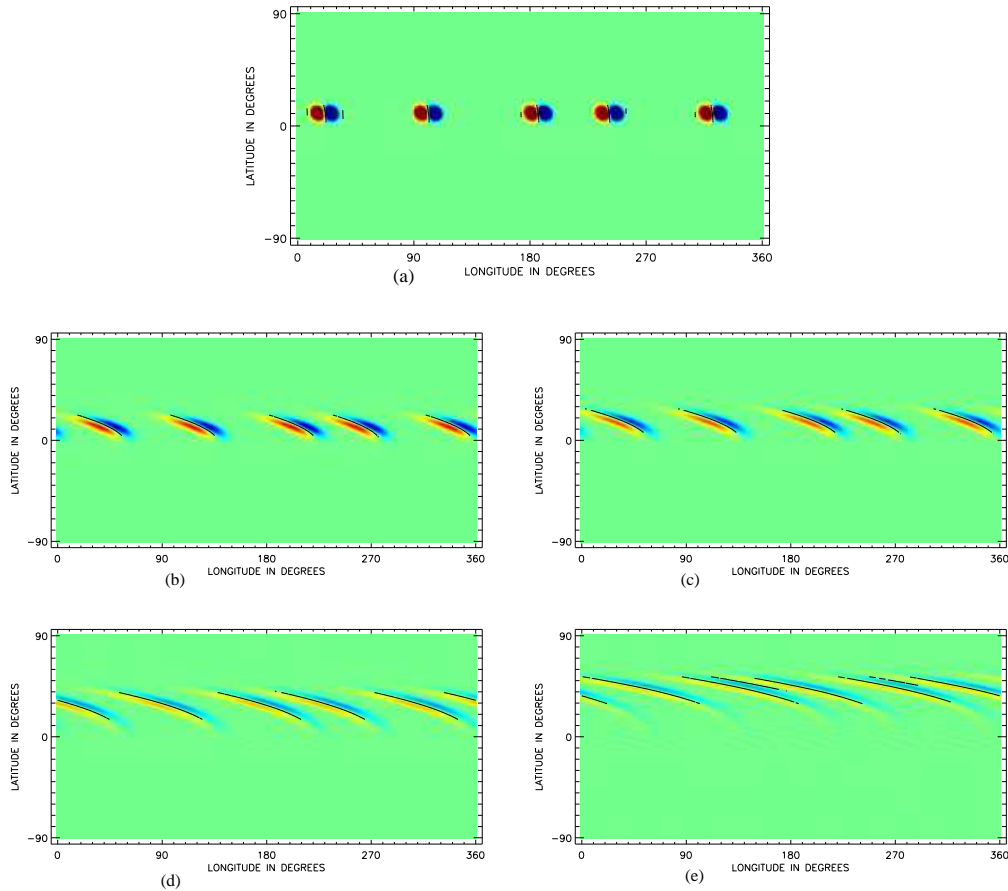


Figure 7.3: Radial surface field images taken when 5 bipoles with an initial tilt angle of 0° are emerged at 10° latitude, and then evolved forward for 20 days. Image (a) shows the radial surface field distribution at day 0, while images (b), (c), (d) and (e) show the radial field distribution at day 20 for a different peak value of meridional circulation. Image (b) shows when a peak value of 50 m s^{-1} is used, (c) shows when a peak value of 100 m s^{-1} is used, (d) shows when a peak value of 200 m s^{-1} is used and (e) shows when a peak value of 300 m s^{-1} is used. All images are produced for a saturation level of 10 Gauss. Similar images can be produced when the bipoles are initially emerged at different latitudes and when the initial tilt angle of the bipoles is set to 30° .

In order to determine the most suitable peak value of meridional circulation that should be used, a set of simulations are run. In these simulations five bipoles are emerged at the same latitude, ranging from 10° and 70° . They are then evolved forward for 20 days using the enhanced differential rotation rate and a new peak value for meridional circulation, which ranges from 11 m s^{-1} to 300 m s^{-1} . The average tilt angle of the bipoles is then recorded and plotted against the initial latitude of emergence

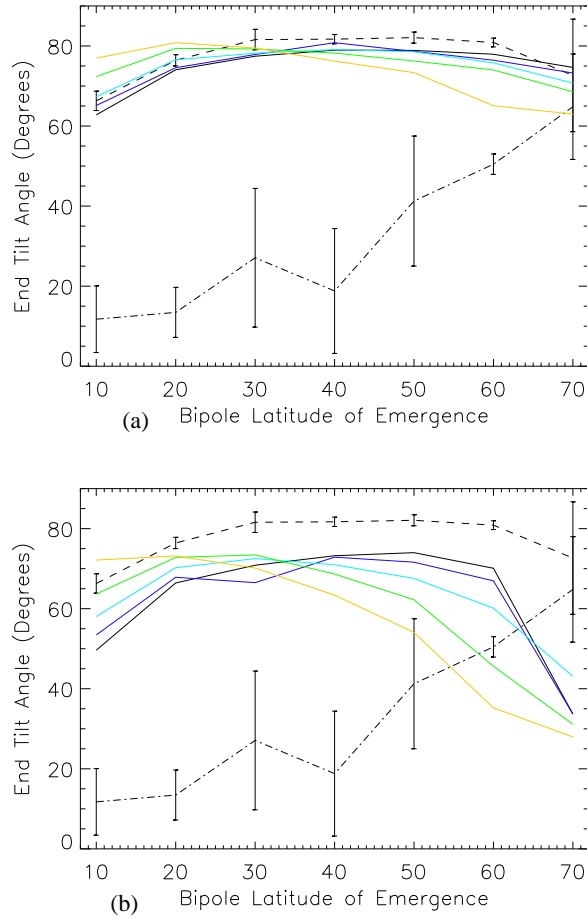


Figure 7.4: Plots showing the average tilt angle after 20 days of five bipoles with the same latitude of emergence, when the initial tilt angle is (a) 0° or (b) 30° . The resulting tilt angle after 20 days is plotted against the initial latitude of emergence of the bipoles. In both graphs the dot-dashed line indicates the average tilt angle versus latitude of the observed map from HD171488, the dashed line indicates the average tilt angle after the observed map has been evolved for 20 days with enhanced differential rotation and solar meridional circulation. Each solid coloured line indicates a different peak value of meridional circulation used to evolve the 5 bipoles. Black indicates a peak value of 11 m s^{-1} , blue shows 50 m s^{-1} , turquoise represents a peak value of 100 m s^{-1} , green represents 200 m s^{-1} and yellow has a peak value of 300 m s^{-1} . The bars on the two lines indicating data from the observed runs show the standard deviation within the observed data set.

of the five bipoles. This is done for a range of emergence latitudes in order to give an idea as to how the tilt angle changes depending upon the initial latitude of emergence of the bipoles. This will highlight any possible connection between latitude of emergence and the tilt angle of the bipoles as the surface flow have an effect upon the bipoles. Using these simulations will hopefully allow us to determine the best peak value of meridional circulation to be used along with the enhanced

differential rotation rate. In the first set of simulations all five bipoles have an initial tilt angle of 0° with respect to the North-South line, and a second set is run where the initial tilt angle is 30° . This also allows us to determine how the initial tilt angle of the bipole can also affect the evolution of the field orientation when the new profile for differential rotation is used, coupled with different peak values of meridional circulation. We hope to be able to use the calculated value of meridional circulation in order to run multiple bipole simulations which can accurately recreate the magnetic field orientations of the observed field on HD171488.

Figure 7.3 shows radial surface field images taken when five bipoles with an initial tilt angle of 0° are emerged at 10° latitude and evolved forward for 20 days. Image (a) shows the initial radial field distribution, while the other images show the radial surface distribution after 20 days when a different peak value of meridional circulation is used. Image (b) shows a peak value of 50 m s^{-1} , (c) 100 m s^{-1} , (d) 200 m s^{-1} and (e) 300 m s^{-1} . Similar images can be produced when the bipoles are initially emerged at a different latitude (ranging from 20° - 70°) or have an initial tilt angle of 30° . These show that after 20 days evolution the tilt angle of the bipoles has increased greatly, while the bipoles themselves have barely moved with respect to latitude.

The plots in Figure 7.4 show the average tilt angle of five bipoles after 20 days evolution plotted against the initial latitude of emergence of the bipoles, using the enhanced differential rotation and different rates of enhanced meridional circulation. Figure 7.4(a) shows the results when the five bipoles have an initial tilt angle of 0° , while Figure 7.4(b) shows the results when an initial tilt angle of 30° is applied to the bipoles. On each graph the solid coloured lines represent a different peak value of meridional circulation: black indicates a peak value of 11 m s^{-1} , blue indicates 50 m s^{-1} , turquoise indicates 100 m s^{-1} , green 200 m s^{-1} and yellow 300 m s^{-1} . The black dash-dot line indicates the values calculated from the observed map which are trying to be matched. These graphs show that when the peak value of meridional circulation is kept within the previously used range of 11 m s^{-1} to 300 m s^{-1} then the simulations do not match the observed values. The meridional circulation is too weak to counter the shearing in an east-west direction by the differential rotation. This results in a large final tilt angle for the bipoles. These runs suggest that a much higher peak value of meridional circulation is needed. When the initial tilt angle is changed to 30° , similar results are found (see Figure 7.4(b)).

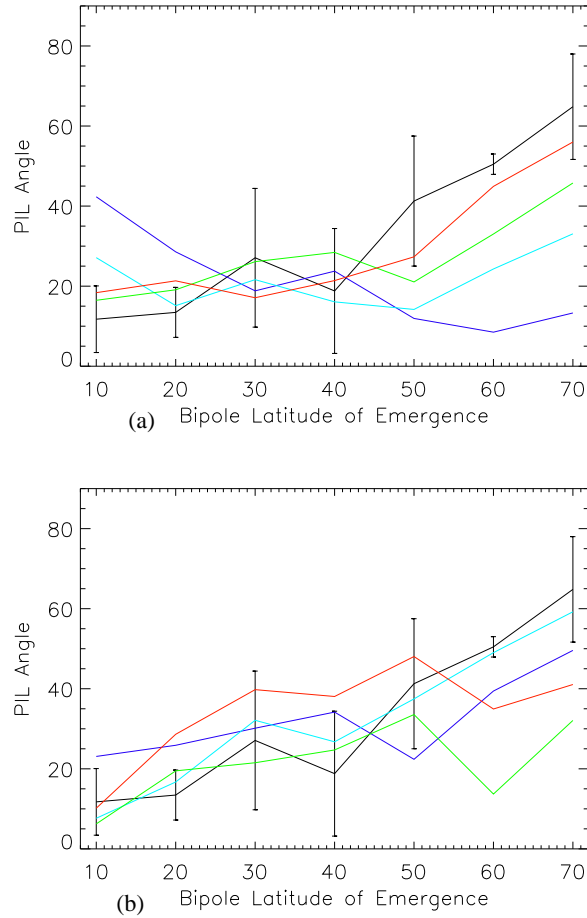


Figure 7.5: Plots showing the average tilt angle after 20 days of five bipoles with the same latitude of emergence, when the initial tilt angle is (a) 0° or (b) 30° . The average tilt angle after 20 days is plotted against the initial latitude of emergence of the bipoles. In both graphs the solid black line, with bars showing variation, indicates the average tilt angle versus latitude of the observed map from HD171488, while each solid coloured line indicates a different peak value of meridional circulation. Dark blue indicates a peak value of 1100 m s^{-1} , turquoise represents a peak value of 1200 m s^{-1} , green represents 1300 m s^{-1} and red has a peak value of 1400 m s^{-1} .

Figure 7.5 shows the results when the same set of simulations are run, but the peak value of meridional circulation is varied between 1100 m s^{-1} and 1400 m s^{-1} . Figure 7.5(a) shows when the bipoles have an initial tilt angle of 0° , while Figure 7.5(b) shows when the bipoles have an initial tilt angle of 30° . In the images the black solid line indicates the results from the observed map (the bars indicate the distribution of tilt angles at each latitude), while each of the coloured lines indicates a different peak value of meridional circulation: dark blue indicates a peak value of 1100 m s^{-1} , turquoise shows 1200 m s^{-1} , green a peak value of 1300 m s^{-1} and red shows 1400 m s^{-1} . With the increase in meridional

circulation, the timescale of meridional flow is between 0.016 and 0.02 years. This is now just under half the timescale of the differential rotation. These graphs show a much better match in average tilt angles versus latitude to the expected variation from the observed map.

Figure 7.5(a) shows that, when an initial tilt angle of 0° is chosen, each of the peak rates of meridional circulation between 1100 ms^{-1} and 1400 ms^{-1} show an acceptable match to the observed PIL tilt angles after 20 days. While there is a good match in tilt angle when the bipoles are emerged at 10° latitude, peak rates of 1100 ms^{-1} and 1200 ms^{-1} give a slightly larger tilt angle. Above approximately 50° , a peak rate of 1400 ms^{-1} shows the best match of the calculated tilt angles from the observed map. Figure 7.5(b) shows that when an initial tilt angle of 30° is used all of the peak rates of meridional circulation again show an acceptable match with the calculated tilt angle from the observations. However, above 50° a peak value of 1200 ms^{-1} gives the most accurate match in tilt angles. These graphs suggest that a peak value of either 1200 ms^{-1} or 1400 ms^{-1} would be the best peak value of meridional circulation to use when modeling the evolution of the magnetic field on HD171488. In the next Section, two separate sets of simulations are run for 60 days. The first uses a peak value of 1200 ms^{-1} for meridional circulation, the second uses a peak value of 1400 ms^{-1} . This covers the full range of the higher rates of meridional circulation that match well.

7.3 Multiple Bipole Emergence Runs

Using the enhanced values of meridional circulation (specifically 1200 ms^{-1} and 1400 ms^{-1}), two simulations are run where multiple bipoles are emerged, and evolved forward for 60 days. Each simulation is run using a different peak value of meridional circulation, but the same pattern of bipole emergence. 200 bipoles are emerged, with the tilt angle chosen randomly between $\pm 50^\circ$ and emergence latitude and longitude of the bipoles is also chosen at random, but the latitude of emergence is kept between $\pm 40^\circ$, giving a good spread of bipole emergence latitudes. These characteristics are chosen to keep in line with the bipoles that can be used to model solar simulations. However, all of the bipoles are randomly created such that no bias towards any one bipole type, shape, size, tilt or emergence latitude is used. In both simulations, the average tilt angle of the PIL in the surface distributions versus latitude is calculated at various time steps and compared to the average tilt angle versus latitude calculated from the observed map (Figure 7.2 (a)). This is the key feature being

matched between these simulations and will indicate whether the radial surface transport code has been successfully adapted in order to model the faster rotating stellar body. Note that in doing this we are only comparing tilt angles of the P.I.L. and not the radial field distributions, nor are we calculating the locations of coronal null points. This is merely a theoretical simulation done in order to ensure that the numerical code may be modified in order to model these faster rotating stellar bodies. To compare radial field distributions, accurate information regarding the emergence of flux would be required, which is not available to us. A further point of note is that, due to the much higher value of meridional circulation being used, there is a very small numerical error within the code when using the spherical harmonics. This error is minimized by taking a smaller time step, where 10000 time steps are used in order to represent a single day, and also a larger diffusion rate of $1400 \text{ km}^2\text{s}^{-1}$ which allows accurate modeling of the magnetic field. This error does not significantly affect the large scale evolution and variation of the magnetic field. In order to stabilize the numerical scheme the diffusion is only doubled while the meridional flow is over a factor of 100 times larger. Such a modest increase in diffusion shows the code has performed well.

7.3.1 Meridional Circulation Peak Value: 1200 ms^{-1}

Figure 7.6 shows the results when a peak value of 1200 ms^{-1} is used for meridional circulation. The plots on the left show the average tilt angle versus latitude after (a) 8 days, (b) 31 days and (c) 60 days, while the respective radial surface field distributions are shown in images (d) 8 days, (e) 31 days and (f) 60 days. In images (a), (b) and (c) the red line shows the average tilt angle versus latitude in the simulation, while the black line shows the calculated average tilt angle versus latitude from the observed map. The error bars denote the standard deviation in the tilt angles. These plots show a relatively good match of tilt angles at lower latitudes. However, above approximately 40° latitude the simulation is not as well matched to the observed data and there is an increase in the average tilt angle within the simulated data. This is due to the rapid fall off in meridional circulation, coupled with a high gradient in the differential rotation, which shears the magnetic flux more in an east-west direction and results in a slightly higher end tilt angle.

To counter this east-west shearing a broader profile of meridional circulation, $u_w(\lambda)$, is used. This produces a larger value of meridional circulation at higher latitudes. The same peak value and peak

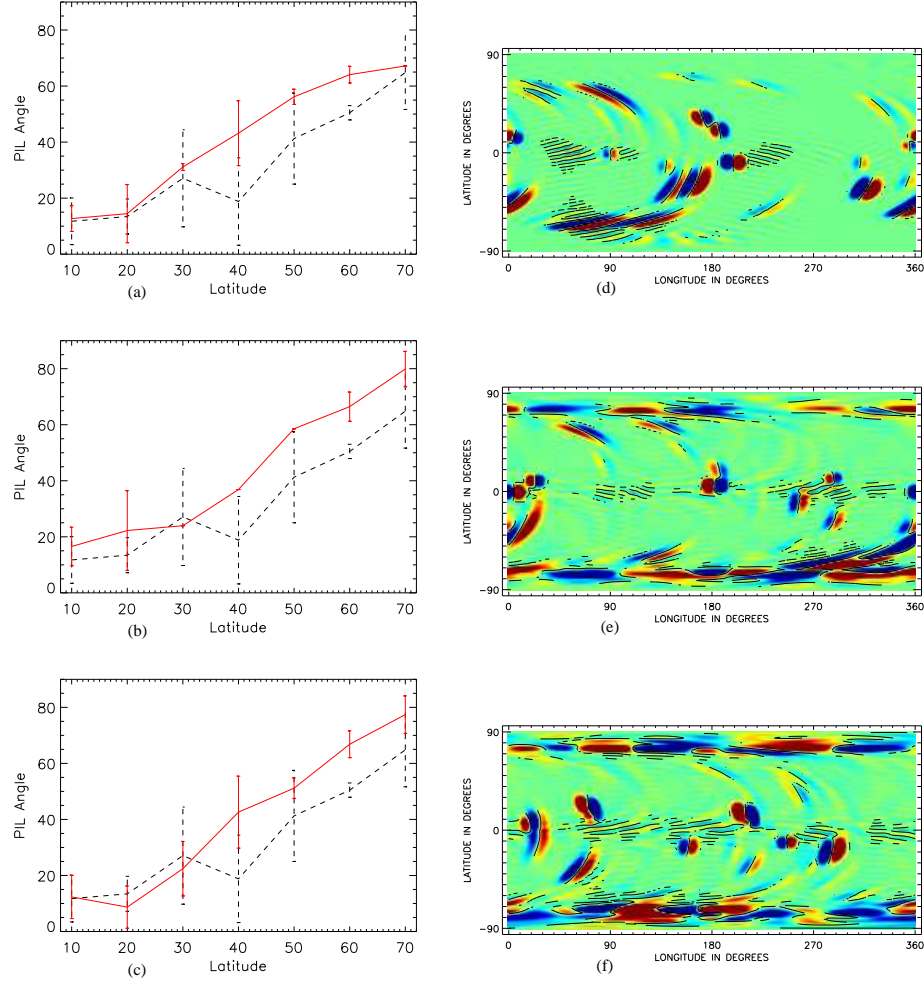


Figure 7.6: Plots showing the average tilt angle versus latitude at various time-steps within the simulation where bipoles are emerged in both hemispheres, where meridional circulation has a peak value of 1200 ms^{-1} . Plot (a) is taken from day 8, (b) is taken from day 31 and (c) is taken from day 60. Images (d), (e) and (f) show the corresponding radial surface field distributions plotted for a saturation level of 50 Gauss. The black lines are polarity inversion lines plotted on the surface.

latitude will be used within this profile and the new profile will merely allow a higher rate of meridional circulation at higher latitudes. The profile is taken to be:

$$u_w(\lambda) = 1350 \left(\sin \left(\frac{\pi \lambda}{\lambda_0} \right) + \left(\frac{1}{9} \right) \sin \left(\frac{3\pi \lambda}{\lambda_0} \right) \right), \quad (7.2)$$

where $u_w(\lambda)$ indicates the value of meridional circulation at latitude λ . The parameter λ_0 is the latitude where the effect of meridional circulation disappears and is taken to be $\lambda_0 = \pm 75^\circ$ as in the solar case. this is done merely to keep inline with the parameters that have been used in the

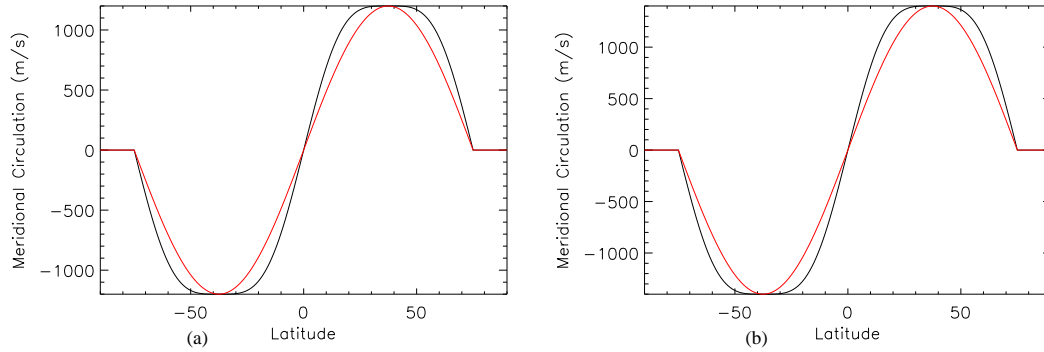


Figure 7.7: Plots of the wider profile of meridional circulation implemented (black line) with the original profile plotted for comparison (red line). Plot (a) shows when the peak value is taken to be 1200 m s^{-1} , while plot (b) shows when the peak value is taken to be 1400 m s^{-1} .

previous solar simulations. Figure 7.7(a) shows a plot of the wider used meridional flow profile (black line), compared with the previous meridional circulation profile (red line). The profile is wider around maximum, and falls off more rapidly above 60° latitude. This should maintain the effect of meridional circulation at higher latitudes and lower the resulting tilt angle of the P.I.L.

The plots and images in Figure 7.8 show the results when the same set of bipoles are emerged, but the wider meridional circulation profile is coupled with the enhanced differential rotation rate. It is clear that the average tilt angle versus latitude calculated within these simulations shows a better match to the calculated variation within the observed map than when a thinner profile of meridional circulation is used. The error bars indicate that the simulated data has slightly more deviation at very few latitudes within the simulated data. However, this can be explained due to the initial tilt angle of the bipoles being chosen at random and having a wide spread between approximately $\pm 45^\circ$.

7.3.2 Meridional Circulation Peak Value: 1400 m s^{-1}

The images in Figure 7.9 show the results when the peak value of meridional circulation is set to 1400 m s^{-1} using the original profile of meridional circulation. The bipole emergence patterns are the same as in the previous set of simulations. Images (a), (b) and (c) show the average tilt angle of the polarity inversion lines versus latitude on day 8, 31 and 60 respectively, while images (d), (e) and (f) show the corresponding radial surface field images. In images (a), (b) and (c) the red line indicates the

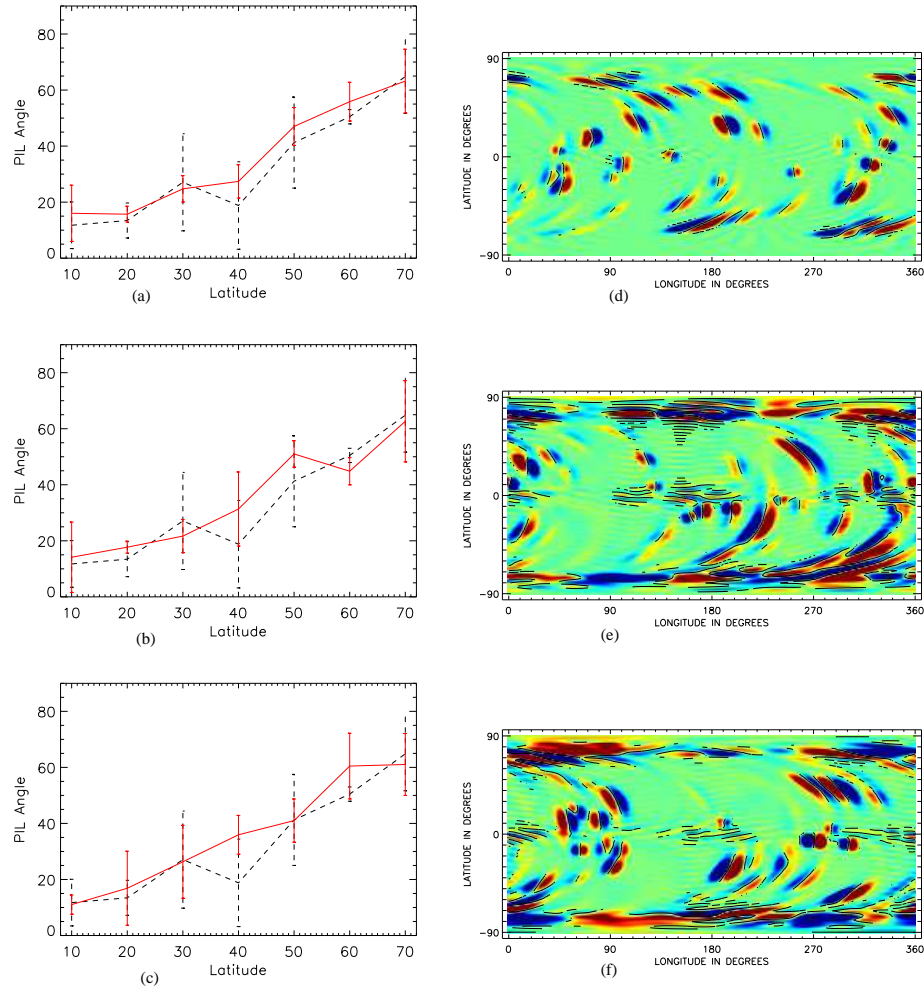


Figure 7.8: Plots showing the average tilt angle versus latitude at various time-steps within the simulation. Bipoles are emerged in both hemispheres and the wider profile of meridional circulation with a peak value of 1200 m.s^{-1} is applied. Plot (a) is taken from day 8, (b) is taken from day 31 and (c) is taken from day 60. Images (d), (e) and (f) show the corresponding radial surface field distributions plotted for a saturation level of 50 Gauss. The black lines are polarity inversion lines plotted on the surface.

calculated variation from the radial surface map, while the black line indicates the calculated variation versus latitude for the observed map.

A variation similar to that found when using a peak value of 1200 m.s^{-1} can be seen. The red curve matches fairly well to the observed map at lower latitudes. However, above 40° there is a slightly larger difference. This difference is smaller compared to when a peak value of 1200 m.s^{-1} is used. However, the difference between this data set and the observed map is still significant at higher latitudes.

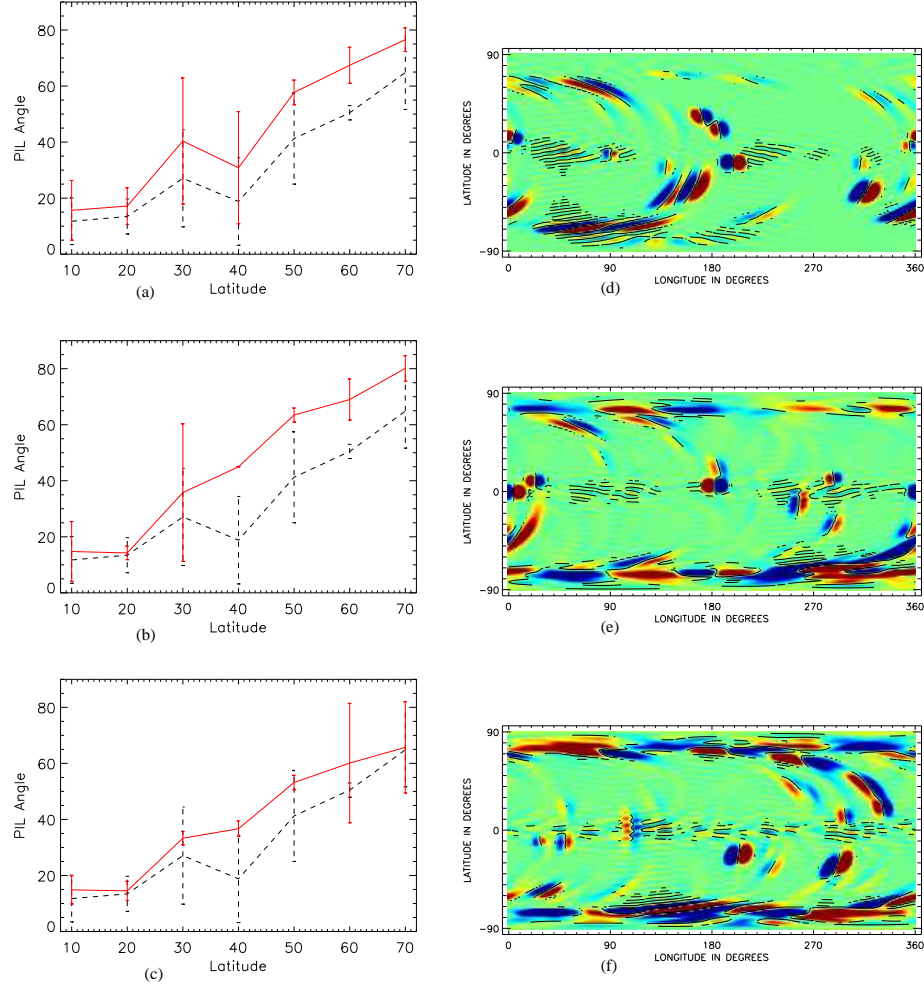


Figure 7.9: Plots showing the average tilt angle versus latitude at various time-steps within the simulation where bipoles are emerged in both hemispheres using the original profile of meridional circulation with a peak value of 1400 m s^{-1} . Plot (a) is taken from day 8, (b) is taken from day 31 and (c) is taken from day 60. Images (d), (e) and (f) show the corresponding radial surface field distributions plotted for a saturation level of 50 Gauss. The black lines are polarity inversion lines plotted on the surface.

A further simulation using a slightly wider meridional circulation profile, modified such that the peak value occurs at 1400 m s^{-1} is run. The chosen profile is:

$$u_w(\lambda) = 1575 \left(\sin \left(\frac{\pi \lambda}{\lambda_0} \right) + \left(\frac{1}{9} \right) \sin \left(\frac{3\pi \lambda}{\lambda_0} \right) \right). \quad (7.3)$$

and is given by the black line in Figure 7.7(b). This profile ensures that the meridional circulation remains stronger around its peak value and falls off faster at the higher latitudes maintaining the effect

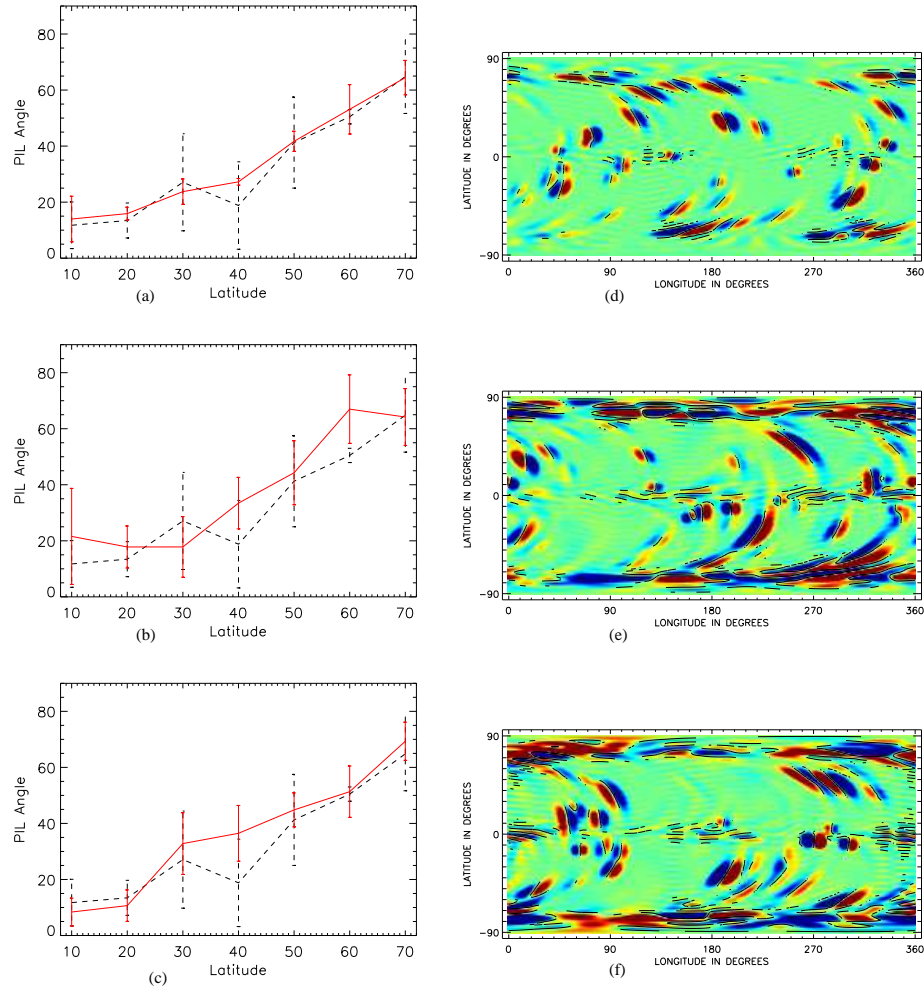


Figure 7.10: Plots showing the average tilt angle versus latitude at various time-steps within the simulation where 400 bipoles are emerged in both hemispheres using the wider profile of meridional circulation with a peak value of 1400 ms^{-1} . Plot (a) is taken from day 8, (b) is taken from day 31 and (c) is taken from day 60. Images (d), (e) and (f) show the corresponding radial surface field distributions plotted for a saturation level of 50 Gauss. The black lines are polarity inversion lines plotted on the surface.

of meridional circulation throughout the active latitudes.

The plots and images in Figure 7.10 show the results when bipoles are emerged using the wider meridional circulation profile from Equation 7.3, coupled with the enhanced differential rotation rate. It can be seen that the average tilt angle versus latitude when using this profile of meridional circulation gives a much better match to the observed orientation of the magnetic field at all latitudes. The difference between the orientation of the magnetic field polarity inversion lines throughout all stages of the simulation give an excellent match to that calculated from the observed magnetogram. This

gives confidence that the code has been modified correctly in order to accurately apply the simulation to faster rotating stellar magnetic fields.

7.4 Results

In this chapter, the radial surface transport code has been modified such that the evolution of magnetic flux on faster rotating stellar bodies, specifically HD171488, can be modeled. This is done through a combination of enhanced differential rotation and an increase and change in the profile for the meridional circulation. This was a speculative study to consider the feasibility of such application in the future.

It was found that a much higher peak value of meridional circulation of approximately 1200-1400 m_s^{-1} must be applied in order to accurately replicate the polarity inversion line orientations calculated from observations of HD171488. This range of peak values, coupled with the original profile of meridional circulation, gives a good match when only five bipoles are used. However, when 400 bipoles are emerged over the course of 60 days, the average tilt angle at higher latitudes (i.e. between 40° and 70° latitude) is slightly higher than the observed variation. In order to combat this, a slightly wider meridional circulation profile is applied (Equations 7.2 and 7.3). This allows a stronger value of meridional circulation at higher latitudes and decreases the eventual tilt angle of the bipoles throughout this region by countering the effect of differential rotation. It is found that using the wider profile of meridional circulation with a peak value of 1400 m_s^{-1} (which is approximately 127 times that of the known meridional circulation on the sun) gives the best match of tilt angle versus latitude to the observed data. This allows the conclusion that the combination of higher peak rate of meridional circulation, wider meridional flow profile and emergence rates has reproduced the observed surface field orientation calculated from HD171488.

While this work produces field orientations that are similar to those observed on the surface magnetic field of HD171488, we cannot say that the field strengths have been accurately reproduced. One reason for this does arise from the limitations that the observations of the star itself have: we merely have limited observations of the surface magnetic field in the northern hemisphere of the star, which arise from the limitations from the imager itself. If we had fully accurate measurements at all latitudes

of the star we could possibly determine emergence patterns for the star and use these, coupled with the adapted numerical code from this section, in order to produce fully accurate simulations which match not only field orientations, but also field strengths.

Conclusions and Future Work

8.1 Conclusions

In this thesis, a magnetic flux transport simulation coupled with a potential field extrapolation technique have been used in order to determine the variation of coronal null points throughout the solar cycle and their dependence upon the overlying global dipole and underlying magnetic flux. This is used as an indication for the applicability of the breakout model (see Antiochos (1998); Antiochos et al. (1999); MacNeice et al. (2004); Lynch et al. (2004); Choe et al. (2005)) as a mechanism for the initiation of a coronal mass ejection. Following from this the magnetic flux transport code is then applied, in a purely speculative study, in order to determine if the numerical scheme within the code allows it to be applied to faster rotating stellar bodies. This is done via the inclusion of a faster differential rotation rate described by Marsden et al. (2007), and a higher peak value and wider profile of meridional circulation.

Chapter 1 gave a description of CMEs and the various mechanisms for the initiation of a CME. Key to the work presented here is the magnetic breakout model (Antiochos, 1998; Antiochos et al., 1999; MacNeice et al., 2004; Lynch et al., 2004; Choe et al., 2005). In the breakout model, a null point plays a key role in the eruption of magnetic flux from the sun by allowing reconnection to occur that removes the overlying coronal field. For simplicity, it is therefore assumed that the variation of coronal null points will indicate the possible variation of breakout configurations.

In Chapter 2, the Magnetic Flux Transport simulation is described. This simulation describes the time evolution of the radial field component of the magnetic field on the solar surface. Two forms of the simulations are described: the instant day simulation, which produces an approximation of the Sun's global magnetic field at any instant in the simulation and the simulated synoptic magnetograms, created using the instant day maps, which are used as a direct comparison with Kitt Peak magnetograms.

Chapter 3 described the Potential Field Source Surface (PFSS) Model. Here, a potential coronal field is extrapolated out to $2.5R_{\odot}$, using each of the previously calculated radial surface magnetic fields as a base boundary condition. A description of the null point finding technique of Haynes & Parnell (2007) is then given. This technique will be applied to each coronal configuration calculated throughout the simulations in order to determine the location of coronal null points throughout the solar cycle. Several simple test configurations are analysed where a coronal null point is known to exist in order to test the accuracy of the null finding technique.

In Chapter 4, the codes described in the previous two chapters were brought together in order to create the main simulation. The null finding code was applied to each coronal field in both the instant day and simulated synoptic magnetogram simulations and the variation of coronal null points deduced. Both the instant day and simulated synoptic magnetogram simulations show that the number of coronal nulls varies cyclically throughout the simulation and in phase with the emergence rate of new flux. Over 2 simulated cycles a total of 2843 coronal nulls were found for the instant day simulations and 2437 for the simulated synoptic magnetograms. Therefore through the process of forming synoptic magnetograms approximately $1/6$ of the nulls are lost. At cycle maximum in the instant day simulations the number of null points peaks at around 15 – 17 per day. When the number of nulls are compared to the the rate of bipole emergence, a wide scatter is observed; however, on average, the ratio of nulls to emerged bipoles is approximately $1/3$. As the emerging flux follows the well known butterfly diagram the location of coronal nulls follows a similar pattern. There is however a difference in the structure of the butterfly diagram for the nulls as it shows a polar drift in the rising phase of the solar cycle. Therefore, active cycles should therefore have many more coronal null points and breakout configurations than inactive ones.

On studying the latitudes of formation of the nulls it is found that the vast majority of nulls form

within the active latitude belts of $\pm 50^\circ$, with only very few forming outside this range. This indicates that it is the complex underlying active region fields that are key in forming the coronal nulls and not the interaction of single bipoles with the global dipole. This is supported by the result that only 8% of the total number of nulls within the instant day simulation found were connected to the global dipole. As the vast majority of nulls are not connected to the global dipole there is no significant change in the number of nulls between the rising and declining phases; therefore, the breakout configurations occur throughout the solar cycle. The hypothesis presented in Chapter 3 and Figure 3.1 is found to be true for nulls connected to the global dipole, however, their numbers are not significant.

As the majority of the coronal nulls are found to form at active latitudes, due to the complex structure of the underlying photospheric fields, a consequence of this is that the nulls form low down in the corona. An average radial extent of $1.25 R_\odot$ (174,000km) is found in both simulations. In addition the number of nulls falls off as approximately $1/r^3$ as predicted by Longcope et al. (2003). When the null points within the instant day simulations are classified depending upon the photospheric flux distribution leading to their creation, it is found that 71% form in quadrupolar flux distributions (either newly emerged quadrupoles – 46%, or advected quadrupoles – 25%), 18% form around the equator due to cross hemisphere bipole interactions while only 11% are due to the interaction of single bipoles with unipolar regions of flux such as those of the polar fields.

A key result of this study shows that the majority of null points (over 90%) do not connect to the global dipole and therefore there is no significant variation in the abundance of breakout configurations between the rising and declining phases of the solar cycle (other than that related to just asymmetry in sunspot numbers). The lack of dependence of the majority of the null points upon the global dipole is one of our key conclusions. As a consequence, in principle, the Magnetic Breakout Model remains equally applicable at all stages of the solar cycle as an initiation mechanism for coronal mass ejections.

In Chapter 5, the locations of the calculated null points were used in order to quantify how many of the coronal configurations may, in principle, breakout. This is done to further determine the applicability throughout the solar cycle. Here, we assume that a null point may breakout if all of the overlying magnetic flux can be removed via reconnection with the underlying magnetic flux at the null point. In essence, if there is more flux below the null than above, then the underlying field may breakout.

A simple calculation is applied to each of the null points. The path of the PIL lying below each null point is followed and a radial projection out to $2.5R_{\odot}$ made. This produces a radial plane along the PIL containing the null point. The unit normal vector at each grid cell along the PIL is then calculated using $\hat{n} = \frac{-\nabla B_r}{|\nabla B_r|}$. This is then used to determine the direction of the field passing through the plane and to determine the flux below compared to flux above.

Through applying this technique, approximately half of the null points were found to have the required condition for breakout to occur. The number of null points that are found to breakout follows the variation of emerging magnetic flux on the solar surface. As the amount of emerging magnetic flux increases, the number of null points that can breakout increases. However, although the number of configurations that can breakout increases with the amount of magnetic flux present, there is never a point throughout the solar cycle where all of the nulls present at a single time allow breakout. It can also be seen that above $1.4R_{\odot}$ all of the null points should breakout, regardless of what stage at the solar cycle they occur. These results show that, while the breakout model may account for approximately half of coronal mass ejections that occur, a further model or set of models would be required to fully explain the initiation of all coronal mass ejections.

Chapter 6 compared the results of the coronal null point variation calculated within the instant day and simulated synoptic data is to the variation calculated when the observed data from Kitt Peak was used as a base boundary condition for potential field extrapolation. This comparison should allowed us to determine if the calculated variation in the simulated data is realistic, as the general characteristics of coronal null point variation should be very similar in both sets of simulations. It is found that both sets of simulations produce results that are consistent with one another and have similar overall characteristics for the variation of coronal null points on the large scale. This gives confidence that the overall variation of coronal null points throughout the solar cycle has been accurately calculated.

In the final chapter of this thesis, the radial surface transport code has been adapted in order to model the time evolution of rapidly rotating stellar bodies. This is done via the application of an enhanced differential rotation rate, calculated by Marsden et al. (2007) (see Equation 7.1), combined with an enhanced meridional circulation. This purely speculative study is done in order to test if the numerical scheme can be applied to the problem of rapidly rotating stars.

The code is modified such that the orientation of polarity inversion lines of bipoles which are emerged

approximately matches the observed orientation from HD171488. This is done by combining an increased meridional circulation peak rate of between 1200 m s^{-1} and 1400 m s^{-1} and applying a wider profile of meridional circulation. The value of diffusion is also increased, however, this is done in order to preserve the numerical stability within the code.

Running multiple bipole simulations with the enhanced differential rotation rate, combined with the profile of meridional circulation, gives a tilt angle versus latitude variation that approximately matches the observed map from HD171488. It is discovered that a peak rate of meridional circulation taken to be 1400 m s^{-1} , combined with a slightly wider profile of meridional circulation (given in Equation 7.3) gives the best match in tilt angle versus latitude distribution. This shows that, in theory, the code could be adapted in order to model faster rotating stellar bodies using a combination of enhanced differential rotation and a faster and wider meridional circulation profile.

8.2 Future Work

The work presented in this thesis could be continued in several ways.

- The potential field extrapolation technique could be modified such that a linear or non linear force free coronal field is extrapolated. This would give slightly more complexity to the coronal field distribution, however, it is hoped that the general variation of coronal null points within the more complex field would be similar to the calculated variation here.
- The recently developed technique for finding magnetic skeletons and separators of Haynes & Parnell (2010) could be applied in order to develop our first guess technique for calculating the magnetic flux above and below the null point. This technique could be used to accurately account for all of the flux above and below the null point and would be able to refine our initial conclusion.
- Given that the numerical code has been modified to work for rapidly rotating stellar bodies, it can be further applied. This can be via further observations of HD171488, which can be used to determine possible emergence rates on this stellar body. This can then be used within the code in order to approximate flux levels and model the flux evolution on the surface. A further application is to the study of other rapidly rotating stellar bodies and deduce a wider range of transport coefficients.

Bibliography

- Aulanier, G., Pariat, E., & Démoulin, P. 2005, *A&A*, 444, 961
- Andrews, M. D. 2003, *Sol. Phys.*, 218, 261
- Antiochos, S. K. 1998, *ApJ*, 502, L181
- Antiochos, S. K., DeVore, C. R., & Klimchuk, J. A. 1999, *ApJ*, 510, 485
- Archontis, V., Moreno-Insertis, F., Galsgaard, K., Hood, A., & O'Shea, E. 2004, *A&A*, 426, 1047
- Barnes, G. 2007, *ApJ*, 670, L53
- Baumann, I., Schmitt, D., & Schüssler, M. 2006, *A&A*, 446, 307
- Berthoud, M. 2001, Diploma Thesis (<http://www.scss.tcd.ie/Stephen.Farrell/ipn/background/alpsat/main.html>)
- Beveridge, C., Priest, E. R., & Brown, D. S. 2002, *Sol. Phys.*, 209, 333
- Beveridge, C., Priest, E. R., & Brown, D. S. 2004, *Geophysical and Astrophysical Fluid Dynamics*, 98, 429
- Brown, D. S., & Priest, E. R. 2001, *A&A*, 367, 339
- Brown, D. S., & Priest, E. R. 1999, *Royal Society of London Proceedings Series A*, 455, 3931
- Chen, J. 1989, *ApJ*, 338, 453
- Chen, J. 1996, *J. Geophys. Res.*, 101, 27499
- Chertok, I. 1997, *ASP Conference Series*, 111, 369
- Choe, G. S., Cheng, C. Z., Lee, J., Lynch, B. J., Antiochos, S. K., DeVore, C. R., & Zurbuchen, T. H. 2005, *AGU Spring Meeting Abstracts*, 2
- Cremades, H., Bothmer, V., & Tripathi, D. 2006, *Advances in Space Research*, 38, 461
- Cremades, H., & St. Cyr, O. C. 2007, *Advances in Space Research*, 40, 1042
- Démoulin, P., Priest, E. R., & Lonie, D. P. 1996, *J. Geophys. Res.*, 101, 7631

- Démoulin, P. 2005, *Chromospheric and Coronal Magnetic Fields*, 596,
- Démoulin, P. 2006, *Advances in Space Research*, 37, 1269
- Forbes, T. G., & Priest, E. R. 1995, *ApJ*, 446, 377
- Galsgaard, K., Titov, V. S., & Neukirch, T. 2003, *ApJ*, 595, 506
- Harvey, K. L., & Zwaan, C. 1993, *Sol. Phys.*, 148, 85
- Haynes, A. L., & Parnell, C. E. 2007, *Physics of Plasmas*, 14, 082107
- Haynes, A. L., Parnell, C. E., Galsgaard, K., & Priest, E. R. 2007, *Royal Society of London Proceedings Series A*, 463, 1097
- Haynes, A. L., & Parnell, C. E. 2010, *Physics of Plasmas*, 17, 092903
- Henney, C. J., & Harvey, J. W. 2001, *AGU Spring Meeting Abstracts*, 51
- Hornig, G., & Priest, E. 2003, *Physics of Plasmas*, 10, 2712
- Howard, T. A., Nandy, D., & Koepke, A. C. 2008, *Journal of Geophysical Research (Space Physics)*, 113, 1104
- Jackson, J. D. 1962, *Classical Electrodynamics*, New York: Wiley, 1962,
- Klimchuk, J. A. 2001, *Space Weather (Geophysical Monograph 125)*, ed. P. Song, H. Singer, G. Siscoe (Washington: Am. Geophys. Un.), 143 (2001), 125, 143
- Kusano, K., Maeshiro, T., Yokoyama, T., & Sakurai, T. 2004, *ApJ*, 610, 537
- Lin, J., Soon, W., & Baliunas, S. L. 2003, *New Astronomy Review*, 47, 53
- Longcope, D. W., Brown, D. S., & Priest, E. R. 2003, *Physics of Plasmas*, 10, 3321
- Longcope, D. W., & Beveridge, C. 2007, *ApJ*, 669, 621
- Longcope, D. W., & Parnell, C. E. 2009, *Sol. Phys.*, 254, 51
- Lynch, B. J., Antiochos, S. K., Devore, C. R., & Zurbuchen, T. H. 2004, *AGU Fall Meeting Abstracts*, 400
- Mackay, D. H., Gaizauskas, V., & van Ballegoijen, A. A. 2000, *ApJ*, 544, 1122

- Mackay, D. H., Priest, E. R., & Lockwood, M. 2002, *Sol. Phys.*, 207, 291
- Mackay, D. H. & Lockwood, M. 2002, *Sol. Phys.*, 209, 287
- Maclean, R., Beveridge, C., Longcope, D., Brown, D. S., & Priest, E. R. 2005, *Royal Society of London Proceedings Series A*, 461, 2099
- Maclean, R. C., Hornig, G., Priest, E. R. & Beveridge, C., 2006, *Sol. Phys.*, 235, 280
- Maclean, R. C., Beveridge, C., & Priest, E. R. 2006, *Sol. Phys.*, 238, 13
- Maclean, R. C., & Priest, E. R. 2007, *Sol. Phys.*, 243, 171
- MacNeice, P., Antiochos, S. K., Phillips, A., Spicer, D. S., DeVore, C. R., & Olson, K. 2004, *ApJ*, 614, 1028
- Marsden, S.C., Jardine, M., Dontai, J.-F., Petit, P., Semel, M. & Carter, B.D. 2007, *Memorie S.A. Italiana*, 79, 307
- Martin, S. F. 1998, *Sol. Phys.*, 182, 107
- Murray, M. J., Hood, A. W., Moreno-Insertis, F., Galsgaard, K., & Archontis, V. 2006, *A&A*, 460, 909
- Murray, M. J., & Hood, A. W. 2007, *A&A*, 470, 709
- Nandy, D., & Choudhuri, A. R. 2001, *ApJ*, 551, 576
- Pariat, E., Aulanier, G., & Démoulin, P. 2006, *SF2A-2006: Semaine de l'Astrophysique Française*, 559
- Parnell, C. E., Smith, J. M., Neukirch, T., & Priest, E. R. 1996, *Physics of Plasmas*, 3, 759
- Parnell, C. E., Neukirch, T., Smith, J. M., & Priest, E. R. 1997, *Geophysical and Astrophysical Fluid Dynamics*, 84, 245
- Parnell, C. E., & Galsgaard, K. 2004, *A&A*, 428, 595
- Parnell, C. E., Haynes, A. L., & Galsgaard, K. 2008, *ApJ*, 675, 1656
- Phillips, K. J. H. 2002, *Vistas in Astronomy*, 34, 353

- Pierce, A. K., Livingston, W. C., Harvey, J. W., Schrage, D., Gillespie, B., Simmons, J., & Slaughter, C. 1976, *Appl. Opt.*, 15, 33
- Pontin, D. I., Hornig, G., & Priest, E. R. 2004, *Geophysical and Astrophysical Fluid Dynamics*, 98, 407
- Pontin, D. I., Galsgaard, K., Hornig, G., & Priest, E. R. 2005, *Physics of Plasmas*, 12, 052307
- Pontin, D. I., Hornig, G., & Priest, E. R. 2005, *Geophysical and Astrophysical Fluid Dynamics*, 99, 77
- Priest, E. R., & Démoulin, P. 1995, *J. Geophys. Res.*, 100, 23443
- Priest, E. R., & Forbes, T. G. 1990, *Sol. Phys.*, 126, 319
- Priest, E. R., Hornig, G., & Pontin, D. I. 2003, *Journal of Geophysical Research (Space Physics)*, 108, 1285
- Régnier, S., Parnell, C. E., & Haynes, A. L. 2008, *A&A*, 484, L47
- Riley, P., Linker, J. A., Mikić, Z., Lionello, R., Ledvina, S. A., & Luhmann, J. G. 2006, *ApJ*, 653, 1510
- Schatten, K. H., Wilcox, J. M., & Ness, N. F. 1969, *Sol. Phys.*, 6, 442
- Schrijver, C. J., & Harvey, K. L. 1994, *Sol. Phys.*, 150, 1
- Schrijver, C. J., & Title, A. M. 2001, *ApJ*, 551, 1099
- Schüssler, M., & Baumann, I. 2006, *A&A*, 459, 945
- Snodgrass, H. B. 1983, *ApJ*, 270, 288
- Titov, V. S., Galsgaard, K., & Neukirch, T. 2003, *ApJ*, 582, 1172
- Tokman, M., & Bellan, P. M. 2002, *ApJ*, 567, 1202
- Török, T., & Kliem, B. 2003, *A&A*, 406, 1043
- van Ballegooijen, A. A., & Martens, P. C. H. 1989, *ApJ*, 343, 971
- van Ballegooijen, A. A., Cartledge, N. P., & Priest, E. R. 1998, *ApJ*, 501, 866

- Wang, Y.-M., Nash, A. G., & Sheeley, N. R., Jr. 1989, *Science*, 245, 712
- Yashiro, S., Gopalswamy, N., Michalek, G., St. Cyr, O. C., Plunkett, S. P., Rich, N. B., & Howard, R. A. 2004, *Journal of Geophysical Research (Space Physics)*, 109, 7105
- Yeates, A. R., Mackay, D. H., & van Ballegooijen, A. A. 2007, *Sol. Phys.*, 245, 87
- Yeates, A. R., Mackay, D. H., & van Ballegooijen, A. A. 2008, *Sol. Phys.*, 247, 103
- Yeates, A. R., Nandy, D., & Mackay, D. H. 2008, *ApJ*, 673, 544
- Yeates, A. R., & Mackay, D. H. 2009, arXiv:0904.4419
- Zaitsev, V. V. & Stepanov, A. V. 2008, *Phys.-Usp.*, 51, 1123
- Zhang, J., Woch, J., Solanki, S. K., & von Steiger, R. 2002, EGS XXVII General Assembly, Nice, 21-26 April 2002, abstract #4034, 27, 4034
- Zhou, G., Wang, J. & Cao, Z. 2003, *A&A*, 397, 1057